Engineering the surface architecture of highly dilute alloys: an *ab initio* Monte-Carlo approach

Konstantinos G. Papanikolaou, Matthew T. Darby, and Michail Stamatakis*

[1] *Thomas Young Centre and Department of Chemical Engineering, University College London, Roberts Building, Torrington Place, London WC1E 7JE, UK*

Abstract

Highly dilute alloys of platinum group metals (PGMs) - (Pt, Rh, Ir, Pd, and Ni) with coinage metals (Cu, Au and Ag) serve as highly selective and coke-resistant catalysts in a number of applications. The catalytic behaviour of these materials is governed by the size and shape of the surface "ensembles" of PGM atoms. Therefore, establishing a means of control over the topological architecture of highly dilute alloy surfaces is crucial to optimising their catalytic performance. In the present work, we use on-lattice Monte Carlo (MC) simulations that are parameterised by density functional theory (DFT) derived energetics, in order to investigate the surface aggregation of PGM atoms under vacuum conditions and in the presence of CO. We study several highly dilute alloy surfaces at various PGM loadings, including Pd/Au(111), Pd/Ag(111), Pt/Cu(111), Rh/Cu(111), Ir/Ag(111) and Ni/Cu(111). Under vacuum conditions, we observe a thermodynamic preference for dispersion of PGM as single atoms in the surface of the coinage metal host, on all examined alloy surfaces except Ir/Ag(111), where Ir atom aggregation and island formation is preferred. By evaluating the alloy surface structure in the presence of CO, we determine that the size and shape of PGM ensembles can be manipulated by tuning the partial pressure of CO (P_{CO}) on the Pd/Au(111), Pd/Ag(111), Ir/Ag(111) and Ni/Cu(111) surfaces. In contrast, we determine that Pt/Cu(111) and Rh/Cu(111) highly dilute alloys are unresponsive to changes in P_{CO} with Rh and Pt dispersing as isolated single atoms within the host matrix, irrespective of gaseous composition. Our findings suggest that it may be possible to fine-tune the surface architecture of highly dilute binary alloys for optimised catalytic performance.

Keywords: Nanoalloy, Surface aggregation, Surface restructuring, Single atom alloys, Highly dilute alloys, *Ab initio* Monte Carlo simulation

Corresponding Author: m.stamatakis@ucl.ac.uk

1. Introduction

Bimetallic alloys, which are composed of two metals, often exhibit improved catalytic performance as compared to their monometallic counterparts.[1–3] For example, chemistries such as the selective dehydrogenation of ethanol to acetaldehyde and H_2 can be performed over Pt/Cu alloys at significantly higher rates than those acquired on pure Cu surfaces.[4] Ni/Au binary alloys are also known for their significantly higher stability compared to pure Ni catalysts during the steam reforming of methane.[5] Similarly, the addition of small amounts of Pd in Au nanoparticles (NPs) results in efficient catalysts for the oxidation of alcohols to aldehydes,[6] whilst preventing the formation of a catalytically inert Pd oxide phase that leads to the deactivation of pure Pd catalysts.[7]

Remarkably, bimetallic alloys that are composed of an inert host metal (i.e. Cu, Au and Ag) and very small amounts of a catalytically active platinum group metal (PGM) can exhibit high selectivity, activity and stability towards deactivation.[1,8–10] In this class of bimetallic alloys, the PGM dopant atoms are embedded in the surface layer of the host metal. With a loading that is sufficiently low, the dopant will disperse in the form of isolated atoms (i.e. monomers) in the surface layer of the host metal, thereby forming a single atom alloy (SAA). The activation of substrates by the catalytic surface of a SAA occurs on the dopant metal atoms prior to spillover onto the inert host metal where highly selective catalysis may occur.[11] Interestingly, the binding of adsorbates on SAA isolated dopant atoms is often weaker as compared to a pure dopant catalyst, which allows for the facile desorption of products and tolerance to common poisons.[12–17]

Though their application has been met with resounding success in the catalysis of a number of chemical processes, the use of SAAs is not ubiquitous. In some instances, dispersed dopant atoms are not capable of activating chemical bonds, with this task requiring contiguous active dopant metal sites.[18] For example, Goodman and co-workers[19] studied the dehydrogenation of ethylene (C_2H_4) over a Pd/Au alloy supported on SiO_2, indicating that there exists a linear increase in the reaction rate with respect to the density of Pd dimer and trimer species on the catalyst surface. Interestingly, in the absence of these Pd clusters the reaction rate was poor, whereas at high densities of contiguous sites the activity was excellent. Similarly Gao et al.[7] focused on the catalytic oxidation of CO over a Pd/Au(100) surface and determined that isolated Pd atoms are not capable of dissociating O_2, which is an essential elementary reaction in a number of oxidative chemical systems. The inability of isolated Pd atom monomers to dissociate O_2 has since been rationalised by DFT calculations by Ham et al.[20]; these calculations have demonstrated that the activation barrier of the O_2 scission reaction is significantly lower on Pd dimers and Pd trimers as compared to single Pd atoms. The lower activation barrier of the reaction in the former configurations, is ascribed to the fact that these Pd aggregates are only partially covered by CO (e.g. a Pd dimer with only one CO adsorbed thereon), thereby enabling O_2 to interact with the free Pd atoms of the small clusters for a sufficient amount of time and therefore dissociate.[20] Along the same lines, the SAA phase exhibits relatively low activity during the hydrogenation of diphenylacetylene over Pd/Ag alloys,[21] whilst Vignola et al.[22] argued that the oligomerisation of acetylene (C_2H_2), which takes place as a side-reaction during its hydrogenation, can be prevented by ensembles of two

or three Pd atoms. Oligomerisation gives rise to detrimental coupled species that poison the active sites of the process catalyst, and therefore, using ensembles that prevent this would be essential in catalytic process development.

Thus, it is evident that certain chemistries can be catalysed by materials with dopant atoms at high dispersion, whereas other chemistries require the presence of contiguous sites as found in dopant atom dimers, trimers and islands. Indeed, it is well-known that the alloy structure and composition strongly affect the adsorption energy of surface intermediates[23–26] and the catalytic performance during a chemical process.[27] Accordingly, a number of experimental and theoretical studies investigating the structure of alloy systems under vacuum[28–32] versus reactive conditions[13,14,20,22,33–41] (i.e. in the presence of adsorbates) have appeared in the literature. For example, Han et al.[42] adopted an *ab initio* Monte Carlo (MC) approach in order to investigate the effect of oxygen chemical potential on the structure and composition of Ru/Pt alloys. An extensive formation of Ru islands was observed at high oxygen chemical potentials because of stronger Ru-O interactions compared to Pt-O. Conversely, at low oxygen chemical potentials, a phase of isolated Ru atoms was thermodynamically favoured.[42] McCue and Anderson studied the CO-induced surface segregation on Pd/Cu alloys supported on Al_2O_3 by means of Fourier-transform infrared (FTIR) spectroscopy.[34] Based on their findings, the authors concluded that the pre-treatment of a 1:10 Pd/Cu alloy with CO can bring about the segregation of Pd atoms from the bulk to the surface, thereby giving rise to a significant fraction of Pd-Pd dimer species.[34] In turn, CO pre-treated Pd/Cu catalysts were found to be considerably more active for the hydrogenation of acetylene (C_2H_2) than those that were not pre-treated, in which Pd was dispersed as isolated single atoms.[34] Similarly, the activity of Pd/Ag alloys toward the hydrogenation of diphenylacetylene was enhanced after catalytic pre-treatment with O_2 or CO, with the improvement in catalytic activity being ascribed to the formation of contiguous Pd sites.[21]

The aforementioned studies highlight the importance of defining ways in order to control the topological architecture of bimetallic alloys. Once such control is achieved, an alloy catalyst may be manipulated to yield fine-tuned compositions and "ensembles" of metallic sites exhibiting tailored catalytic behaviour.[20,34] With this in mind, we investigate the surface aggregation of dopant atoms on numerous (111) highly dilute alloy surfaces in the presence versus absence of CO, which is a molecule commonly found as a substrate or impurity in many industrial processes. We study the effects of the dopant loading and the partial pressure of CO (P_{CO}) on the surface structure of these alloys. Based on density functional theory (DFT) calculations, we parametrise MC simulations and investigate the thermodynamically favourable dopant configurations on several alloy surfaces of practical interest including Pd/Au(111), Pd/Ag(111), Pt/Cu(111), Rh/Cu(111), Ir/Ag(111) and Ni/Cu(111).[8,17,19,35,43–45] Our results suggest that there are three main patterns of behaviour: (1) alloys in which dopant atoms tend to form clusters even under vacuum and irrespective of the dopant loading; (2) alloys whereby the SAA phase is preferred throughout the entire range of P_{CO}; (3) alloys in which the SAA phase is dominant under vacuum, but considerable aggregation is induced by CO at intermediate P_{CO}. This work aims

at providing a "compass" that will enable experimentalists to navigate the large design space of highly dilute alloys with optimal performance for a particular application.

The rest of the paper is organised as follows: in section 2**,** we provide details on the DFT and MC setups used for our calculations. In section 3, we present our results on the surface aggregation of each highly dilute alloy in our study, both under vacuum conditions and in the presence of CO. Finally, we summarise the main findings of this work in section 4.

2. Computational Details

Density functional theory calculations. For consistency we use the computational setup for DFT calculations as described in our previous work.[13] We have performed periodic DFT calculations as implemented in the Vienna *ab initio* Simulation Package (VASP) version 5.4.1,[46,47] under the generalized gradient approximation, making use of the revised Perdew–Burke–Ernzerhof (RPBE) exchange–correlation energy functional.[48] We do not impose van der Waals corrections, since the RPBE functional has been shown to predict CO binding energies that reproduce remarkably well temperature programmed desorption (TPD) spectra.[13] Spin polarized calculations were performed only for the Ni/Cu surfaces. The core ionic electrons were treated using projector augmented wave (PAW) potentials and the valence electronic wave functions were expanded using plane waves with an energy cutoff of 400 eV. We modelled the FCC (111) slab using a five–layer p(3 × 3) unit cell (see section IX in the supporting information). We expect that the presence of a small number of dopant atoms on the surface layer of the alloy surface is unlikely to bring about a change to the lattice constant of the host metal. Therefore, the two bottom-most layers were kept fixed at the corresponding RPBE lattice constant of the host metal (3.64, 4.23, and 4.22 Å for Cu, Ag, and Au, respectively) and the three top-most layers were allowed to relax during ionic optimization. The Brillouin zone was sampled with a 13 × 13 × 1 Monkhorst–Pack k-point mesh and the Hellmann–Feynman forces on all atoms that are free to move were relaxed to less than 10^{-2} eV/Å. To aid with convergence, we employed the smearing scheme of Methfessel and Paxton with a width of 0.1 eV. The adsorption energy of *m* CO molecules ($E_{ads}(m{\cdot}CO)$) was computed according to eq. (1):

$$E_{ads}\left(m\cdot\mathrm{CO}\right)=E_{tot}^{mCO+slab}-E_{tot}^{slab}-m\cdot E_{tot}^{CO_{(g)}}, \quad (1)$$

where $E_{tot}^{mCO+slab}$ is the DFT total energy of *m* CO molecules co-adsorbed on a slab, E_{tot}^{slab} is the DFT total energy of the clean slab and $E_{tot}^{CO_{(g)}}$ is the DFT total energy of a CO molecule in the gas phase. More negative values of E_{ads}(CO) indicate stronger CO binding on the surface. The DFT-computed formation energies, which are used for the fitting of the cluster expansions (CEs) (see next subsections), are defined with respect to the DFT total energy of CO gas and the corresponding SAA catalyst, as follows:

$$E_f=E_{tot}\left(n+m\cdot CO\right)+\left(n-1\right)\cdot E_{tot}\left(host\right)-n\cdot E_{tot}\left(SAA\right)-m\cdot E_{tot}^{CO_{(g)}}, \quad (2)$$

where $E_{tot}(n{+}m{\cdot}CO)$, $E_{tot}(host)$, $E_{tot}(SAA)$ and $E_{tot}^{CO_{(g)}}$ are the DFT total energies of an alloy surface with a cluster of *n* dopant atoms and *m* CO adspecies, the pure host material and a single dopant atom in the surface layer of the host material, respectively. According to eq. (2), the formation energy of an adsorbate-free SAA

surface is zero. Along these lines, the SAA configuration and CO in the gas phase are used as a reference and therefore the formation energy of any other configuration is relative to their energies (for a schematic explanation of eq. (2) see section XI in the supporting information). Negative and positive values of E_f indicate, respectively, geometries with higher and lower stability than the SAA geometry with gas CO.

Finally, vibrational frequencies were computed within the harmonic approximation using a finite difference displacement of 0.02 Å (see section VII in the supporting information). Based on the attained vibrational frequencies of CO in the chemisorbed state, we computed zero-point energy corrected pre-exponential factors for the desorption of CO (see next subsection).

Monte Carlo simulations. On-lattice MC simulations were performed within the graph-theoretical (GT) framework of Stamatakis and coworkers,[49,50] as implemented in *Zacros* (version 2.0).[51] The MC calculations were performed within the grand canonical ensemble with a fixed CO chemical potential (calculated from P_{CO}) and a constant number of dopant/host atoms in each simulation. We performed MC simulations with various dopant loadings (1, 2, 3 and 4%) under vacuum conditions, as well as at various P_{CO} for dopant loadings of 4 %. In the latter calculations, we investigate partial pressures of CO that result in CO dopant fractional coverages (Ω_{CO}) in the range of $0.0 \leq \Omega_{CO} \leq 1.0$, and we define this quantity as

$$\Omega_{CO} = \frac{N_{CO*}}{N_{Dopant}}, \qquad (3)$$

where N_{CO*} is the number of adsorbed CO molecules on the dopant metal atoms and N_{Dopant} is the total number of dopant atoms. We note that due to the weak interactions between CO and the Au(111), Cu(111) and Ag(111) surfaces and the low P_{CO} employed in all simulations, the CO coverage on the host metal atoms is negligible; however, we note that CO adsorption and diffusion on host metal sites are explicitly taken into account in our MC model (see the following paragraphs).

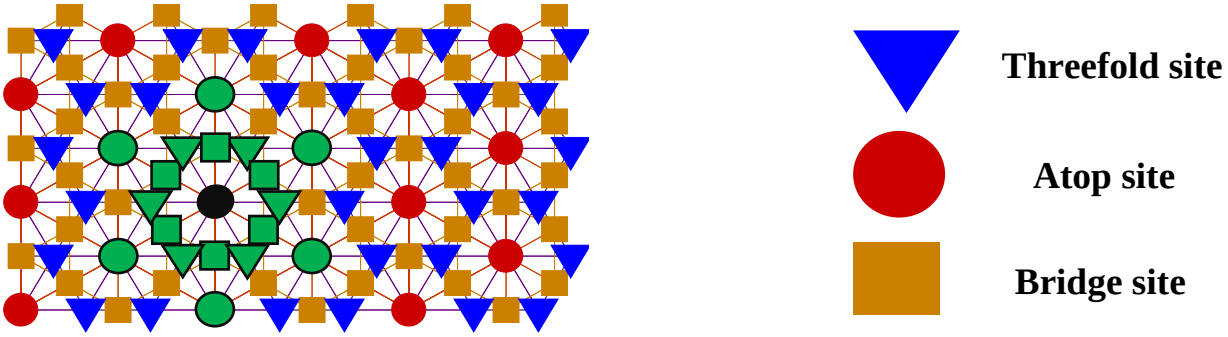

Figure 1. Lattice employed in MC simulations. Three site types are considered: atop (shown as red circles), threefold (shown as blue triangles) and bridge (shown as orange squares). The sites that are connected with the atop site shown as black circle are shown in green.

The simulation lattice contains three different site types, atop, threefold and bridge. The binding strength of CO on fcc and hcp threefold sites surrounded by dopant atoms is very similar.[13] Therefore, we simplify the MC lattice by using only the fcc threefold site energies to treat both sites, referring to these throughout the text as “threefold”. To minimise any finite lattice size effects,[52] we performed preliminary lattice size testing (see section I in the supporting information). On the basis of our tests, we employed lattices with a total number of sites of 19,200 (3,200 atop sites) and 7,500 (1,250 atop sites) for the simulations under

vacuum conditions and in the presence of CO, respectively, as there were no notable lattice size effects in either case (see section I of the supporting information). A representative lattice structure used in our simulations is shown in Figure 1. Each top site is connected with 18 sites, including the closest 6 atop sites, 6 bridge sites and 6 threefold sites (Figure 1). For example, the atop site shown in black in Figure 1 is connected with all the surrounded sites shown in green. Moreover, each bridge site is connected with 8 neighbouring sites: the closest 2 threefold sites, 4 bridge sites and 2 atop sites. Finally, each threefold site is connected with the closest 3 atop sites and 3 bridge sites (Figure 1).

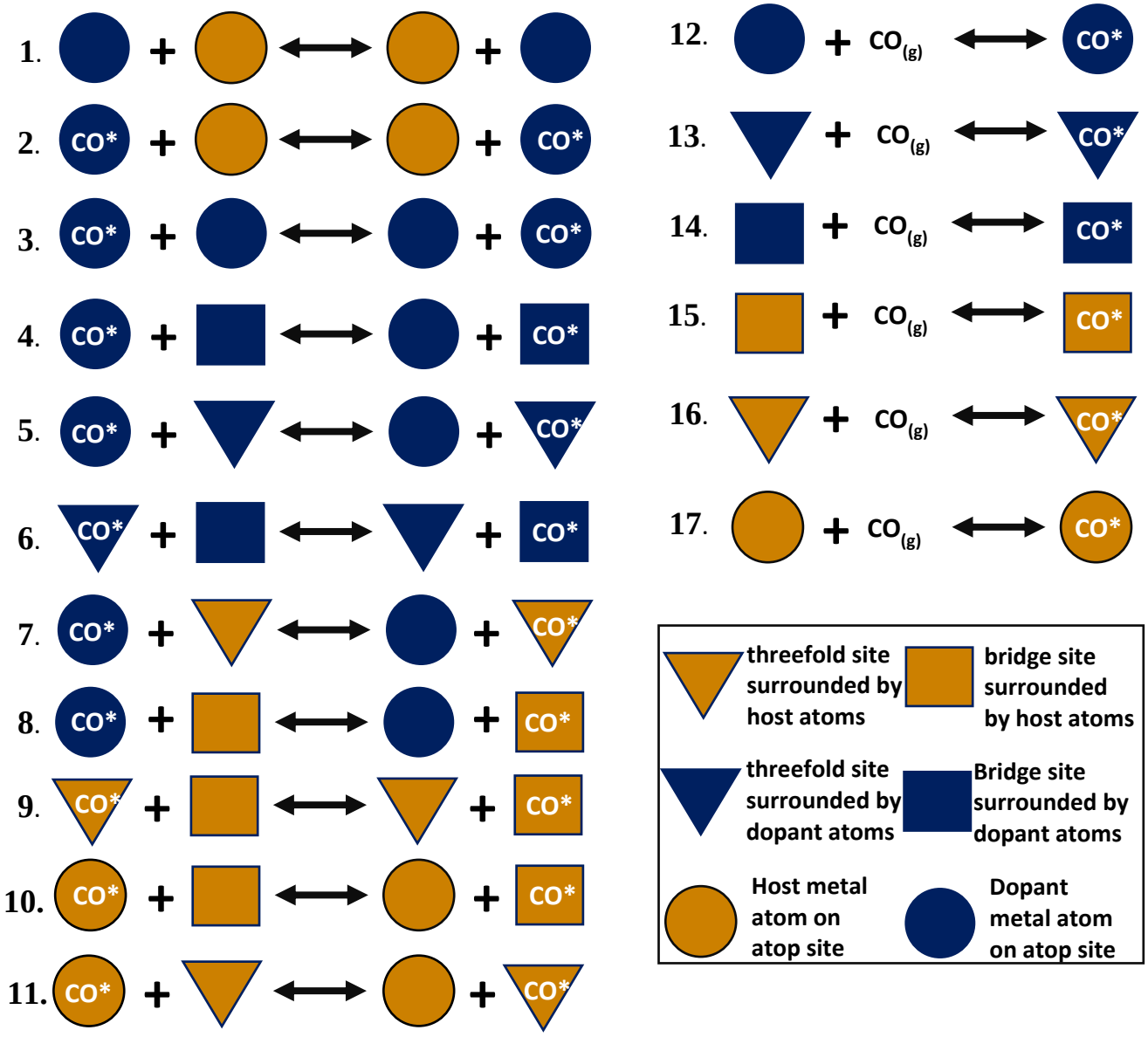

Figure 2. Schematics of the microscopic processes included in the reaction mechanism of the MC simulations. Processes 1-3 correspond to swaps of surface species; processes 4-11 are diffusions of CO and processes 12-17 are CO adsorptions on the different site types. Dopant and host metal atoms are shown as blue and orange circles, respectively. Bridge sites surrounded by dopant and host metal atoms are shown as blue and orange squares, respectively; similarly for threefold sites but with triangle symbols. Adsorbed CO is denoted as CO*. We note that all the microscopic processes are included in the reaction mechanism of Au- and Ag-based alloys. For Cu-based alloys the adsorption of CO on Cu atop sites is omitted and therefore processes 10, 11 and 17 are not included in the reaction mechanism.

In order to capture both the state of CO adlayer and that of the alloy surface with our model, we adopt the following conventions: atop sites are always covered by one of the following four species: a bare dopant atom (i.e. not covered by CO), a bare host atom (i.e. not covered by CO), a CO-covered dopant atom or a CO-

covered host atom. Importantly, the last species appears only on Au- and Ag-based alloys, where CO can adsorb in all the host metal site types; these are atop, bridge and threefold. By contrast, the adsorption of CO on Cu atop site on the Cu(111) surface is significantly less stable than on Cu-Cu bridge and threefold fcc site ($E_{ads}(CO)$ of -0.51 eV, -0.48 eV and -0.36 eV for threefold, bridge and atop sites, respectively) and therefore we exclude CO adsorption and diffusion on Cu atop sites from our MC model. In addition, bridge or threefold sites can be either vacant or occupied by CO. This gives rise to 5 species that are considered for the Cu-based alloys in our MC simulations: dopant atom, host atom, CO*-threefold, CO*-bridge, CO*-top dopant. Along the same lines there are 6 species considered for Au- and Ag-based: dopant atom, host atom, CO*-threefold, CO*-bridge, CO*-top dopant and CO*-top host.

We allowed for several state-to-state events to occur on the lattice during the MC simulation including: i) swaps of atop surface species (e.g. dopant metal atoms, host metal atoms and dopant atoms with a CO molecule attached); ii) CO diffusions from one site to another; and iii) CO adsorption on different site types (Figure 2). We consider 17 state-to-state events in total (Figure 2), from which only the adsorptions/desorptions of CO are actual elementary events. In contrast, the rates of CO diffusion events and species swaps are set to be much faster than CO adsorption/desorption so that stationary conditions are reached efficiently in the simulation. In any case, given enough simulation time, the system would sample the most thermodynamically favourable surface configurations, in line with the objective of our study, which did not aim at resolving the kinetics of the host-dopant atom swaps.

CO adsorption events are treated as non-activated, and we compute the kinetic constant of CO adsorption (or equivalently the pre-exponential factor) using the 2D gas model:[53]

$$k_{ads} = \frac{P_{\mathrm{CO}} \cdot A_{st}}{\sqrt{2 \cdot \pi \cdot m_{\mathrm{CO}} \cdot k_B \cdot T}}, \tag{4}$$

where m_{CO} is the mass of a CO molecule, k_B is the Boltzmann constant, T is the temperature and A_{st} is the effective area of the adsorption site. The latter quantity is approximated by the van der Waals radius of the metal atom whereon the CO chemisorption takes place. In turn, the rate constant for the desorption of CO is calculated using the Eyring equation as derived from harmonic transition state theory:

$$k_{des} = \frac{Q_{vib,\mathrm{CO}_{(g)}} \cdot Q_{transl,\mathrm{CO}_{(g)}} \cdot Q_{rot,\mathrm{CO}_{(g)}}}{Q_{vib,\mathrm{CO}^*}} \cdot \frac{k_B \cdot T}{h} \cdot \exp\left(\frac{\Delta E_{ads}}{k_B \cdot T}\right), \tag{5}$$

where $Q_{vib,\mathrm{CO}(g)}$, $Q_{transl,\mathrm{CO}(g)}$ and $Q_{rot,\mathrm{CO}(g)}$ are the vibrational, translational and rotational partition functions of a CO molecule in the gas phase, h is the Planck's constant, ΔE_{ads} is the adsorption energy and Q_{vib,CO^*} is the vibrational partition function for a CO molecule, which is chemisorbed on the alloy surface.

We highlight that the actual values of k_{ads} and k_{des} are not important, as we are not interested in the kinetics; yet, their ratio has to be correctly calculated, because it is directly related to the chemical potential of gas CO. Thus, based on the equations above and those presented in section VIII of the supporting information, we find the ratio of the forward over the reverse pre-exponentials for all the CO adsorption events (reactions 12-17 in Figure 2). The use of these pre-exponential ratios in our calculations ensures their thermodynamic consistency.

Along the same lines, the thermodynamically consistent pre-exponential ratios of CO diffusion events (reactions 4-11 In Figure 2) are calculated on the basis of a thermodynamic cycle (see section VI of the supporting information), which includes CO adsorption to one site type, then diffusion of CO from this site type to another site type and finally desorption of CO from the latter site.

In all simulations the MC lattice is initialised without any CO species adsorbed on the surface. Each atop site is occupied by either a dopant or a host atom and the dopant loading remains constant at all times. We consider several surface aggregates, referred to as surface species from here on, including isolated dopant atoms (i.e. monomers), contiguous dopant dimers and trimers, but also island species that contain more than 3 dopant atoms. The system is allowed to reach stationary conditions, detected by having a constant average number of surface species and Ω_{CO} over a time-window (see section V in the supporting information). Under these circumstances, the lattice state is frequently sampled (see sections I and V of the supporting information) and the average fractional coverage of a particular surface dopant atom species *k* (single atoms, dimers, trimers, …), $\overline{Y_k}$, is computed using eq. (6):

$$\overline{Y_k} = \frac{1}{N_{MC,conf}} \sum_{i=1}^{N_{MC,conf}} Y_{k,i} = \frac{1}{N_{MC,conf}} \sum_{i=1}^{N_{MC,conf}} \left(\frac{N_{k,i}}{N_{tot,i}} \right), \qquad k \in \{Monomers, Dimers, Trimers, ...\} \tag{6}$$

where $Y_{k,i}$ is the fraction of dopant species *k* in snapshot *i*, $N_{MC,conf}$ is the number of lattice snapshots taken under stationary conditions, $N_{k,i}$ is the number of dopant species *k* in snapshot *i* and $N_{tot,i}$ is the total number of species detected in snapshot *i*. It follows that the number of dopant atoms (N_D), which is constant in each simulation, is linked to the fractions of the dopant species as shown in eq. (7):

$$N_D = N_{tot} \cdot \sum_{m=1}^{D\max} Y_m \cdot m \,, \tag{7}$$

where N_{tot} is the total number of species in a particular snapshot, Y_m is the fraction of species with *m* dopant atoms and D_{max} is the number of dopant atoms contained in the largest species existing on the alloy surface. To simplify the analysis, we will lump together any species larger than trimers into a class of species referred to as *islands*.

Cluster expansion Hamiltonians. We have performed an approximate total of 240 DFT calculations with various dopant and CO arrangements on the alloy surfaces in this study (see section III of the supporting information). Using this DFT dataset, we have fitted a CE for each alloy system,[54] enabling the fast computation of the energy of arbitrarily complex configurations formed on the MC lattice during simulation. The CE method was recently implemented in the GT framework by Nielsen et al.[50] and within this formalism, the energy, $H(\sigma)$, of a configuration σ is expanded in "clusters" or "figures". These clusters represent single- to multi-body terms with a certain energy contribution to the total energy of a lattice configuration, $H(\sigma)$, which is given by:

$$H(\sigma) = \sum_{k=1}^{N_c} \frac{\mathrm{ECI_k}}{\mathrm{GM_k}} \mathrm{NOC_k} \,, \tag{8}$$

where N_c is the number of clusters included in the energetics model, ECI_k is the so-called energy effective cluster interaction of pattern k (i.e. the contribution of that arrangement of adsorbates to the total energy), NOC_k is the number of times a cluster k is detected on a lattice configuration σ, and GM_k is a graph-multiplicity factor included to prevent over-counting since some patterns are detected more than once because of their symmetry.[50]

We note that an exact CE can in principle be built by incorporating a very large number of clusters in the energetics model. Yet, the calculation of the ECI parameters for such a large number of incorporated clusters would require an impractically large number of DFT calculations. In addition, it is known that the inclusion of an excessive number of terms in the CE gives rise to overfitting issues.[53,55] A common practice in order to overcome these challenges is to truncate the CE, by choosing an appropriate small set of energetic clusters, based on which one can accurately compute the energy of any on-lattice adsorbate configuration. After fitting the truncated CE, its performance is assessed by statistical measures such as the leave-one-out cross-validation (LOO-*CV*) score,[55–57] which indicates the predictive capacity of the CE. The lower the *CV* score the higher the probability that the energy of new configurations (not included when fitting) will be predicted accurately. The *CV* score is found as follows: after leaving a configuration out from the DFT dataset, we compute the ECI parameters by fitting a system of eq. (8) to the DFT-computed formation energies of the remaining configurations therein; subsequently, the formation energy of the omitted configuration is calculated based on the retrieved ECIs and compared to the DFT formation energy. This procedure is repeated for each configuration included in the DFT dataset and the *CV* score is then calculated as:

$$CV^2 = \frac{1}{N_{conf}} \sum_{i=1}^{N_{conf}} \left[E_{CE}\left(\sigma_i\right) - E_{DFT}\left(\sigma_i\right) \right]^2 , \qquad (9)$$

where N_{conf} is the number of configurations in the DFT dataset, and $E_{CE}(\sigma_i)$ and $E_{DFT}(\sigma_i)$ are the CE-predicted and DFT-computed formation energies of configuration *i* (see eq. (8)).

In our CEs, we consider explicitly the spatial arrangement of dopant and host atoms in the lattice top sites, as well as CO as an adsorbate (surface species). This adsorbate can be bound to dopant top sites, bridge sites formed by two neighbouring dopant atoms (dimer), threefold sites surrounded by a dopant triangle (trimer) and to the most stable adsorption sites on the host (111) surfaces. The latter sites correspond to bridge and threefold sites on Cu(111) surfaces and atop, bridge and threefold sites on Au(111) and Ag(111) surfaces.[13] Our DFT calculations show that the adsorption of CO on mixed sites (i.e. bridge sites between a dopant atom and a host metal atom or threefold sites between 2 dopant atoms and 1 host) is not stable. This is in agreement with earlier DFT-based studies[20] and high-resolution electron energy-loss spectroscopy (HREELS) works, which for example reveal that CO adsorption can be stable on mixed Ni-Cu bridge sites only at high CO coverages and temperatures lower than 130 K.[58] Accordingly, we ensure that CO adsorption is not stable on mixed sites by assigning a high ECI value to clusters formed by CO and a mixture of dopant and host metal atoms (see section II in the supporting information). This value is 10.0 eV, which is appropriate for the temperature range of our studies, since it is much larger than $k_B \cdot T$ at all temperatures considered.

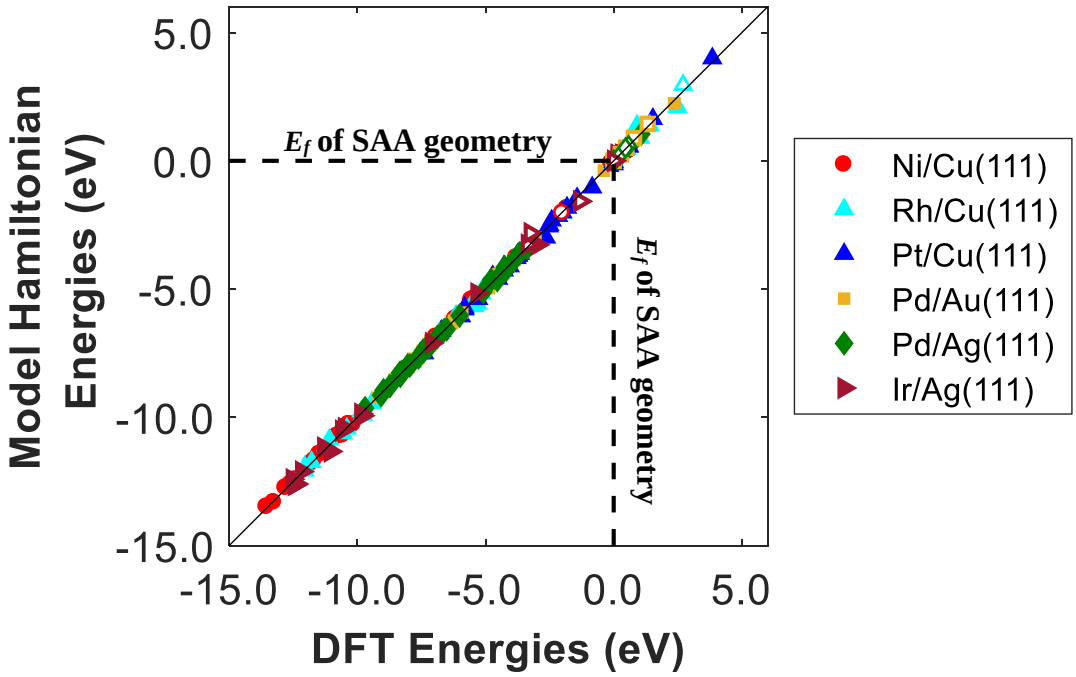

Figure 3. Parity between the DFT-computed and the CE-predicted formation energies of the geometries included in the DFT datasets of all investigated alloys. Open symbols represent the formation energy of clean geometries (i.e. geometries without CO adsorbed)**.** Positive energy values correspond to geometries of lower stability than the SAA geometry. The dashed lines indicate the formation energy of the SAA geometry, which is used as a reference.

In our CEs , we consider terms with a different number of dopant atoms in various geometries (see section III the supporting information). Furthermore, we include several two-body CO-CO interaction terms in the energetics (CO adspecies are adsorbed on different site types) with up to 2nd nearest neighbour (2NN) interaction range (see section II in the supporting information). Figure 3 shows the parity between the DFT-computed formation energies of the geometries in our DFT datasets sets and the CE-predicted formation energies. We note that the relative stability of trimer and dimer structures compared to the SAA structure, for all the alloys under investigation herein, was extensively discussed by Stamatakis and co-workers in previous studies.[13,14] These works explored both vacuum and reactive conditions (i.e. in the presence of CO). Moreover, Table 1 shows the number of figures included in the CE of each alloy, the number of DFT geometries used to fit each CE, the root-mean square (RMS) errors between the DFT-computed and CE-predicted formation energies, as well as the calculated *CV* scores. We briefly note that the *CV* score and the RMS errors are normalised with respect to the number of top sites (Table 1).

Table 1. Tabulation of the details of the CEs for each investigated surface in the present work.

Surface	Figures included in the CE	Number of DFT Geometries	Root-mean square between DFT and CE (meV/site)	*CV* score (meV/site)
Ni/Cu(111)	19	42	10.0	2.7
Rh/Cu(111)	20	36	24.0	8.0
Pd/Ag(111)	20	42	9.0	3.0
Pd/Au(111)	20	46	10.0	3.2
Pt/Cu(111)	19	35	17.0	6.5
Ir/Ag(111)	19	41	31.0	9.7

3. Results and Discussion

We investigate the surface aggregation of dopant atoms over a number of (111) highly dilute alloy surfaces. In general, the low-index (111) facet exhibits high thermodynamic stability,[59] being extensively exposed in NPs of FCC metals.[60] We perform simulations under vacuum conditions (P_{CO} = 0), as well as in the presence of gas CO at different concentrations (i.e. various P_{CO}). In the latter case, the chemical potential of CO is such that the CO dopant fractional coverage, Ω_{CO}, is within the range of 0.0 – 1.0 (see eq. (3)), whilst the host metal remains almost free of chemisorbed CO during simulation.

3.1. Surface aggregation of dopant atoms under vacuum conditions

We first use our MC model to investigate the effect of the dopant loading on surface aggregation under vacuum conditions. We study (111) surfaces of various dopant loadings within the range of 1 - 4 % at 350 K. Dopant loadings within this range are typically found in SAA catalysts employed in experimental studies.[8,17,61] SAA catalysts are prepared by methods whereby the dopant atoms are deposited on the surface of the host metal (galvanic replacement for NP synthesis[1] and vapour deposition in surface science).[61]

We assume that the barrier for diffusion of dopant atoms from the surface layer to the bulk is sufficiently large so that dopant atoms will be kinetically trapped on the surface of the catalyst under vacuum conditions and not segregate into the bulk of the alloy.[13,14] Indeed, we note that a number of SAAs are kinetically stable as extended surfaces and NPs, despite having a thermodynamic preference for dopant atom segregation into the bulk.[13,14,17,62] In particular, Sykes and co-workers have highlighted the importance of the temperature under which the dopant deposition happens;[63] they studied the Pd/Cu(111) structure showing that only when Pd deposition occurs at high temperatures (e.g. 500 K), there is a significant fraction of Pd atoms segregating into the subsurface layer of the alloy.[63] Conversely, when Pd deposition took place at 350 K the vast majority of Pd atoms remained on the surface layer. Along the same lines, HREELS studies have shown that on Ni/Cu(111) surfaces, segregation of Ni atoms into the bulk takes place only when Ni deposition occurs at temperatures higher than 475 K.[64] Moreover, we note that under reactive conditions, and particularly in the presence of CO, dopant atoms are generally very stable on the surface layer of highly dilute alloys as a result of the strong CO-dopant interactions.[13,14,34,42]

In addition, we assume that the deposition of the dopant onto the host metal surface occurs at high enough temperatures so that dopant atoms are mixed in the matrix of the host metal, thereby forming a surface alloy. According to the pioneering work of Garfunkel and co-workers,[64] deposition of Ni on Cu(111) surfaces within the temperature range of 375 - 475 K inhibits the formation of Ni 2D and 3D islands on (top of) the host surface, and also prevents the segregation of Ni into the bulk of the alloy.

Figure 4 shows the results of our MC simulations under vacuum conditions for all the alloys under investigation. A general observation is that within the examined range of 1 - 4 %, there is a small effect of the dopant loading on the surface aggregation. In particular, we simulate a clear thermodynamic preference toward the SAA phase for Pd/Au(111), Pt/Cu(111), and Rh/Cu(111) surfaces for all the considered dopant loadings (Figure 4 (c), (e) and (f), respectively). For all these cases $\overline{Y_{Monomers}} > 0.99$. Our calculations are in good

agreement with combined surface science and theoretical studies on the Pt/Cu(111) system,[43] where the SAA phase was found to prevail at Pt coverages lower than 6 % of the monolayer. Along the same lines, our simulations are corroborated further by H_2 activation studies on Pd/Au(111) alloys, which have revealed a tendency of Pd atoms to be dispersed at Pd coverages less than 0.05 ML,[17] as well as by recent theoretical works.[40,65] We also note that the strong preference for the dispersion of the dopant atoms in Pd/Au(111), Pt/Cu(111) and Rh/Cu(111) alloys has been suggested by recent DFT studies, in which the aggregation energies (ΔE_{agg}) for the formation of dimer and trimer species for all the aforementioned alloys were found to favour the SAA phase under vacuum.[13]

Conversely, we observe that the effect of dopant loading on the surface aggregation is, to some extent, important on the Pd/Ag(111) and more so on the Ni/Cu(111) surface (Figure 4 (a)). More specifically, for Pd/Ag(111) and Ni/Cu(111) surfaces and at 1% PGM loading, we compute a small fraction of dimers of 0.02 and 0.03, respectively (Figure 4 (a) and (b)). However, these dimer fractions are considerably larger at 4 % dopant loading, where $\overline{Y_{Dimers}}$ = 0.06 and 0.10 for Pd/Ag(111) and Ni/Cu(111), respectively (Figure 4 (a) and (b)). Both cases are quite interesting, as they exhibit a behaviour that could not have been predicted by DFT calculations alone. For instance, under vacuum conditions, the DFT-computed ΔE_{agg} for dimer clusters on the Ni/Cu(111) surface is -0.01 eV.[13] This value is almost zero suggesting that, enthalpically, the SAA phase and the formation of Ni dimers will be almost equally favoured. Yet, our MC simulations suggest that Ni atoms tend to be dispersed (i.e. $\overline{Y_{Monomers}}$ > 0.85) and that there is only a small fraction of dimers, which becomes larger at increasing Ni coverage. This is attributed to configurational entropy contributions to the free energy of the system, which become increasingly more important at higher temperatures, as those reached under experimental conditions. Similar conclusions hold for the case of Pd/Ag. We point out that these effects of coverage, temperature, and entropy are explicitly considered in our MC simulations, but are not accounted for in DFT calculations, thereby highlighting the value of MC approaches in elucidating the behaviour of such alloys.

Finally, we find that the enthalpic preference for the formation of Ir aggregates on the Ir/Ag(111) surface is sufficiently high, such that there are no isolated Ir atoms thereon. Our previous DFT studies have highlighted the high thermodynamic stability of dopant aggregates (e.g. for Ir triangular trimers ΔE_{agg} = -0.90 eV).[13] Yet, the present MC approach enables us to upscale these previous investigations, thereby showing that Ir aggregates with more than three Ir atoms dominate over the Ir/Ag(111) surface (Figure 4 (d)).

3.2.Surface aggregation of dopant atoms in the presence of CO

Previous studies in relation to the adsorption of CO on various (111),[13] (100)[14] and (211)[14] highly dilute alloy surfaces have shown that CO chemisorption is, in general, more stable on hollow sites of dopant aggregates (i.e. dimers and trimers) than on their atop sites. Yet, Ir alloys do not exhibit this behaviour; in these alloys, CO adsorption is very stable on the atop sites of Ir trimers and Ir-Ir species.[13,14] A CO molecule adsorbed on the hollow site of a dopant cluster can bring about the trapping of the dopant atoms in

neighbouring positions, thereby providing an enthalpic driving force for surface aggregation. In contrast, at high CO dopant coverage, lateral interactions between CO adspecies will inhibit aggregation.

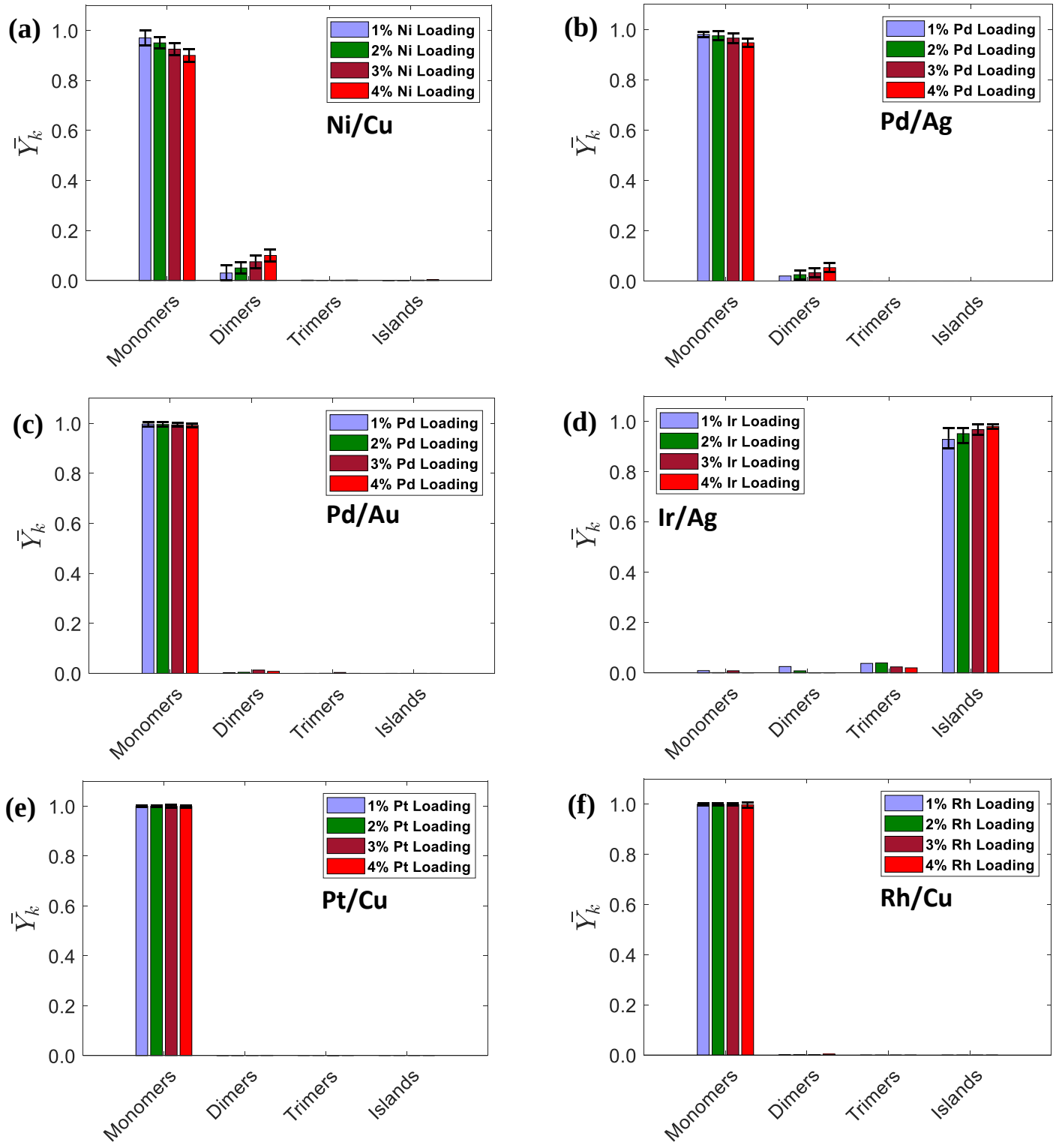

Figure 4. Fractions of surface species $\bar{Y}_k$ at 350 K under vacuum conditions and at different dopant loadings for (a) Ni/Cu(111) (b) Pd/Ag(111) (c) Pd/Au(111) (d) Ir/Ag(111) (e) Pt/Cu(111) and (f) Rh/Cu(111). The error bars are ± one standard deviation.

The ability of CO to induce or inhibit surface aggregation in bimetallic alloys has been highlighted by molecular dynamics and DFT studies,[13,14,20,66] whilst electronic factors of the surface aggregation of Pd atoms on Pd/Cu(111) surfaces were discussed in an excellent DFT study by Kasai and co-workers.[67] With this in

mind, we proceed by exploring the effect of CO coverage, Ω_{CO}, on the surface aggregation of dopant atoms on each of the (111) highly dilute alloy surfaces in this study. P_{CO} is varied such that Ω_{CO} takes values in the range of 0.0 – 1.0, and such that the host metal atoms remain almost CO-free. The dopant loading is kept fixed at 4 % in all the simulations presented in this section. We report Ω_{CO} and $\overline{Y_k}$ at different values of a normalised pressure, P_N (Figure 5 (a)-(f)), which we defined as:

$$P_N = \frac{P_{CO}}{P_{CO,max}}, \tag{10}$$

where P_{CO} is the applied partial pressure of CO and $P_{CO,max}$ is the partial pressure of CO for which the Ω_{CO} assumes a value close to unity (see section VII of the supporting information). Therefore, $P_N = 1.0$ corresponds to dopant atoms approximately fully covered by CO (i.e. one CO adspecies per dopant atom) and P_N values close to zero correspond to CO-free dopant atoms (i.e. vacuum conditions).

We note that for almost all the alloys there is a general thermodynamic preference toward the SAA phase at low P_N (i.e. low Ω_{CO}) - (Figure 5 (a), (b), (c), (e) and (f)). An exception to this is Ir/Ag(111), where we observe that for $\Omega_{CO} < 0.28$, Ir atoms aggregate to form islands (Figure 5 (d)). Moreover, the SAA phase is also favoured on all the alloy surfaces at P_N values close to unity (Figure 5 (a)-(f)), corresponding to almost one CO adspecies per dopant atom ($\Omega_{CO} \rightarrow 1$). Under these circumstances, repulsive CO-CO lateral interactions tend to break dopant clusters apart by overcoming any attractive dopant-dopant interactions, thereby promoting the formation of the SAA phase.

On the other hand, we realise that surface aggregation is induced at intermediate CO dopant fractional coverages on Ni/Cu(111), Pd/Ag(111) and Pd/Au(111) surfaces (Figure 5 (a)-(c)). More specifically, our simulations suggest that dopant dimer and trimer as well as island species are present in significant fractions on the aforementioned surfaces for $0.2 \leq \Omega_{CO} \leq 0.8$. The tendency of Ni atoms to form clusters is particularly pronounced as compared to Pd atoms on Pd/Ag(111) and Pd/Au(111). We note that this high tendency for Ni surface aggregation on Ni/Cu(111) alloys in the presence of CO is in qualitative agreement HREELS studies,[64] but also with very recent reflection adsorption infrared spectroscopy studies.[17,68] Thus, on Ni/Cu(111) at $\Omega_{CO} \approx 0.41$ we compute a relatively low fraction of monomers of approximately 0.39. Interestingly, in all three aforementioned cases the fraction of isolated monomers is minimal at a CO dopant fractional coverage of approximately 0.4.

Within the range $0.2 \leq \Omega_{CO} \leq 0.8$ there is also a noteworthy phase transition between $\overline{Y_{Dimers}}$ and $\overline{Y_{Trimers}}$, thereby indicating that one could favour the formation of a particular ensemble of dopant clusters by adjusting P_{CO}. For example, for the three aforementioned alloys, the highest possible fraction of trimers at 350 K is for $0.2 \leq \Omega_{CO} \leq 0.4$. More specifically, at $\Omega_{CO} \approx 0.2$ the fractions of dopant trimer clusters on Ni/Cu(111), Pd/Ag(111) and Pd/Au(111) are 0.21, 0.15 and 0.18, respectively, whilst the corresponding fractions of dopant dimers are 0.10, 0.09 and 0.06, respectively. By contrast, it is evident that the formation of dimers is promoted for $0.4 < \Omega_{CO} \leq 0.8$ and at $\Omega_{CO} \approx 0.6$, where the computed dimer fractions are in most

cases larger than the corresponding trimer fractions and are 0.26, 0.20 and 0.11 for Ni/Cu(111), Pd/Ag(111) and Pd/Au(111), respectively (Figure 5 (a)-(c)).

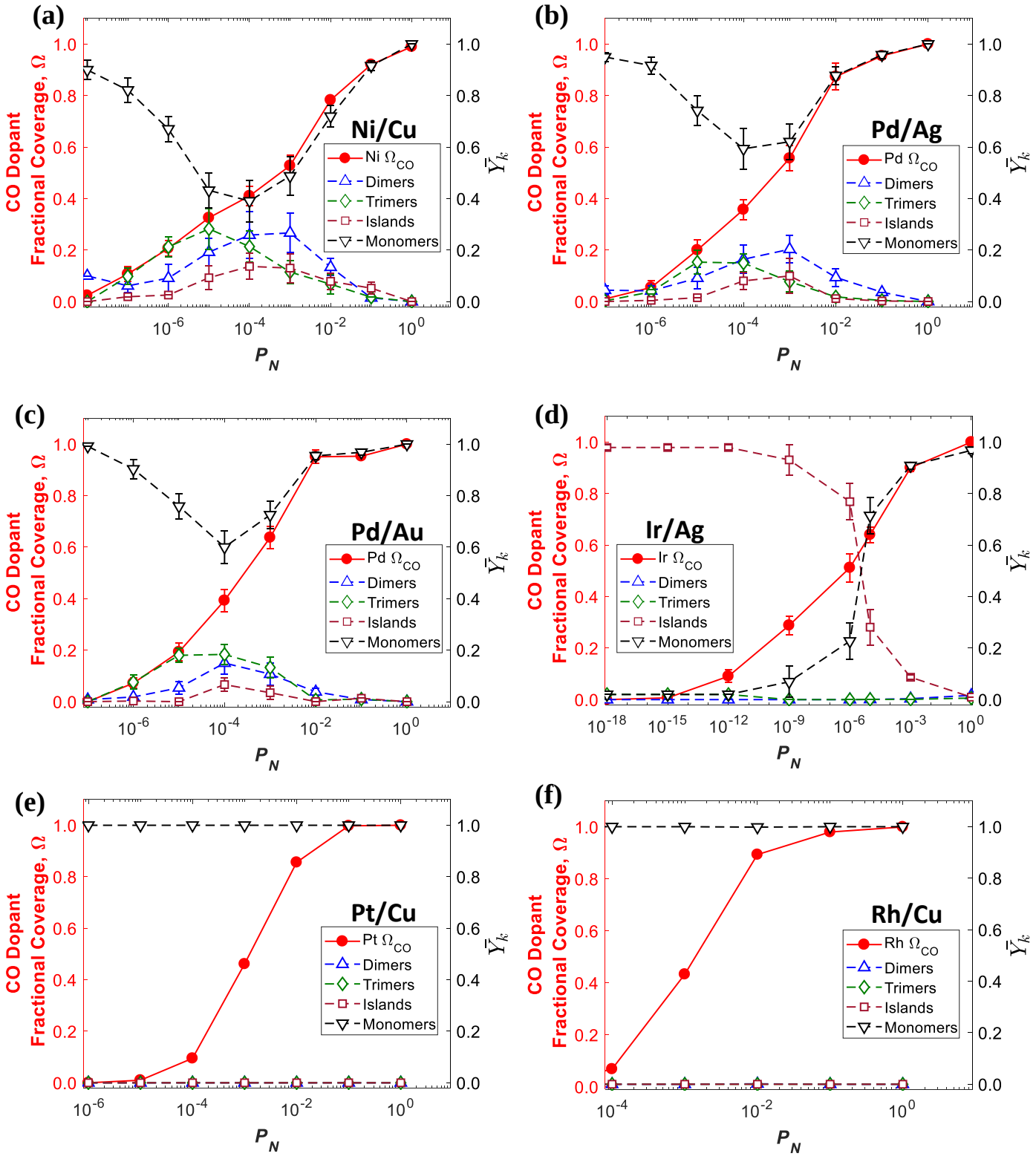

Figure 5. Fractions of surface species $\bar{Y}_k$ at 350 K at different values of the normalised pressure, P_N, for (a) Ni/Cu(111) (b) Pd/Ag(111) (c) Pd/Au(111) (d) Ir/Ag(111) (e) Pt/Cu(111) and (f) Rh/Cu(111). The left y-axis (red) shows the CO dopant fractional coverage, while the right y-axis (black) shows the fraction of different surface species. The dopant loading is 4 % in all cases and the error bars are ± one standard deviation.

The DFT-computed ΔE_{agg} for triangular trimer clusters on Ni/Cu(111), Pd/Ag(111) and Pd/Au(111) at Ω_{CO} = 0.33 are -0.36 eV, -0.29 eV and -0.34 eV, respectively.[13] These values are significantly more negative than the corresponding ΔE_{agg} for dimer clusters which are -0.15 eV, -0.14 eV and -0.14 eV for Ni/Cu(111),

Pd/Ag(111) and Pd/Au(111), respectively.[13] Accordingly, one would expect that trimer species will dominate over dimer and monomer species. However, our MC simulations (Figure 5 (a)-(c)) reveal that at similar Ω_{CO} (i.e. $0.2 < \Omega_{CO} < 0.3$) the fraction of monomer species is always larger than 0.52, being also larger than both $\overline{Y_{Dimers}}$ and $\overline{Y_{Trimers}}$. This result highlights the importance of coverage, configurational entropy and temperature effects, which can lead to the substantial population of states that are not the most enthalpically favoured.

Ir atoms in the Ir/Ag(111) surface have a high tendency to form islands at $\Omega_{CO} < 0.28$ (Figure 5 (d)). However, these Ir islands become gradually smaller for higher P_{CO} (i.e. Ω_{CO}), and the SAA phase is preferred for Ω_{CO} larger than 0.6. Contrary to the case of Ni/Cu(111), Pd/Ag(111) and Pd/Au(111) alloys, we observe a relatively sharp transition from a phase where island species prevail on the alloy surface to a phase where dopant atoms are isolated and occupied by CO. Remarkably, during this transition there is very limited, if any, formation of small Ir clusters (e.g. dimers and trimers). The absence of these small dopant clusters can be attributed to: (1) the more energetically favoured adsorption of CO on atop sites of Ir clusters as compared to hollow sites and (2) the very low stability of the SAA phase at low and intermediate CO dopant fractional coverages.[13,14]

Finally, we study the effect of Ω_{CO} into the restructuring of Rh/Cu(111) and Pt/Cu(111) alloy surfaces (Figure 5 (e) and (f)). DFT studies indicate that these alloys have a very strong enthalpic preference for the SAA phase, independently of the CO dopant fractional coverage.[13,14] In addition, the high stability of the SAA phase in Rh/Cu(111) and Pt/Cu(111) is underscored in recent works, which focus on Cu-based highly dilute alloys.[69,70] Indeed, the formation of dopant clusters in Rh/Cu and Pt/Cu is enthalpically unfavourable even in the presence of multi-dentate species (i.e. species that bind to more than one site upon adsorption) such as ethylene (C_2H_2).[70] These results are further supported by our MC simulations, where we find that within the range of $0.0 \leq \Omega_{CO} \leq 1.0$ the fraction of monomer species is always 1.0. Yet, we point out that Rh/Cu and Pt/Cu SAA catalysts are promising toward the efficient catalysis of numerous chemistries of practical interest,[1,16,45,71] and the formation of contiguous dopant sites may deteriorate their performance for certain applications. A typical example of such a reaction is the selective hydrogenation of 1,3-butadiene to butenes over Pt/Cu alloys,[16] where the formation of large Pt ensembles, at high Pt loadings (≈ 30 %), diminishes the selectivity toward butene in favour of butane.[16]

3.3. Temperature effects on the aggregation of dopant atoms

According to our discussion in the previous section, the maximum fractions of dopant dimers and trimers on Ni/Cu(111), Pd/Ag(111) and Pd/Au(111) surfaces are noted for CO dopant fractional coverages within the range of 0.35 - 0.41 (~0.41, 0.36 and 0.39 for Ni/Cu(111), Pd/Ag(111) and Pd/Au(111)). In the current section, we look into the possibility of inducing further surface aggregation over these surfaces by exploiting synergistic effects between P_{CO} and temperature. The presence of large dopant ensembles may be crucial in order to obtain high catalytic activity for reactions that involve C-C scission, like hydrogenolysis reactions.[72] We perform MC simulations within the temperature range of 290 K - 350 K, while adjusting P_{CO} such that

Ω_{CO} remains in the region of maximum dopant aggregation. Similarly to the calculations presented in the previous section, the dopant loading is always fixed at 4% and the result is shown in Figure 6.

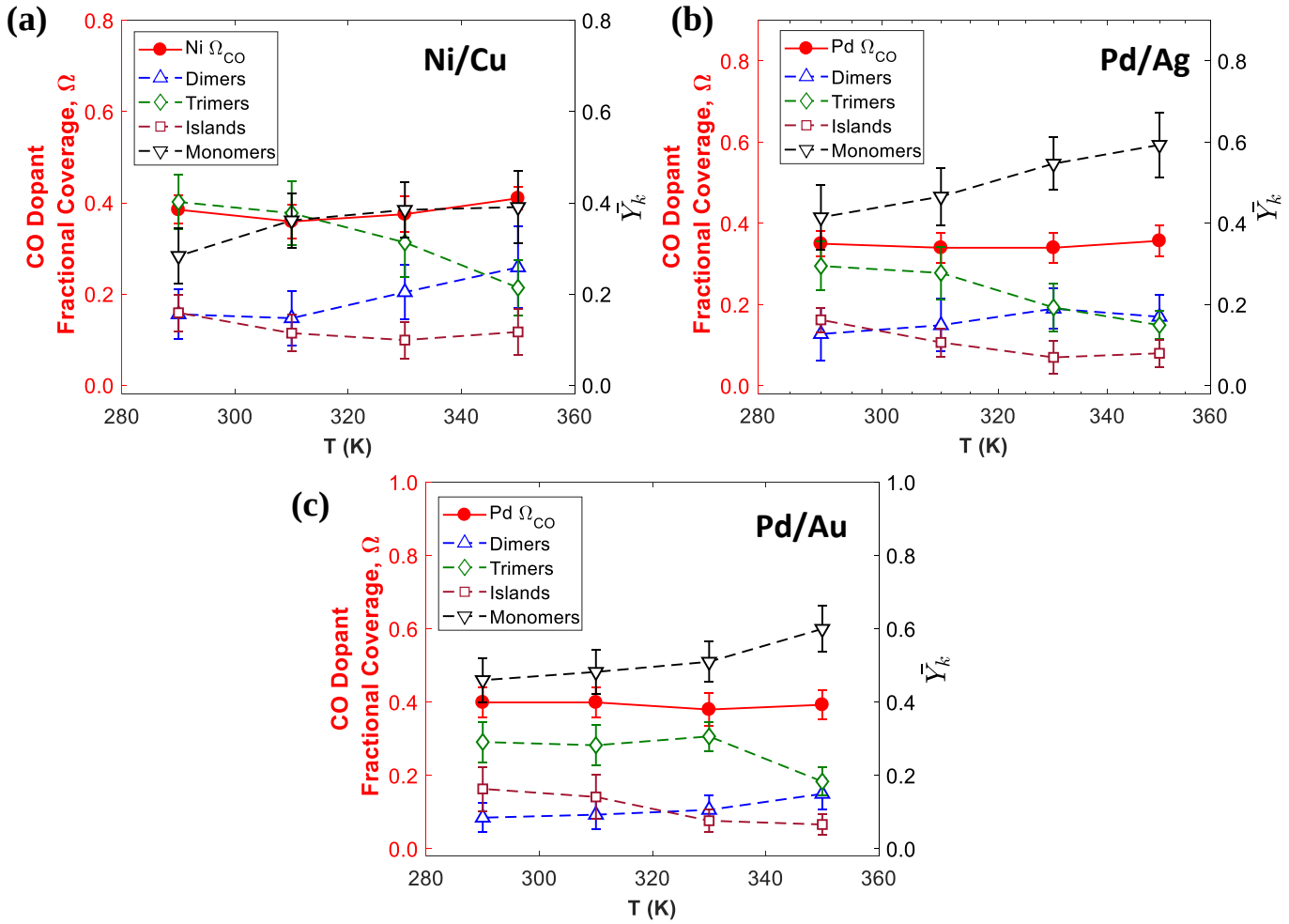

Figure 6. Fractions of surface species $\bar{Y}_k$ at various temperatures within the range of 290 K – 350 K for (a) Ni/Cu(111) (b) Pd/Ag(111) and (c) Pd/Au(111). The left y-axis (red) shows the CO dopant fractional coverage Ω_{CO}, while the right y-axis (black) shows the fraction of different surface species. The CO dopant fractional coverage remains in the vicinity of 0.4, where the maximum amount of dopant aggregation was observed at 350 K. The dopant loading is 4 % in all cases and the error bars are ± one standard deviation.

In general, we determine that $\overline{Y_{Monomers}}$ increases when the simulation temperature is increased from 290 K to 350 K, and the lowest $\overline{Y_{Monomers}}$ is observed for Ni/Cu(111) at 290 K, where $\overline{Y_{Monomers}} < 0.30$ (Figure 6 (a)). This trend exhibited by $\overline{Y_{Monomers}}$ can be explained by the increasing population of the most energetically favourable configurations at lower temperatures, i.e. dopant trimers with a CO adsorbed on the threefold site (see Ref. 13). Yet, we notice that monomers are not the only species whose number diminishes at lower temperature (Figure 6). A similar trend at decreasing temperature is observed in the fraction of dimer species (Figure 6). The most significant reduction in the number of dimer species is seen for Pd/Au(111), where at 350 K we compute $\overline{Y_{Dimers}} \approx 0.15$, whilst the corresponding fraction at 290 K is ca. 0.07 (Figure 6 (c)).

By contrast, at a decreasing temperature from 350 K to 290 K there is an increase in the number of islands and trimer species for all the alloy surfaces (Figure 6). At 290 K, we determine that the fraction of islands becomes significant in all cases with $\overline{Y_{Islands}}$ = 0.15, 0.16, and 0.16 for Ni/Cu(111), Pd/Au(111) and

Pd/Ag(111), respectively(Figure 6 (a) and (b)). Under these circumstances, the fraction of trimer species on Pd/Au(111) is considerable (ca. 0.30), whilst the corresponding fraction of monomers is significantly reduced to values lower than 0.5. These observations can be put in context, by considering the dissociation of O_2 as an exemplar case of an ensemble-sensitive reaction, toward which trimers are known to be active.[20] Thus, the Pd/Au(111) surface could be engineered, under the aforementioned conditions, towards a trimer-abundant structure, which would promote O_2 dissociation. Furthermore, we observe that at the same temperature (290 K), trimer species dominate the Ni/Cu(111) surface as well, with a fraction of 0.41, which is considerably larger than the corresponding fraction of single atoms ($\overline{Y_{Monomers}}$ = 0.28). This result highlights the potential of inducing further aggregation on the highly dilute alloy surface by taking the advantage of the synergy between *P*co and temperature.

As a final remark, we point out that our approach examines the thermodynamic stability of surface species and is based on assumptions that should be kept in mind upon comparison of these results to experimental findings. We point out that in an experiment, there might be kinetic limitations that are not accounted for herein. For example, we showed that on a Rh/Cu(111) surface, Rh atoms tend to be isolated. This, however, does not exclude the existence of dimer (or even trimer) species as a result of kinetic trapping. Similarly, the formation of contiguous dopant sites might be prevented because of kinetic limitations at low temperatures.[35] We note, however, that the inclusion of kinetic aspects to our models is part of ongoing work.

Moreover, we have assumed that after deposition to the (111) host metal surface, the dopant atoms remain on the surface layer due to the high activation barriers for the diffusion of dopant atoms from the surface layer to the bulk;[13] indeed in the presence of CO dopant atoms are more stable on the surface layer than in the bulk.[13,14] Nonetheless, these high activation barrier may be overcome at conditions of industrial relevance (e.g. high temperatures), thereby leading to the segregation of dopant atoms into the bulk.[33,64] For instance, Garfunkel and coworkers[58] estimated that a large amount of Ni (i.e. 55 - 75%) segregates into the bulk when Ni deposition on a Cu(111) happens 475 K. On the other hand, the same work showed that the vast majority on Ni remained on the surface layer when Ni was deposited at 420 K and below, in line with our assumption of insignificant dopant segregation to the bulk.

4. Conclusions

We have presented a methodology that allows us to study the surface aggregation of PGM atoms on highly dilute alloy surfaces. By employing DFT calculations and MC simulation in conjunction with the CE Hamiltonian method, we have studied the surface aggregation of dopant atoms on several highly dilute alloy (111) surfaces, under vacuum conditions and in the presence of CO. We focused our attention to dilute alloys (i.e. dopant loadings up to 4 %), which are promising for the catalysis of numerous chemistries of practical interest.[1,16,22]

The effect of dopant loading on surface aggregation was studied under vacuum conditions within the range of 1 - 4%. Under these conditions, Pd/Au(111), Pt/Cu(111) and Rh/Cu(111) systems show a notable preference for the SAA phase with dispersed PGM atoms within the surface of the host metal, whilst at 4 %

Pd loading we simulated a dimer fraction of 5 % on the Pd/Ag(111) surface. Although DFT calculations suggest that isolated Ni atoms on the Ni/Cu(111) surface will be as stable as Ni-Ni dimers and triangular trimer species,[13] our MC calculations showed that the SAA phase prevails on this surface. This difference is ascribed to coverage, temperature and configurational entropy effects, which effectively promote the SAA structure, owing to its higher disorder as compared to dopant cluster formation. Undoubtedly, these effects are important and are explicitly treated in MC simulations. Finally, Ir atoms on the Ir/Ag(111) surface tend to aggregate, thereby forming islands and a very small number of Ir trimers.

Subsequently, we have performed simulations to explore the possibility of manipulating the trends observed under vacuum conditions by exposing the catalytic surfaces to CO. We noted that on Pd/Au(111), Pd/Ag(111) and Ni/Cu(111) surfaces there is an extensive formation of dimers, trimers and small islands for $0.2 \leq \Omega_{CO} \leq 0.8$, and further surface aggregation can be induced by lowering the temperature. At Ω_{CO} smaller than 0.2 and larger than 0.8 the SAA phase is promoted in all three surfaces. Interestingly, we have shown that when $0.2 \leq \Omega_{CO} \leq 0.4$, there is a thermodynamic driving force for the formation of trimer species, whereas the formation of dimer species, which are highly active toward the dissociation of O_2,[20] is promoted for $0.4 < \Omega_{CO} \leq 0.8$. On the other hand, the presence of CO was found to be ineffective toward inducing the formation of small dopant clusters on the Ir/Ag(111), Pt/Cu(111) and Rh/Cu(111) surfaces. Regardless of the CO dopant fractional coverage, the PGM atoms remain atomically disperse in the two aforementioned Cu-based alloy surfaces. By contrast, at low Ω_{CO} (< 0.2) there are only Ir islands on the Ir/Ag(111) surface. The number of Ir islands diminishes gradually at increasing Ω_{CO}, before a sharp transition to the SAA phase, which dominates at $\Omega_{CO} > 0.6$.

This work serves as a guide for the experimental synthesis and manipulation of highly dilute alloy surfaces under reactive environments. While adsorbate induced aggregation strategies have been successfully demonstrated in certain cases,[13,14,20] our calculations provide a "compass" by which one can navigate the vast design space that encompasses materials' structures and operating conditions (different alloy compositions, dopant coverages, temperature, and adsorbate chemical potential). Hence, our results provide valuable insight into fine-tuning the architecture of a range alloy surfaces and controlling the PGM ensemble size, which mediates adsorbate binding and catalytic performance.[73] Our *ab initio* statistical mechanics approach (combining DFT and MC calculations) can be readily applied to other bimetallic combinations and adsorbate species, thus serving as a proof of principle for the design of bespoke ensembles that can optimise catalytic performance for reactions of practical interest.

Supporting Information

Finite lattice size testing, figures included in the cluster expansions of this work, DFT geometries used for the fitting of the cluster expansions, Cook's distances, average properties in Monte Carlo simulations, calculation of pre-exponential ratios for CO diffusion, vibrational frequencies of CO adsorbed on different sites and maximum CO pressures used in the simulations, calculation of partition functions for CO adsorption/desorption, representative images of the DFT slab and Monte Carlo snapshots, electronic aspects

of surface aggregation, calculating the formation energy of a DFT geometry, Monte Carlo simulation bias testing.

Acknowledgement

M. T. D. is supported by the EPSRC Doctoral Prize Fellowship, grant reference number EP/N509577/1. The development of *Zacros* has been partially supported by the embedded Computer Science and Engineering (eCSE) program of the ARCHER UK National Supercomputing Service (grants eCSE01-001, eCSE10-8) and the Leverhulme Trust (grant RPG-2017-361). The authors gratefully acknowledge the use of the UCL High Performance Computing Facility Myriad@UCL and Grace@UCL in the completion of the simulations of this work. The authors are also grateful to the UK Materials and Molecular Modelling Hub for computational resources (HPC facility Thomas), which is partially funded by EPSRC (EP/P020194/1).

References

(1) Marcinkowski, M. D.; Darby, M. T.; Liu, J.; Wimble, J. M.; Lucci, F. R.; Lee, S.; Michaelides, A.; Flytzani-Stephanopoulos, M.; Stamatakis, M.; Sykes, E. C. H. Pt/Cu Single-Atom Alloys as Coke-Resistant Catalysts for Efficient C–H Activation. *Nat. Chem.* **2018**, *10*, 325–332.

(2) Nørskov, J. K.; Studt, F.; Abild-Pedersen, F.; Bligaard, T. The Electronic Factor in Heterogeneous Catalysis. In *Fundamental Concepts in Heterogeneous Catalysis*; John Wiley & Sons, Inc: Hoboken, NJ, USA, 2014; pp 114–137.

(3) Zhang, S.; Rong, H.; Yang, T.; Bai, B.; Zhang, J. Ultrafine PtRu Dilute Alloy Nanodendrites for Enhanced Electrocatalytic Methanol Oxidation. *Chem. Eur. J.* **2019**, *25*, 1–8.

(4) Wang, Z.-T.; Hoyt, R. A.; El-Soda, M.; Madix, R. J.; Kaxiras, E.; Sykes, E. C. H. Dry Dehydrogenation of Ethanol on Pt–Cu Single Atom Alloys. *Top. Catal.* **2018**, *61*, 328–335.

(5) Besenbacher, F. Design of a Surface Alloy Catalyst for Steam Reforming. *Science (80-.).* **1998**, *279*, 1913–1915.

(6) Meenakshisundaram, S.; Nowicka, E.; Miedziak, P. J.; Brett, G. L.; Jenkins, R. L.; Dimitratos, N.; Taylor, S. H.; Knight, D. W.; Bethell, D.; Hutchings, G. J. Oxidation of Alcohols Using Supported Gold and Gold–Palladium Nanoparticles. *Faraday Discuss.* **2009**, *145*, 341–356.

(7) Gao, F.; Wang, Y.; Goodman, D. W. Reaction Kinetics and Polarization-Modulation Infrared Reflection Absorption Spectroscopy (PM-IRAS) Investigation of CO Oxidation over Supported Pd - Au Alloy Catalysts. *J. Phys. Chem. C* **2010**, *114*, 4036–4043.

(8) Pei, G. X.; Liu, X. Y.; Wang, A.; Lee, A. F.; Isaacs, M. A.; Li, L.; Pan, X.; Yang, X.; Wang, X.; Tai, Z.; et al. Ag Alloyed Pd Single-Atom Catalysts for Efficient Selective Hydrogenation of Acetylene to Ethylene in Excess Ethylene. *ACS Catal.* **2015**, *5*, 3717–3725.

(9) Li, H.; Chai, W.; Henkelman, G. Selectivity for Ethanol Partial Oxidation: The Unique Chemistry of Single-Atom Alloy Catalysts on Au, Ag, and Cu(111). *J. Mater. Chem. A* **2019**, 23868–23877.

(10) Giannakakis, G.; Trimpalis, A.; Shan, J.; Qi, Z.; Cao, S.; Liu, J.; Ye, J.; Biener, J.; Flytzani-

Stephanopoulos, M. NiAu Single Atom Alloys for the Non-Oxidative Dehydrogenation of Ethanol to Acetaldehyde and Hydrogen. *Top. Catal.* **2018**, *61*, 475–486.

(11) Tierney, H. L.; Baber, A. E.; Kitchin, J. R.; Sykes, E. C. H. Hydrogen Dissociation and Spillover on Individual Isolated Palladium Atoms. *Phys. Rev. Lett.* **2009**, *103*, 246102.

(12) Darby, M. T.; Stamatakis, M.; Michaelides, A.; Sykes, E. C. H. Lonely Atoms with Special Gifts: Breaking Linear Scaling Relationships in Heterogeneous Catalysis with Single-Atom Alloys. *J. Phys. Chem. Lett.* **2018**, *9*, 5636–5646.

(13) Darby, M. T.; Sykes, E. C. H.; Michaelides, A.; Stamatakis, M. Carbon Monoxide Poisoning Resistance and Structural Stability of Single Atom Alloys. *Top. Catal.* **2018**, *61*, 428–438.

(14) Papanikolaou, K. G.; Darby, M. T.; Stamatakis, M. CO-Induced Aggregation and Segregation of Highly Dilute Alloys : A Density Functional Theory Study. *J. Phys. Chem. C* **2019**, *123*, 9128–9138.

(15) Nørskov, J. K.; Studt, F.; Abild-Pedersen, F.; Bligaard, T. Activity and Selectivity Maps. In *Fundamental Concepts in Heterogeneous Catalysis*; John Wiley & Sons, Inc: Hoboken, NJ, USA, 2014; pp 97–113.

(16) Lucci, F. R.; Liu, J.; Marcinkowski, M. D.; Yang, M.; Allard, L. F.; Flytzani-Stephanopoulos, M.; Sykes, E. C. H. Selective Hydrogenation of 1,3-Butadiene on Platinum–Copper Alloys at the Single-Atom Limit. *Nat. Commun.* **2015**, *6*, 8550.

(17) Lucci, F. R.; Darby, M. T.; Mattera, M. F. G.; Ivimey, C. J.; Therrien, A. J.; Michaelides, A.; Stamatakis, M.; Sykes, E. C. H. Controlling Hydrogen Activation, Spillover, and Desorption with Pd–Au Single-Atom Alloys. *J. Phys. Chem. Lett.* **2016**, *7*, 480–485.

(18) Maroun, F.; Ozanam, F.; Magnussen, O. M.; R. J. Behm. The Role of Atomic Ensembles in the Reactivity of Bimetallic Electrocatalysts. **2001**, *293*, 1811–1815.

(19) Luo, K.; Wei, T.; Yi, C.-W.; Axnanda, S.; Goodman, D. W. Preparation and Characterization of Silica Supported Au−Pd Model Catalysts. *J. Phys. Chem. B* **2005**, *109*, 23517–23522.

(20) Ham, H. C.; Stephens, J. A.; Hwang, G. S.; Han, J.; Nam, S. W.; Lim, T. H. Role of Small Pd Ensembles in Boosting CO Oxidation in AuPd Alloys. *J. Phys. Chem. Lett.* **2012**, *3*, 566–570.

(21) Stakheev, A. Y.; Smirnova, N. S.; Markov, P. V.; Baeva, G. N.; Bragina, G. O.; Rassolov, A. V.; Mashkovsky, I. S. Adsorption-Induced Segregation as a Method for the Target-Oriented Modification of the Surface of a Bimetallic Pd–Ag Catalyst. *Kinet. Catal.* **2018**, *59*, 610–617.

(22) Vignola, E.; Steinmann, S. N.; Al Farra, A.; Vandegehuchte, B. D.; Curulla, D.; Sautet, P. Evaluating the Risk of C–C Bond Formation during Selective Hydrogenation of Acetylene on Palladium. *ACS Catal.* **2018**, *8*, 1662–1671.

(23) Saxena, S.; Khan, T. S.; Jalid, F.; Ramteke, M.; Haider, M. A. In Silico High Throughput Screening of Bimetallic and Single Atom Alloys Using Machine Learning and Ab Initio Microkinetic Modelling. *J. Mater. Chem. A* **2019**.

(24) Toyao, T.; Suzuki, K.; Kikuchi, S.; Takakusagi, S.; Shimizu, K.; Takigawa, I. Toward Effective

Utilization of Methane: Machine Learning Prediction of Adsorption Energies on Metal Alloys. *J. Phys. Chem. C* **2018**, *122*, 8315–8326.

(25) Liu, P.; Nørskov, J. K. Ligand and Ensemble Effects in Adsorption on Alloy Surfaces. *Phys. Chem. Chem. Phys.* **2001**, *3*, 3814–3818.

(26) Simonovis, J. P.; Hunt, A.; Palomino, R. M.; Senanayake, S. D.; Waluyo, I. Enhanced Stability of Pt-Cu Single-Atom Alloy Catalysts: In Situ Characterization of the Pt/Cu(111) Surface in an Ambient Pressure of CO. *J. Phys. Chem. C* **2018**, *122*, 4488–4495.

(27) Nørskov, J. K.; Studt, F.; Abild-Pedersen, F.; Bligaard, T. The Potential Energy Diagram. In *Fundamental Concepts in Heterogeneous Catalysis*; John Wiley & Sons, Inc: Hoboken, NJ, USA, 2014; pp 6–25.

(28) Wang, G.; Van Hove, M. A.; Ross, P. N.; Baskes, M. I. Monte Carlo Simulations of Segregation in Pt-Re Catalyst Nanoparticles. *J. Chem. Phys.* **2004**, *121*, 5410–5422.

(29) Divi, S.; Chatterjee, A. Understanding Segregation Behavior in AuPt, NiPt, and AgAu Bimetallic Nanoparticles Using Distribution Coefficients. *J. Phys. Chem. C* **2016**, *120*, 27296–27306.

(30) Yuge, K.; Seko, A.; Kuwabara, A.; Oba, F.; Tanaka, I. First-Principles Study of Bulk Ordering and Surface Segregation in Pt-Rh Binary Alloys. *Phys. Rev. B* **2006**, *74*, 174202.

(31) Taylor, M. G.; Mpourmpakis, G. Rethinking Heterometal Doping in Ligand-Protected Metal Nanoclusters. *J. Phys. Chem. Lett.* **2018**, *9*, 6773–6778.

(32) Yan, Z.; Taylor, M. G.; Mascareno, A.; Mpourmpakis, G. Size-, Shape-, and Composition-Dependent Model for Metal Nanoparticle Stability Prediction. *Nano Lett.* **2018**, *18*, 2696–2704.

(33) Andersson, K. J.; Calle-Vallejo, F.; Rossmeisl, J.; Chorkendorff, I. Adsorption-Driven Surface Segregation of the Less Reactive Alloy Component. *J. Am. Chem. Soc.* **2009**, *131*, 2404–2407.

(34) McCue, A. J.; Anderson, J. A. CO Induced Surface Segregation as a Means of Improving Surface Composition and Enhancing Performance of CuPd Bimetallic Catalysts. *J. Catal.* **2015**, *329*, 538–546.

(35) Zhu, B.; Thrimurthulu, G.; Delannoy, L.; Louis, C.; Mottet, C.; Creuze, J.; Legrand, B.; Guesmi, H. Evidence of Pd Segregation and Stabilization at Edges of AuPd Nano-Clusters in the Presence of CO: A Combined DFT and DRIFTS Study. *J. Catal.* **2013**, *308*, 272–281.

(36) Meng, J.; Zhu, B.; Gao, Y. Surface Composition Evolution of Bimetallic Alloys under Reaction Conditions. *J. Phys. Chem. C* **2019**.

(37) Zafeiratos, S.; Piccinin, S.; Teschner, D. Alloys in Catalysis: Phase Separation and Surface Segregation Phenomena in Response to the Reactive Environment. *Catal. Sci. Technol.* **2012**, *2*, 1787.

(38) Vignola, E.; Steinmann, S. N.; Le Mapihan, K.; Vandegehuchte, B. D.; Curulla, D.; Sautet, P. Acetylene Adsorption on Pd–Ag Alloys: Evidence for Limited Island Formation and Strong Reverse Segregation from Monte Carlo Simulations. *J. Phys. Chem. C* **2018**, *122*, 15456–15463.

(39) van Spronsen, M. A.; Daunmu, K.; O'Connor, C. R.; Egle, T.; Kersell, H.; Oliver-Meseguer, J.;

Salmeron, M. B.; Madix, R. J.; Sautet, P.; Friend, C. M. Dynamics of Surface Alloys: Rearrangement of Pd/Ag(111) Induced by CO and O2. *J. Phys. Chem. C* **2019**, *123*, 8312–8323.

(40) Ham, H. C.; Hwang, G. S.; Han, J.; Nam, S. W.; Lim, T. H. On the Role of Pd Ensembles in Selective H2O2 Formation on PdAu Alloys. *J. Phys. Chem. C* **2009**, *113*, 12943–12945.

(41) Zhu, B.; Creuze, J.; Mottet, C.; Legrand, B.; Guesmi, H. CO Adsorption-Induced Surface Segregation and Formation of Pd Chains on AuPd(100) Alloy: Density Functional Theory Based Ising Model and Monte Carlo Simulations. *J. Phys. Chem. C* **2016**, *120*, 350–359.

(42) Han, B. C.; Van der Ven, A.; Ceder, G.; Hwang, B. Surface Segregation and Ordering of Alloy Surfaces in the Presence of Adsorbates. *Phys. Rev. B* **2005**, *72*, 205409.

(43) Therrien, A. J.; Hensley, A. J. R.; Marcinkowski, M. D.; Zhang, R.; Lucci, F. R.; Coughlin, B.; Schilling, A. C.; Mcewen, J.; Sykes, E. C. H. An Atomic-Scale View of Single-Site Pt Catalysis for Low-Temperature CO Oxidation. *Nat. Catal.* **2018**, *1*, 192–198.

(44) Yao, Y.; Goodman, D. W. In Situ IR Spectroscopic Studies of Ni Surface Segregation Induced by CO Adsorption on Cu–Ni/SiO2 Bimetallic Catalysts. *Phys. Chem. Chem. Phys.* **2014**, *16*, 3823–3829.

(45) Liu, J.; Lucci, F. R.; Yang, M.; Lee, S.; Marcinkowski, M. D.; Therrien, A. J.; Williams, C. T.; Sykes, E. C. H.; Flytzani-Stephanopoulos, M. Tackling CO Poisoning with Single-Atom Alloy Catalysts. *J. Am. Chem. Soc.* **2016**, *138*, 6396–6399.

(46) Kresse, G.; Furthmüller, J. Efficiency of Ab-Initio Total Energy Calculations for Metals and Semiconductors Using a Plane-Wave Basis Set. *Comput. Mater. Sci.* **1996**, *6*, 15–50.

(47) Kresse, G.; Hafner, J. Ab Initio Molecular Dynamics for Liquid Metals. *Phys. Rev. B* **1993**, *47*, 558–561.

(48) Perdew, J. P.; Burke, K.; Ernzerhof, M. Generalized Gradient Approximation Made Simple. *Phys. Rev. Lett.* **1996**, *77*, 3865–3868.

(49) Stamatakis, M.; Vlachos, D. G. A Graph-Theoretical Kinetic Monte Carlo Framework for on-Lattice Chemical Kinetics A Graph-Theoretical Kinetic Monte Carlo Framework for on-Lattice. *J. Chem. Phys.* **2011**, *134*, 214115.

(50) Nielsen, J.; D'Avezac, M.; Hetherington, J.; Stamatakis, M. Parallel Kinetic Monte Carlo Simulation Framework Incorporating Accurate Models of Adsorbate Lateral Interactions. *J. Chem. Phys.* **2013**, *139*, 224706.

(51) Stamatakis, M. Zacros: advanced lattice-KMC simulation made easy http://tinyurl.com/zacroskmc.

(52) Papanikolaou, K. G.; Darby, M. T.; Stamatakis, M. Adlayer Structure and Lattice Size Effects on Catalytic Rates Predicted from KMC Simulations : NO Oxidation on Pt (111). *J. Chem. Phys.* **2018**, *149*, 184701.

(53) Jansen, A. P. J. *An Introduction to Kinetic Monte Carlo Simulations of Surface Reactions*; Lecture Notes in Physics; Springer Berlin Heidelberg: Berlin, Heidelberg, 2012; Vol. 856.

(54) Sanchez, J. M.; Ducastelle, F.; Gratias, D. Generalized Cluster Description of Multicomponent

Systems. *Phys. A Stat. Mech. its Appl.* **1984**, *128*, 334–350.

(55) Schmidt, D. J.; Chen, W.; Wolverton, C.; Schneider, W. F. Performance of Cluster Expansions of Coverage-Dependent Adsorption of Atomic Oxygen on Pt(111). *J. Chem. Theory Comput.* **2012**, *8*, 264–273.

(56) Walle, A.; Ceder, G. Automating First-Principles Phase Diagram Calculations. *J. Phase Equilibria* **2002**, *23*, 348–359.

(57) Wu, C.; Schmidt, D. J.; Wolverton, C.; Schneider, W. F. Accurate Coverage-Dependence Incorporated into First-Principles Kinetic Models: Catalytic NO Oxidation on Pt (111). *J. Catal.* **2012**, *286*, 88–94.

(58) Garfunkel, E.; Yu, M.; Yang, S.; Feng, X. A Mixed Cu–Ni Bridge Site for CO Adsorption. *J. Vac. Sci. Technol. A Vacuum, Surfaces, Film.* **1989**, *7*, 1579–1584.

(59) Sholl, D. S.; Steckel, J. A. DFT Calculations for Surfaces of Solids. In *Density Functional Theory: A Practical Introduction*; John Wiley & Sons, Inc.: Hoboken, NJ, USA, 2009; pp 83–112.

(60) Wang, W.; Wang, Z.; Wang, J.; Zhong, C.-J.; Liu, C.-J. Highly Active and Stable Pt-Pd Alloy Catalysts Synthesized by Room-Temperature Electron Reduction for Oxygen Reduction Reaction. *Adv. Sci.* **2017**, *4*, 1600486.

(61) Kyriakou, G.; Boucher, M. B.; Jewell, A. D.; Lewis, E. a; Lawton, T. J.; Baber, A. E.; Tierney, H. L.; Flytzani-Stephanopoulos, M.; Sykes, E. C. H. Isolated Metal Atom Geometries as a Strategy for Selective Heterogeneous Hydrogenations. *Science (80-.).* **2012**, *335*, 1209–1212.

(62) Shan, J.; Janvelyan, N.; Li, H.; Liu, J.; Egle, T. M.; Ye, J.; Biener, M. M.; Biener, J.; Friend, C. M.; Flytzani-Stephanopoulos, M. Selective Non-Oxidative Dehydrogenation of Ethanol to Acetaldehyde and Hydrogen on Highly Dilute NiCu Alloys. *Appl. Catal. B Environ.* **2017**, *205*, 541–550.

(63) Tierney, H. L.; Baber, A. E.; Sykes, E. C. H. Atomic-Scale Imaging and Electronic Structure Determination of Catalytic Sites on Pd/Cu Near Surface Alloys. *J. Phys. Chem. C* **2009**, *113*, 7246–7250.

(64) Yang, S.; Yu, M.; Meigs, G.; Feng, X. H.; Garfunkel, E. Nickel Monolayers on Copper Surfaces: CO Adsorption and Ni Diffusion. *Surf. Sci.* **1988**, *205*, L777–L785.

(65) Stephens, J. A.; Ham, H. C.; Hwang, G. S. Atomic Arrangements of AuPt/Pt(111) and AuPd/Pd(111) Surface Alloys: A Combined Density Functional Theory and Monte Carlo Study. *J. Phys. Chem. C* **2010**, *114*, 21516–21523.

(66) Michalka, J. R.; Gezelter, J. D. Island Formation on Pt/Pd(557) Surface Alloys in the Presence of Adsorbed CO: A Molecular Dynamics Study. *J. Phys. Chem. C* **2015**, *119*, 14239–14247.

(67) Meng, J.; Zhu, B.; Gao, Y. Surface Composition Evolution of Bimetallic Alloys under Reaction Conditions. *J. Phys. Chem. C* **2019**, In press.

(68) Patel, D. A.; Hannagan, R. T.; Kress, P. L.; Schilling, A. C.; Çınar, V.; Sykes, E. C. H. Atomic-Scale Surface Structure and CO Tolerance of NiCu Single-Atom Alloys. *J. Phys. Chem. C* **2019**, In press.

(69) Fu, Q.; Luo, Y. Catalytic Activity of Single Transition-Metal Atom Doped in Cu(111) Surface for Heterogeneous Hydrogenation. *J. Phys. Chem. C* **2013**, *117*, 14618–14624.

(70) Yang, K.; Yang, B. Surface Restructuring of Cu-Based Single-Atom Alloy Catalysts under Reaction Conditions: The Essential Role of Adsorbates. *Phys. Chem. Chem. Phys.* **2017**, *19*, 18010–18017.

(71) Darby, M. T.; Réocreux, R.; Sykes, E. C. H.; Michaelides, A.; Stamatakis, M. Elucidating the Stability and Reactivity of Surface Intermediates on Single-Atom Alloy Catalysts. *ACS Catal.* **2018**, *8*, 5038–5050.

(72) Sinfelt, J. H.; Carter, J. L.; Yates, D. J. C. Catalytic Hydrogenolysis and Dehydrogenation over Copper-Nickel Alloys. *J. Catal.* **1972**, *24*, 283–296.

(73) Li, H.; Shin, K.; Henkelman, G. Effects of Ensembles, Ligand, and Strain on Adsorbate Binding to Alloy Surfaces. *J. Chem. Phys.* **2018**, *149*, 174705.

Table of Contents Graphic

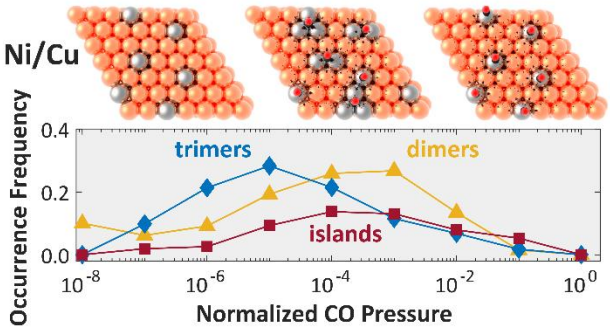

Supporting Information

Engineering the surface architecture of highly dilute alloys: an *ab initio* Monte Carlo approach

Konstantinos G. Papanikolaou, Matthew T. Darby and Michail Stamatakis*

Thomas Young Centre and Department of Chemical Engineering, University College London, Roberts Building, Torrington Place, London WC1E 7JE, UK

Corresponding Author: m.stamatakis@ucl.ac.uk

I. Finite lattice size effects

We perform preliminary lattice size testing on the Ni/Cu(111) and Pd/Ag(111) systems, in the presence and in the absence of CO.[1] In the latter case, we converge the average fraction of surface species (see the main text) with respect to the number of dopant atoms (Figure S1 (a)), whereas in the presence of CO we converge both the CO dopant fractional coverage (Figure S1 (b)) and the average fraction of surface species with respect to the same quantity as before (Figure S1 (c)).

For the lattice size testing under vacuum we choose the Ni/Cu(111) system (Figure S1 (a)) and this choice is not random. As shown in the main text, this surface is the one, whereon there is a formation of considerable amount of dopant dimer species under vacuum conditions and therefore this alloy is appropriate for testing purposes. In our test, we monitor the fractions of dopant atom surface species (i.e. dimers and monomers) for different numbers of lattice sites. Based on the result of this test (Figure S1 (a)), we choose lattices of 19,200 sites (i.e. 127 Ni atoms for 4% Ni) for our Monte Carlo (MC) simulations under vacuum conditions, thereby excluding lattice size effects and obtaining small standard deviations (Figure S1 (a)).

Along the same lines, we perform lattice size testing for our MC simulations under reactive conditions (i.e. in the presence of CO). We monitor how the CO dopant fractional coverage (on the Ni/Cu(111) surface) and the fractions of surface species (on the Pd/Ag(111) surface) converge at increasing lattice sizes, and the results are shown in Figure S1 (b) and Figure S1 (c), respectively. Our lattice size testing in the presence of CO (Figure S1 (b) and Figure S1 (c)) suggests that finite lattice size effects exist for lattices with a number of dopant atoms less than 50. On these small lattices, we note that the collected data exhibit a large variance (Figure S1 (b) and Figure S1 (c)). Accordingly, we choose a lattice with 50 dopant atoms for our simulations under reactive conditions.

Another important parameter to be considered for the MC simulations is the simulation duration (or walltime). In particular, the duration of the simulation must be long enough so that the stationary conditions are achieved. Under such conditions, we can obtain reliable estimates of the average number of species and the average CO dopant fractional coverage. In order to determine the walltime of our simulations, we perform a number of simulations with different walltimes, and monitor the average fraction of surface species (Figure S1 (d)). This test is done on the Pd/Ag(111) alloy and shows that the average species fractions are converged for tested walltimes larger than 24 hrs (Figure S1 (d)). We choose a walltime of 30 hrs for our simulations and the number of MC snapshots collected throughout the simulation is in the range of 500 – 600. We point out that the result of each simulation is in all cases carefully monitored, in order to assure that the average quantities (i.e. species fractions, CO coverage) are computed after having reached stationary conditions (see e.g. section V).

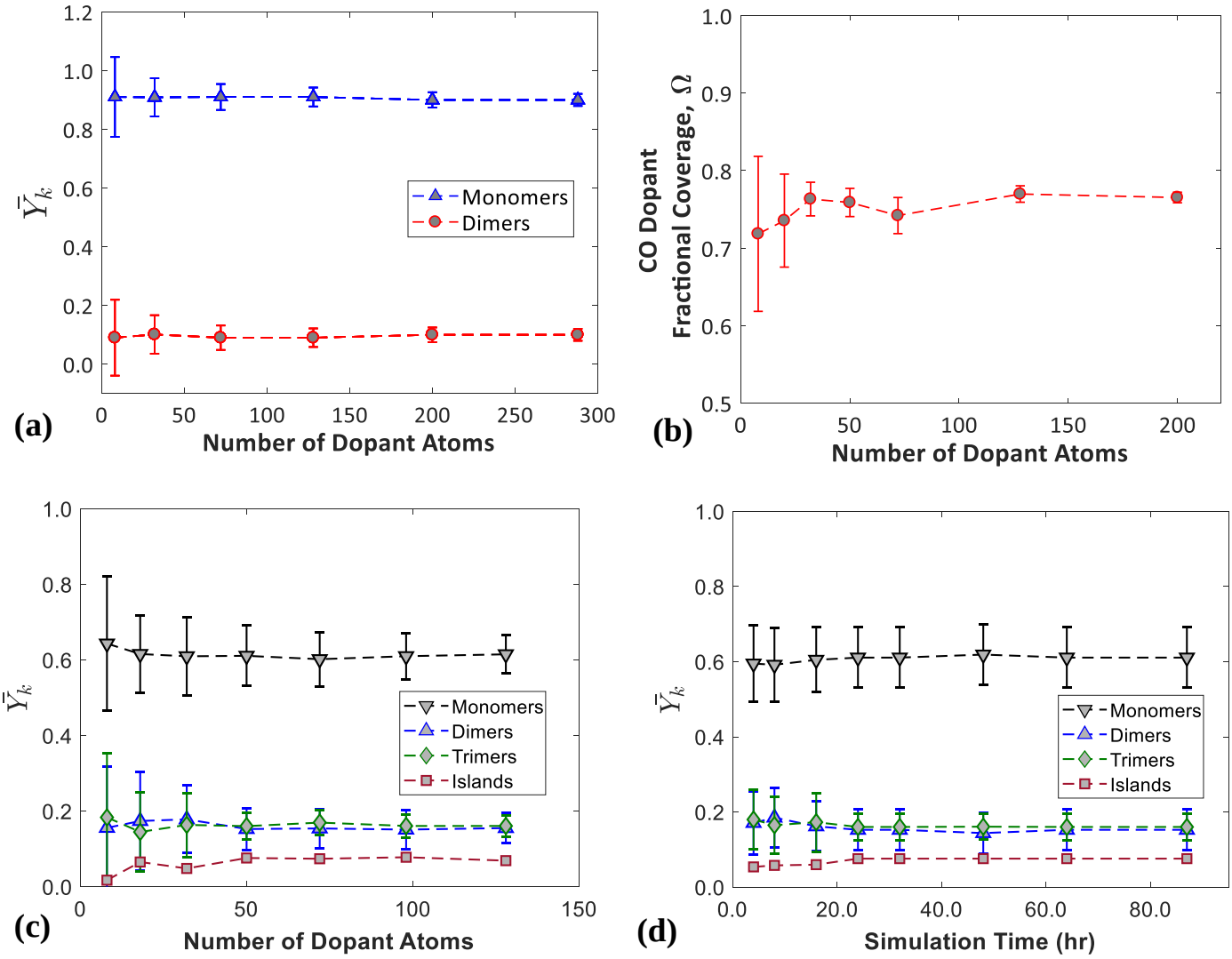

Figure S1. (a) Lattice size testing performed on the Ni/Cu(111) alloy under vacuum conditions and for 4% Ni loading. (b) Lattice size testing performed on the Ni/Cu(111) alloy in the presence of CO at $P_N = 0.01$ (for the definition of P_N see the main text) and for 4 % Ni loading. (c) Lattice size testing performed on the Pd/Ag(111) alloy in the presence of CO and $P_N = 10^{-4}$. Note that at this CO pressure the induced aggregation is maximum (see the main text). (d) Walltime testing on the Pd/Ag(111) alloy in the presence of CO and $P_N = 10^{-4}$. The error bars in all panels are ± one standard deviation.

II. Figures included in the cluster expansions

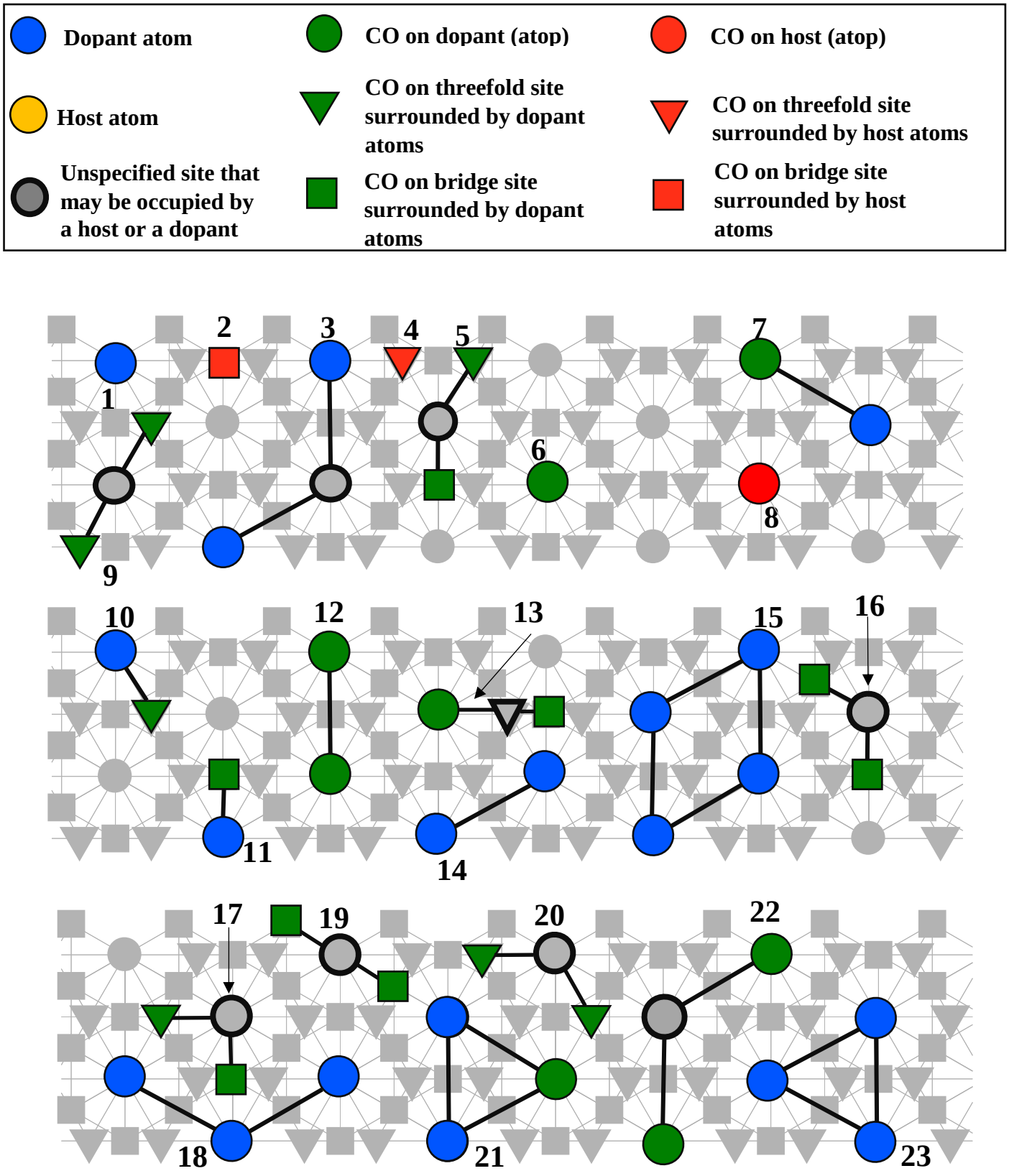

Figure S2. All different figures that may be included in the cluster expansions (CEs) of the investigated alloys. Note that the CO adsorbates on the host bridge sites and on the dopant bridge sites are represented by one species in the CE, but we use two different colours for clarity in the figure above. Thus, in the simulation, the "extra stability" of CO on dopant bridge is modelled by attractive interactions of cluster 11, respectively. This scheme is inspired by previously used approaches in different context (see e.g. models developed by Zhdanov).[2] Similarly for the CO threefold configurations. The legend above the figure shows how different species are represented.

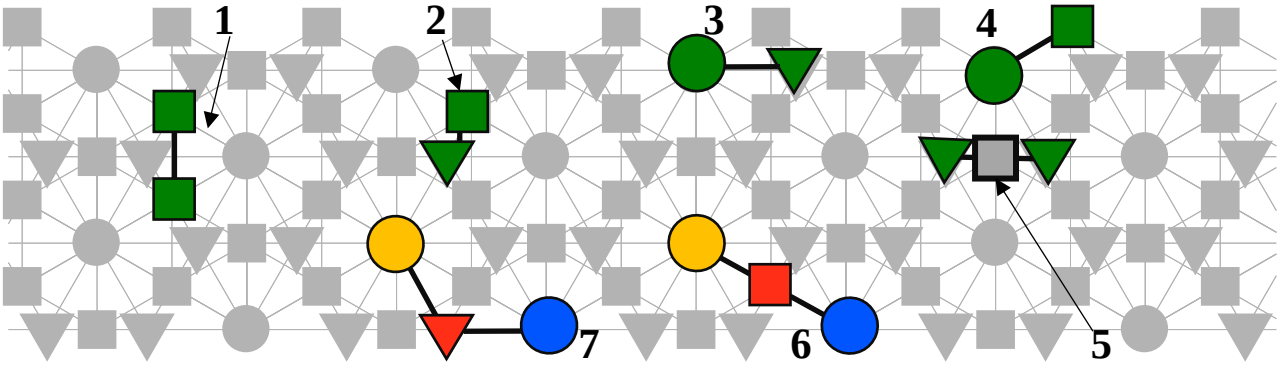

Figure S3. Unstable configurations whose formation is eliminated in the MC simulations for all alloys by assigning a large effective cluster interaction parameter of 10.0 eV. Patterns 6 and 7 represent mixed bridge and threefold adsorption sites. The legend above Figure S2 shows how different species are represented.

Table S1. Effective cluster interaction (ECI) parameters and their graph multiplicities (GM). This table shows which clusters were used in the cluster expansion of each of the investigated alloys along with the corresponding ECI and GM. The cluster numbering is shown in Figure S2. A dash indicates that the specific cluster was not used in the specific case.

Pattern	**Ni/Cu(111)**		**Rh/Cu(111)**		**Pt/Cu(111)**		**Pd/Au(111)**		**Pd/Ag(111)**		**Ir/Ag(111)**	
	GM	ECI (eV)	GM	ECI (eV)	GM	ECI (eV)	GM	ECI (eV)	GM	ECI (eV)	GM	ECI (eV)
1	1	-0.002	1	0.01	1	-0.02	1	-0.005	1	-0.01	1	-0.01
2	1	-0.44	1	-0.44	1	-0.44	1	-0.03	1	-0.04	1	-0.03
3	-	-	2	-0.008	2	0.03	2	-0.01	2	0.01	2	-0.02
4	1	-0.48	1	-0.49	1	-0.49	1	-0.05	1	0.07	1	-0.04
5	2	0.18	2	0.29	2	0.34	2	0.12	2	0.22	-	-
6	1	-1.33	1	-1.65	1	-1.15	1	-0.87	1	-0.96	1	-2.4
7	-	-	2	0.31	2	0.22	2	0.04	2	0.06	2	-0.13
8	-	-	-	-	-	-	1	-0.02	1	0.01	1	-0.01
9	2	0.05	-	-	-	-	2	0.05	2	-0.003	2	-0.65
10	1	-0.42	1	-0.42	1	-0.19	1	-0.47	1	-0.49	1	0.04
11	1	-0.54	1	-0.59	1	-0.30	1	-0.53	1	-0.61	1	0.01
12	2	0.11	2	0.33	2	0.36	2	0.11	2	0.16	2	0.08
13	2	0.38	2	0.53	2	0.56	2	0.21	2	0.26	2	0.75
14	2	0.01	2	0.10	2	0.19	2	0.08	2	0.03	2	-0.41
15	-	-	-	-	-	-	-	-	-	-	4	-0.18
16	2	0.19	2	0.26	2	0.25	2	0.19	2	0.25	2	0.29
17	1	0.38	1	0.50	-	-	1	0.23	-	-	-	-
18	-	-	2	-0.03	-	-	-	-	-	-	2	0.20
19	2	0.08	2	-0.06	2	0.06	2	0.03	2	0.11	2	0.29
20	2	0.24	-	-	-	-	2	0.12	2	0.12	-	-
21	-	-	6	-0.05	6	-0.06	6	-0.02	6	-0.03	-	-
22	-	-	2	0.02	2	0.05	-	-	-	-	-	-
23	-	-	-	-	6	0.005	-	-	-	-	6	0.41

III. DFT geometries used in fitting the cluster expansions

In the following images empty sites are shown in grey, sites occupied by host metal atoms in yellow, sites occupied by dopant atoms in blue, top sites of dopant atoms occupied by CO or hollow/bridge sites surrounded by dopant atoms occupied by CO in green, and top sites of host atoms occupied by CO or hollow/bridge sites surrounded by host atoms occupied by CO are shown in red. The markers used for different site types are as follows: circle for atop, square for bridge, triangle for hollow.

The geometries added in our DFT dataset are those extensively formed on the MC lattice during simulation. These structures contain small dopant clusters that, however, can resolve patterns of arbitrary complexity formed on the lattice.

- **Ni/Cu(111)**

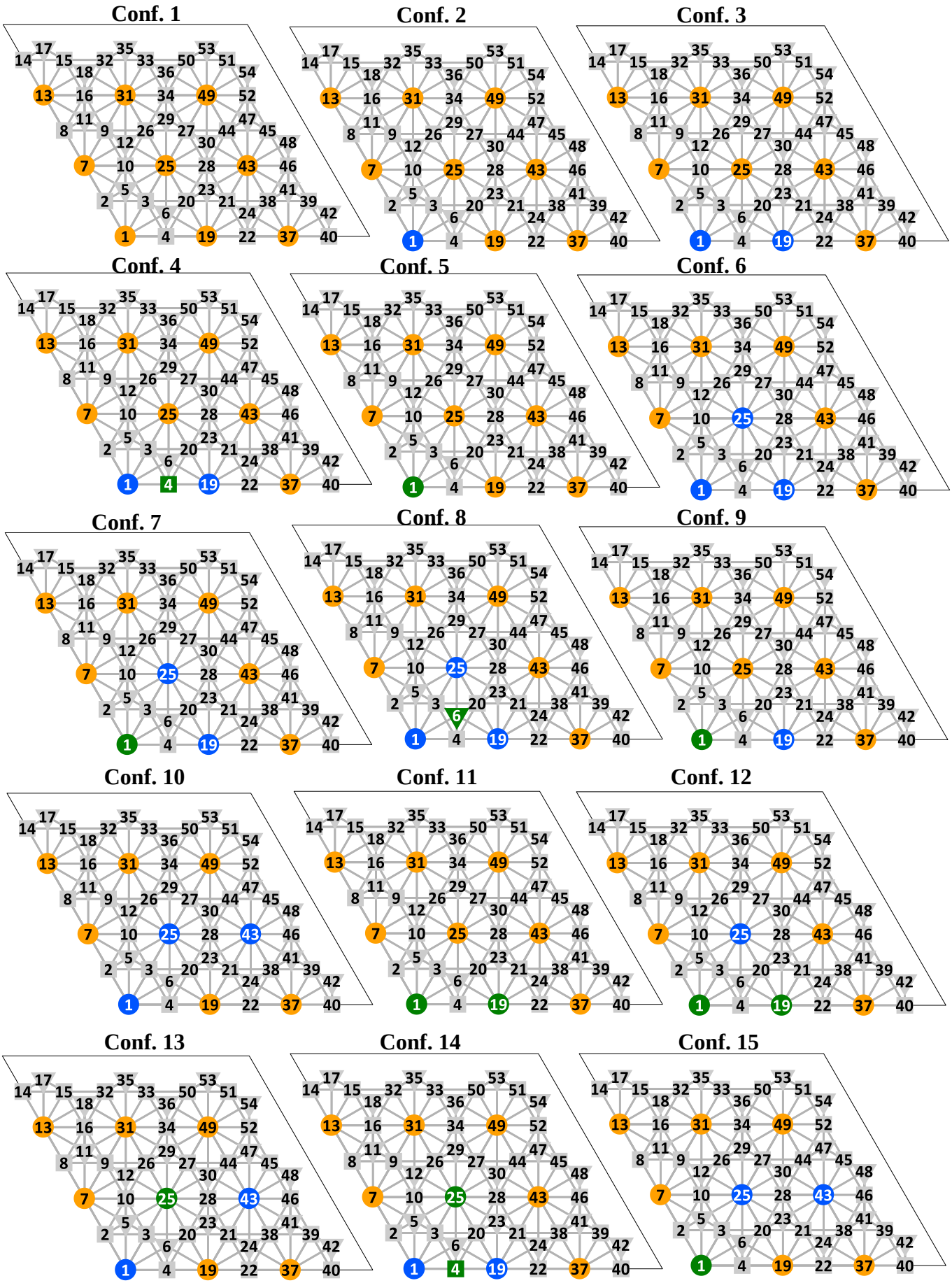

Continues

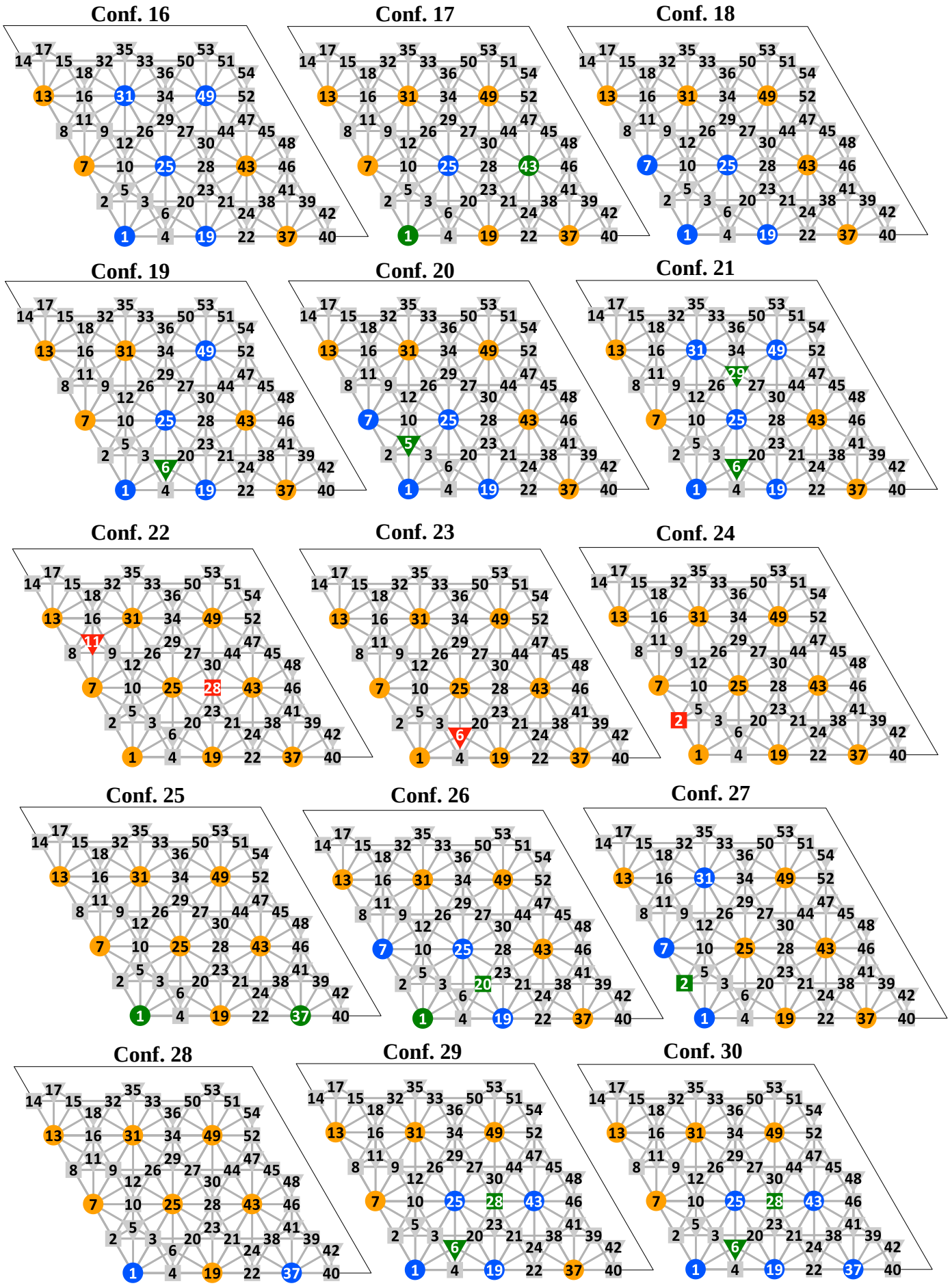
Conf. 16
Conf. 17
Conf. 18
Conf. 19
Conf. 20
Conf. 21
Conf. 22
Conf. 23
Conf. 24
Conf. 25
Conf. 26
Conf. 27
Conf. 28
Conf. 29
Conf. 30

Continues

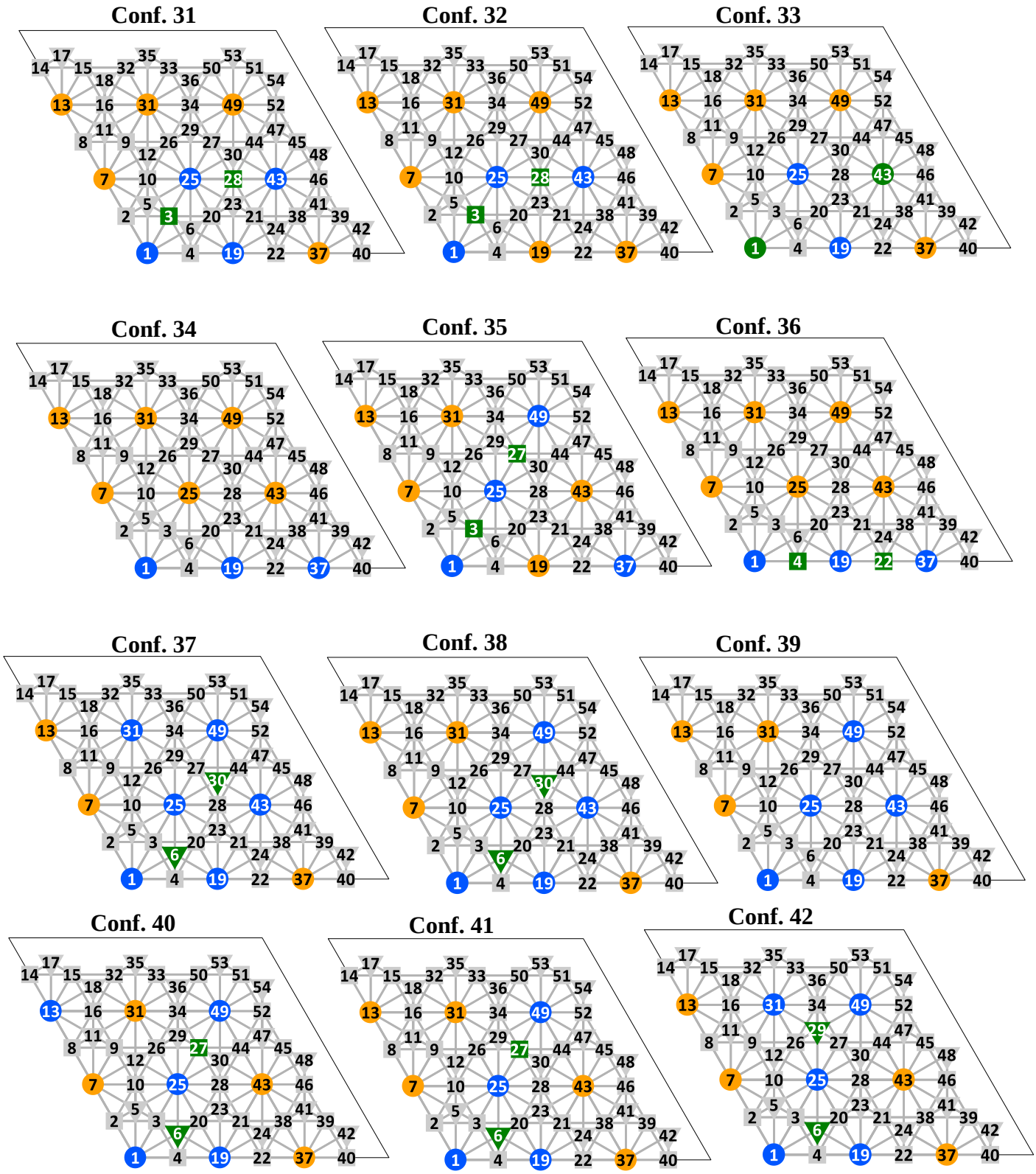

Figure S4. DFT geometries used in the cluster expansion of the Ni/Cu(111) system.

- **Rh/Cu(111)**

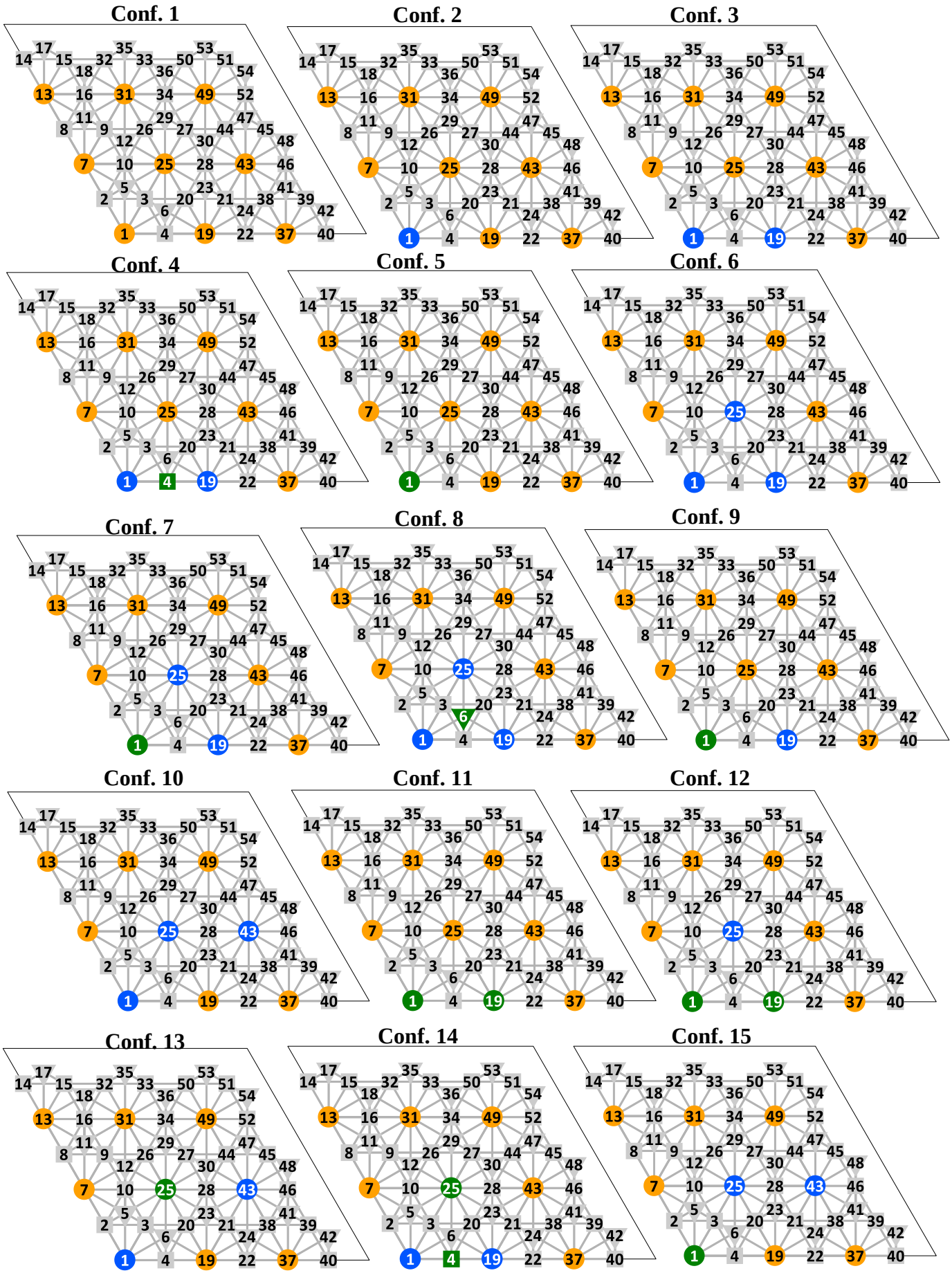

Continues

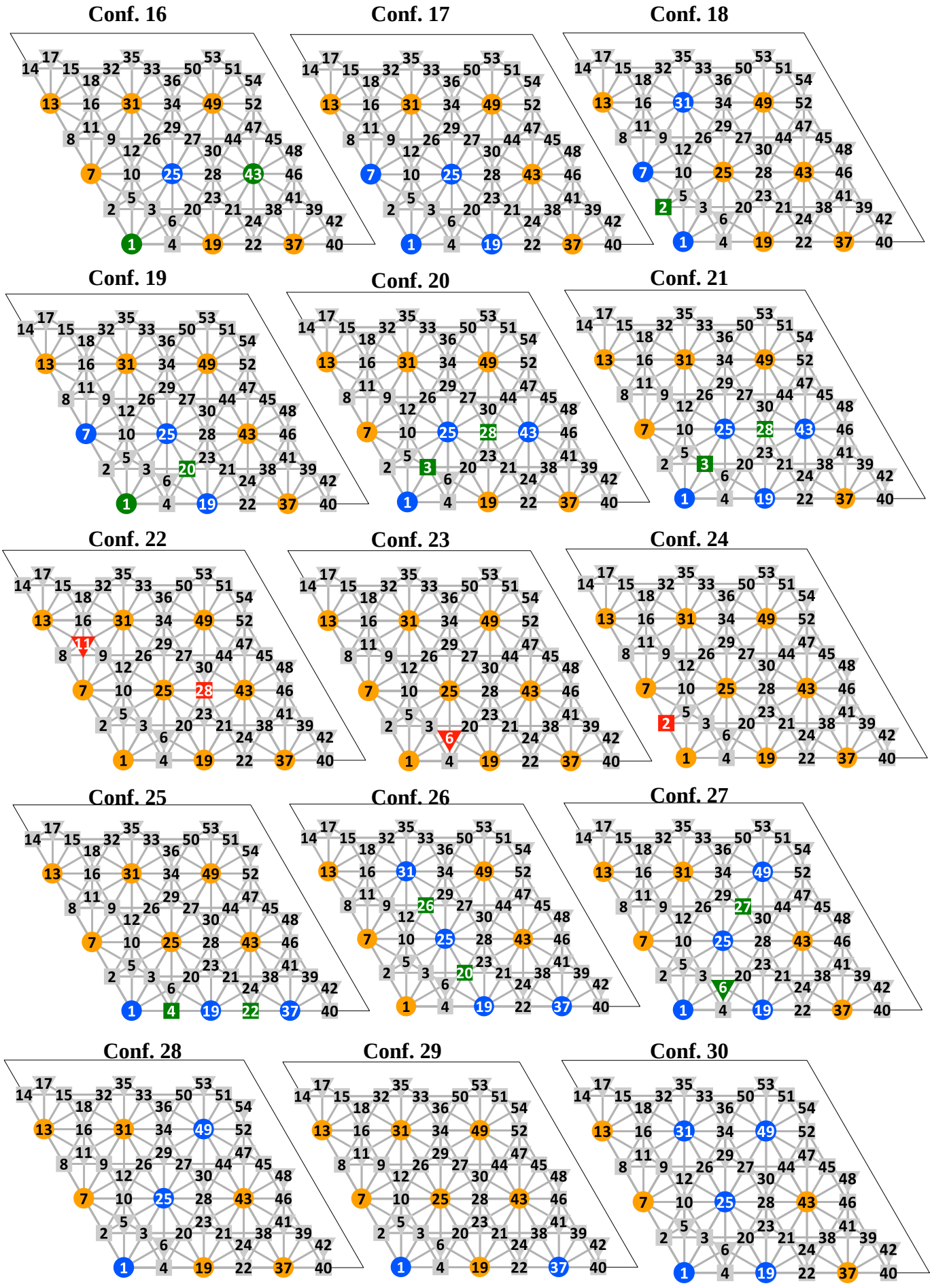
Conf. 16
Conf. 17
Conf. 18
Conf. 19
Conf. 20
Conf. 21
Conf. 22
Conf. 23
Conf. 24
Conf. 25
Conf. 26
Conf. 27
Conf. 28
Conf. 29
Conf. 30

Continues

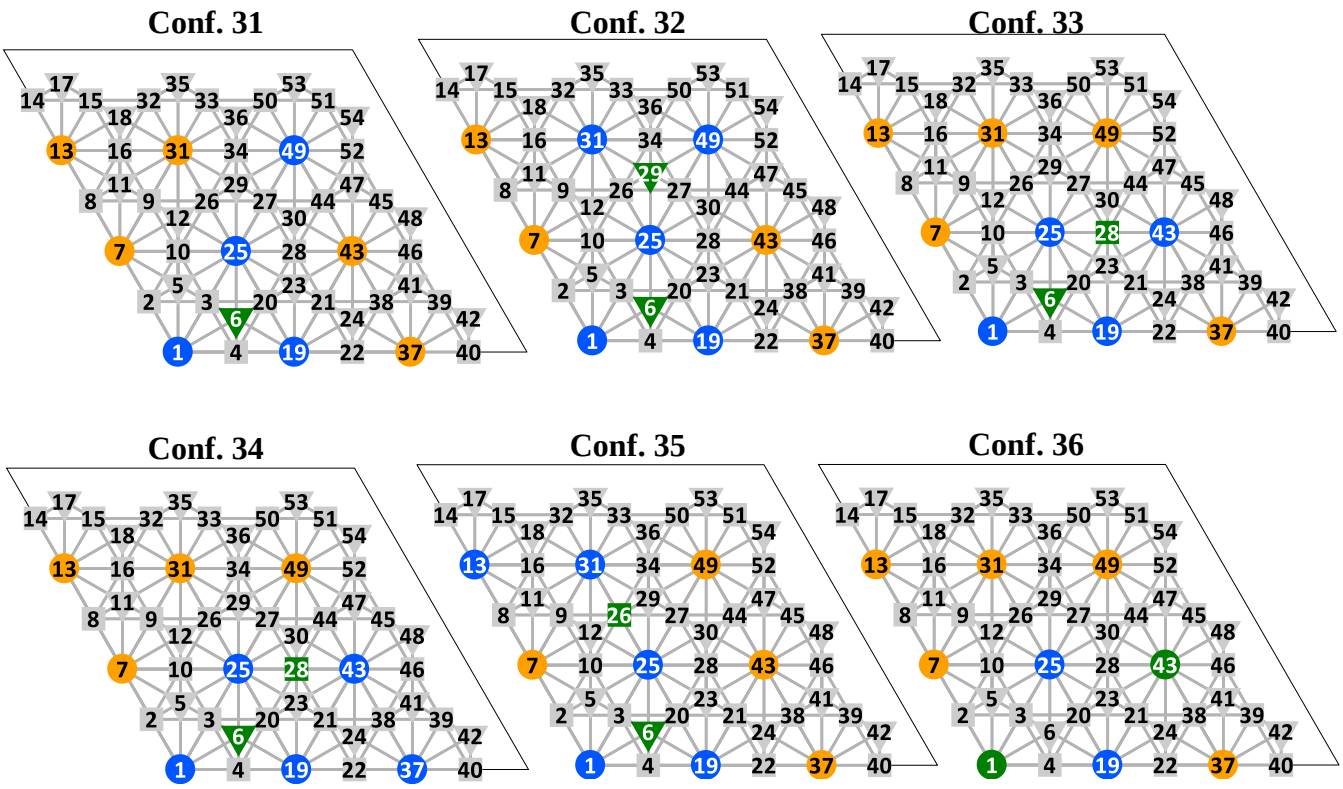

Figure S5. DFT geometries used in the cluster expansion of the Rh/Cu(111) system.

- **Pt/Cu(111)**

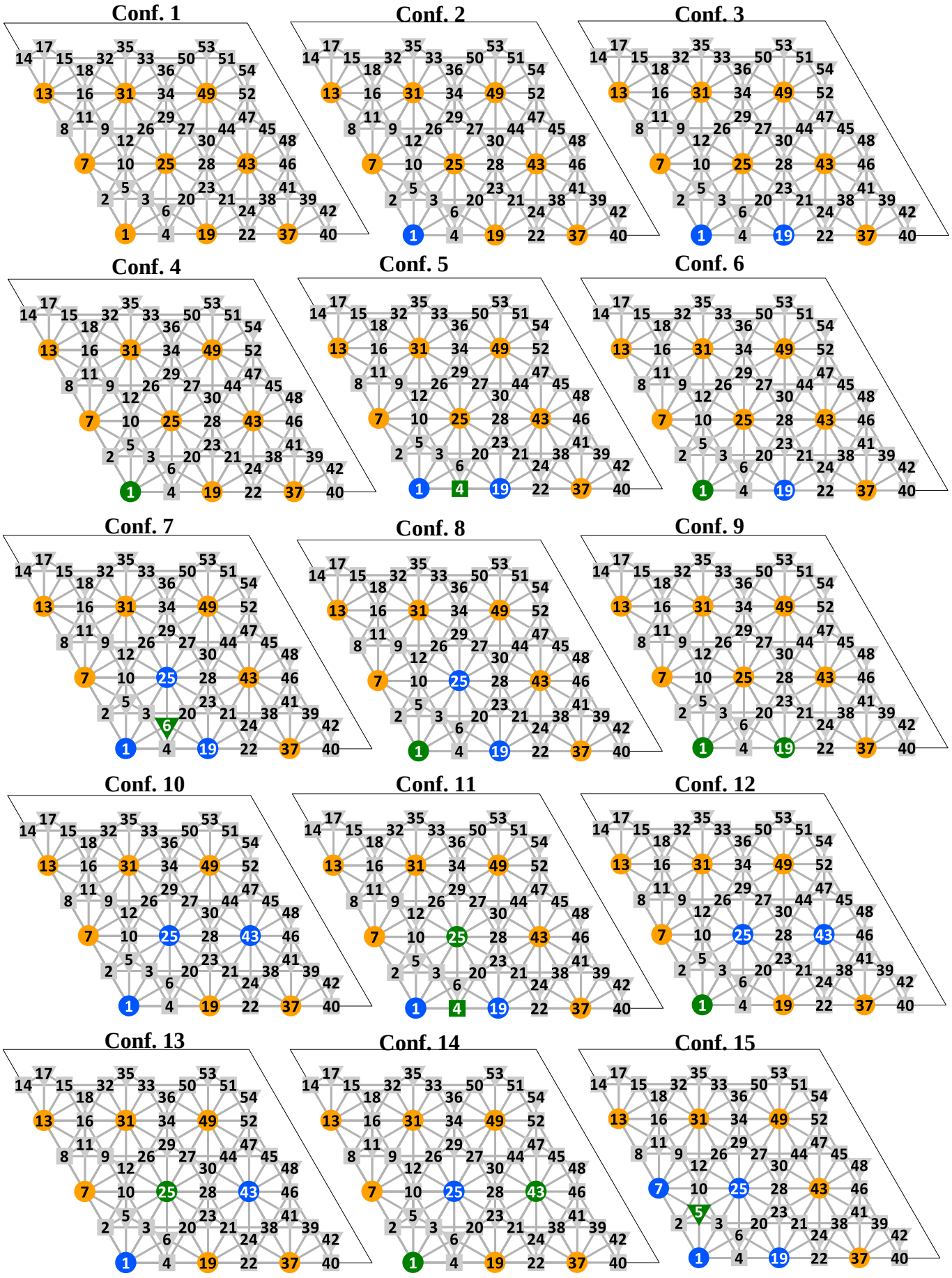

Continues

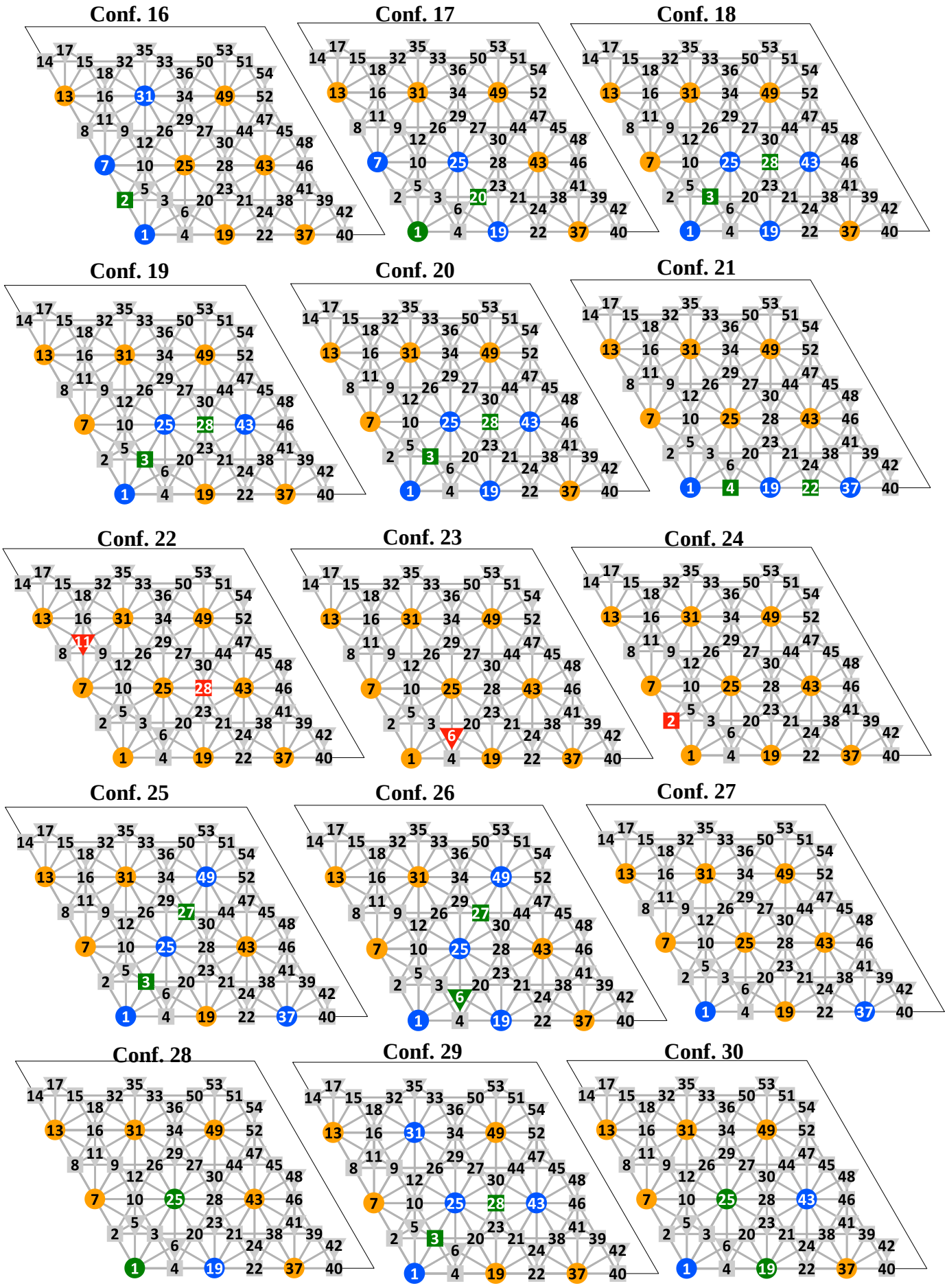
Conf. 16
Conf. 17
Conf. 18
Conf. 19
Conf. 20
Conf. 21
Conf. 22
Conf. 23
Conf. 24
Conf. 25
Conf. 26
Conf. 27
Conf. 28
Conf. 29
Conf. 30

Continues

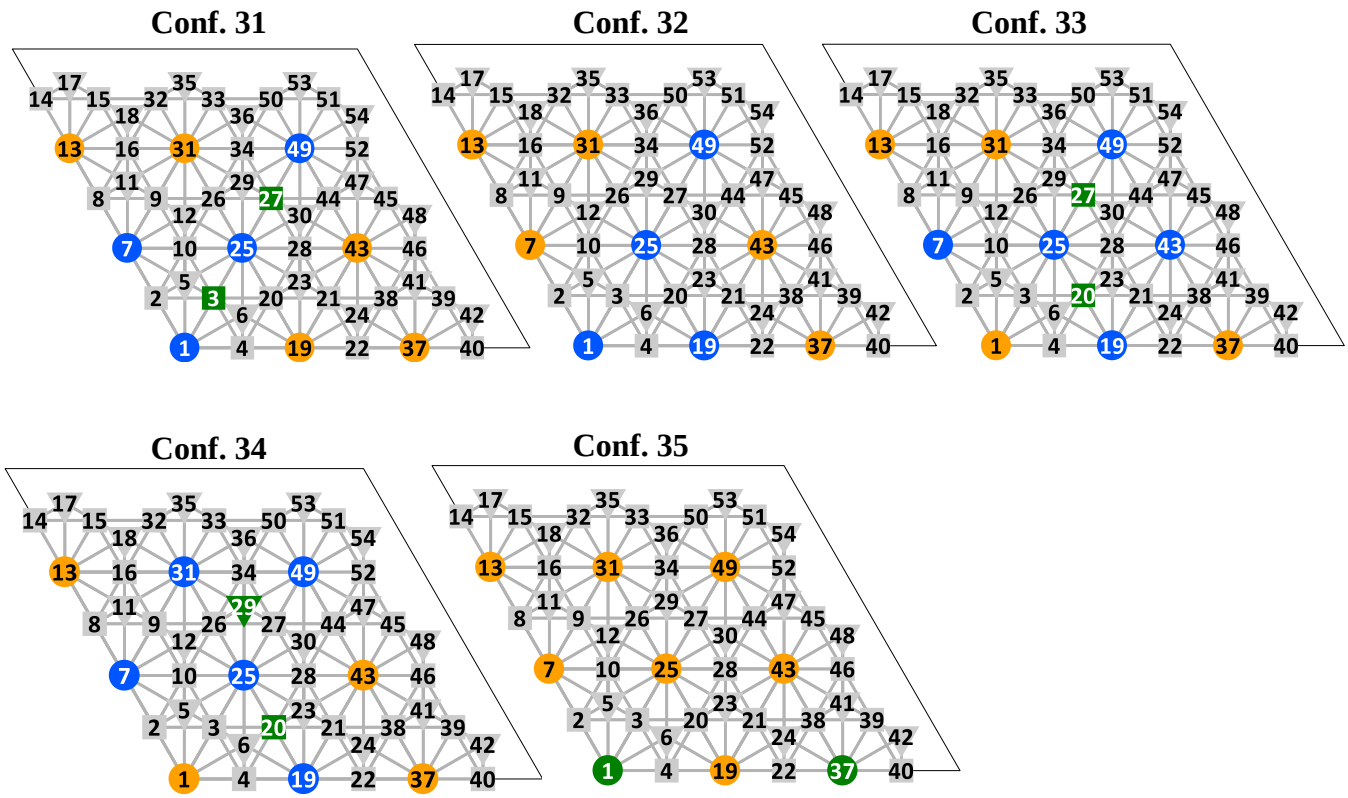

Figure S6. DFT geometries used in the cluster expansion of the Pt/Cu(111) system.

- **Pd/Au(111)**

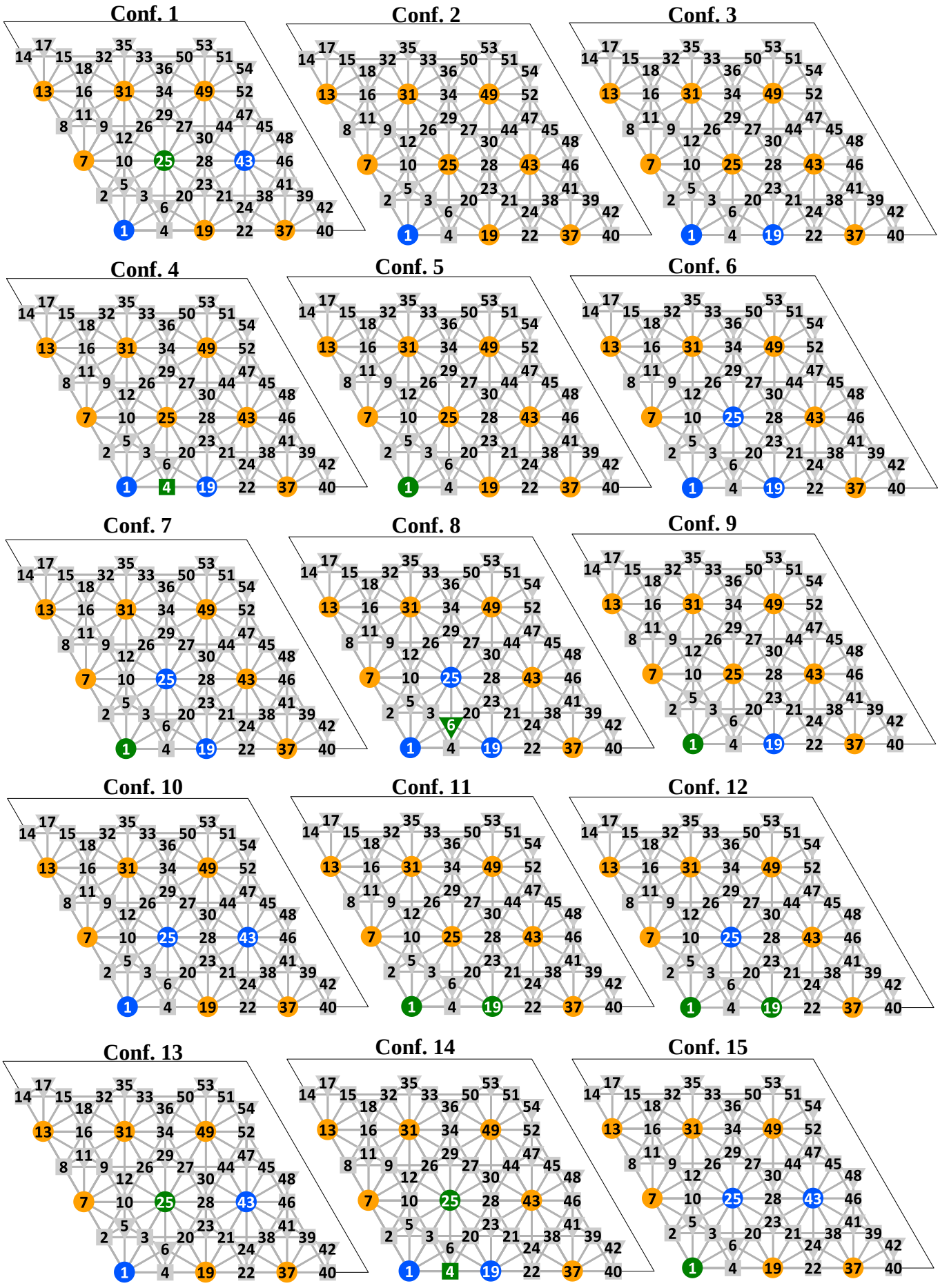

Continues

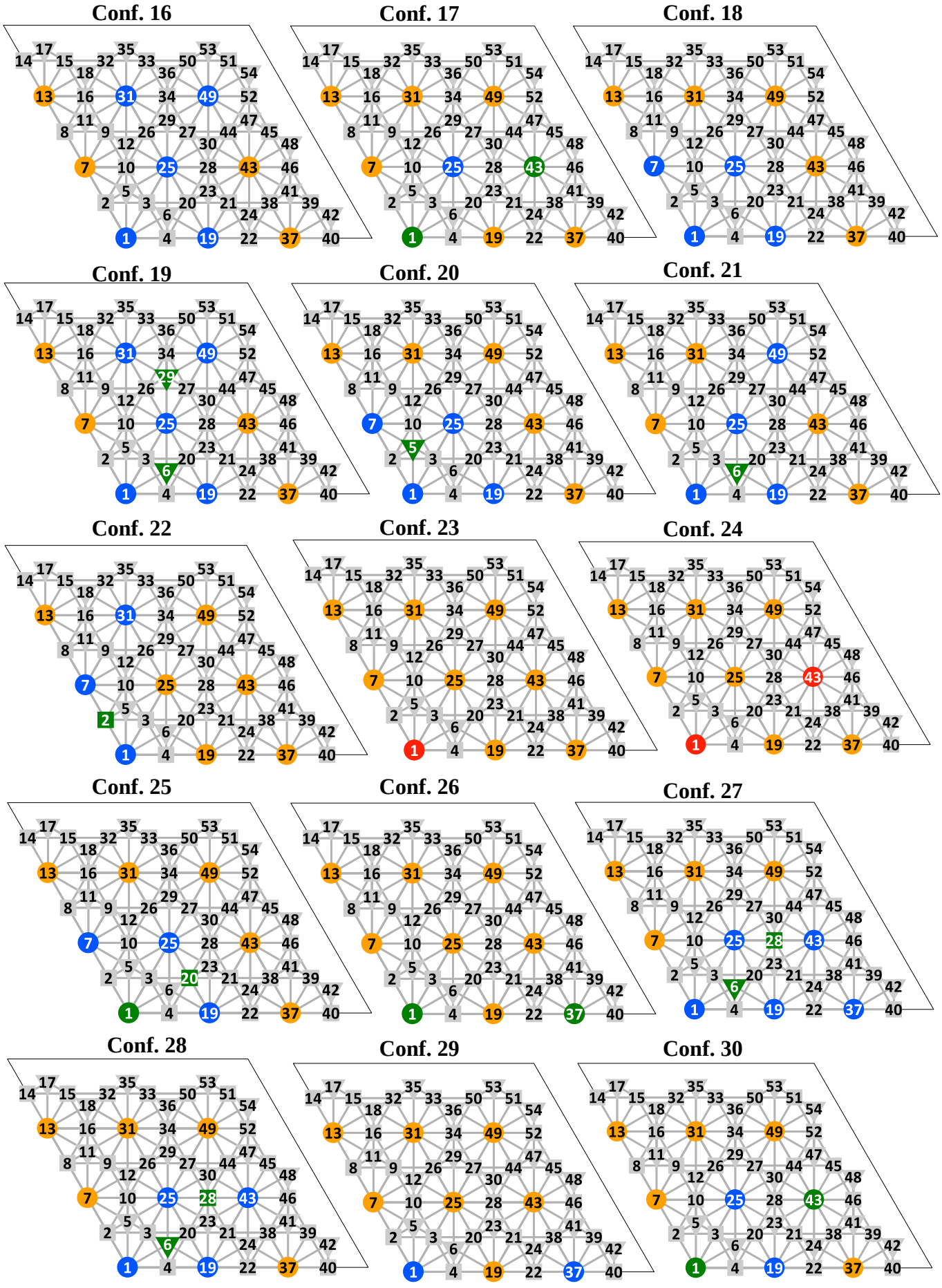
Conf. 16
Conf. 17
Conf. 18
Conf. 19
Conf. 20
Conf. 21
Conf. 22
Conf. 23
Conf. 24
Conf. 25
Conf. 26
Conf. 27
Conf. 28
Conf. 29
Conf. 30

Continues

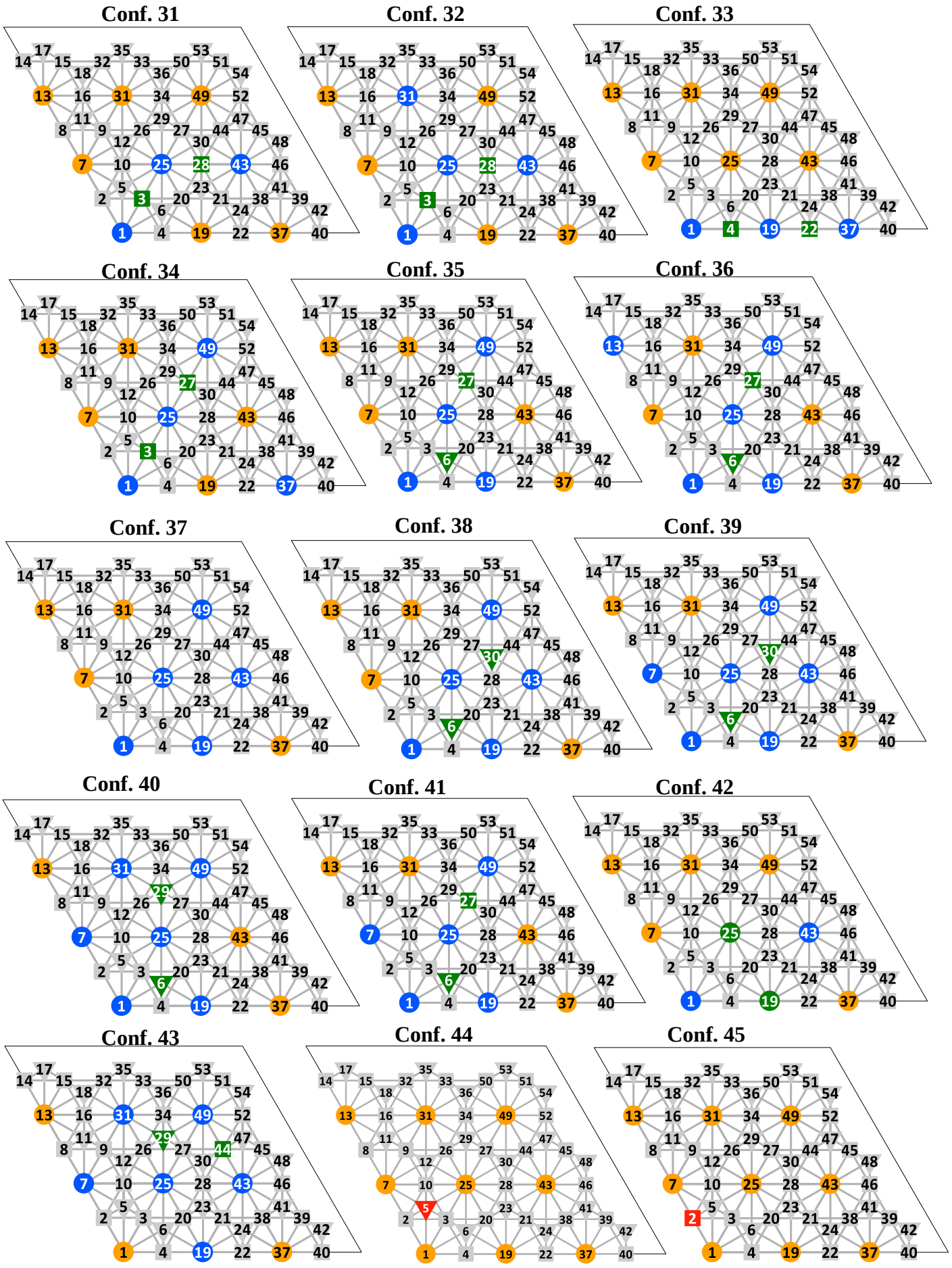
Conf. 31
Conf. 32
Conf. 33
Conf. 34
Conf. 35
Conf. 36
Conf. 37
Conf. 38
Conf. 39
Conf. 40
Conf. 41
Conf. 42
Conf. 43
Conf. 44
Conf. 45

Continues

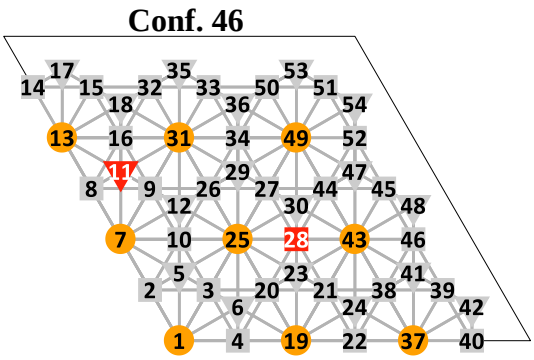

Figure S7. DFT geometries used in the cluster expansion of the Pd/Au(111) system.

- **Pd/Ag(111)**

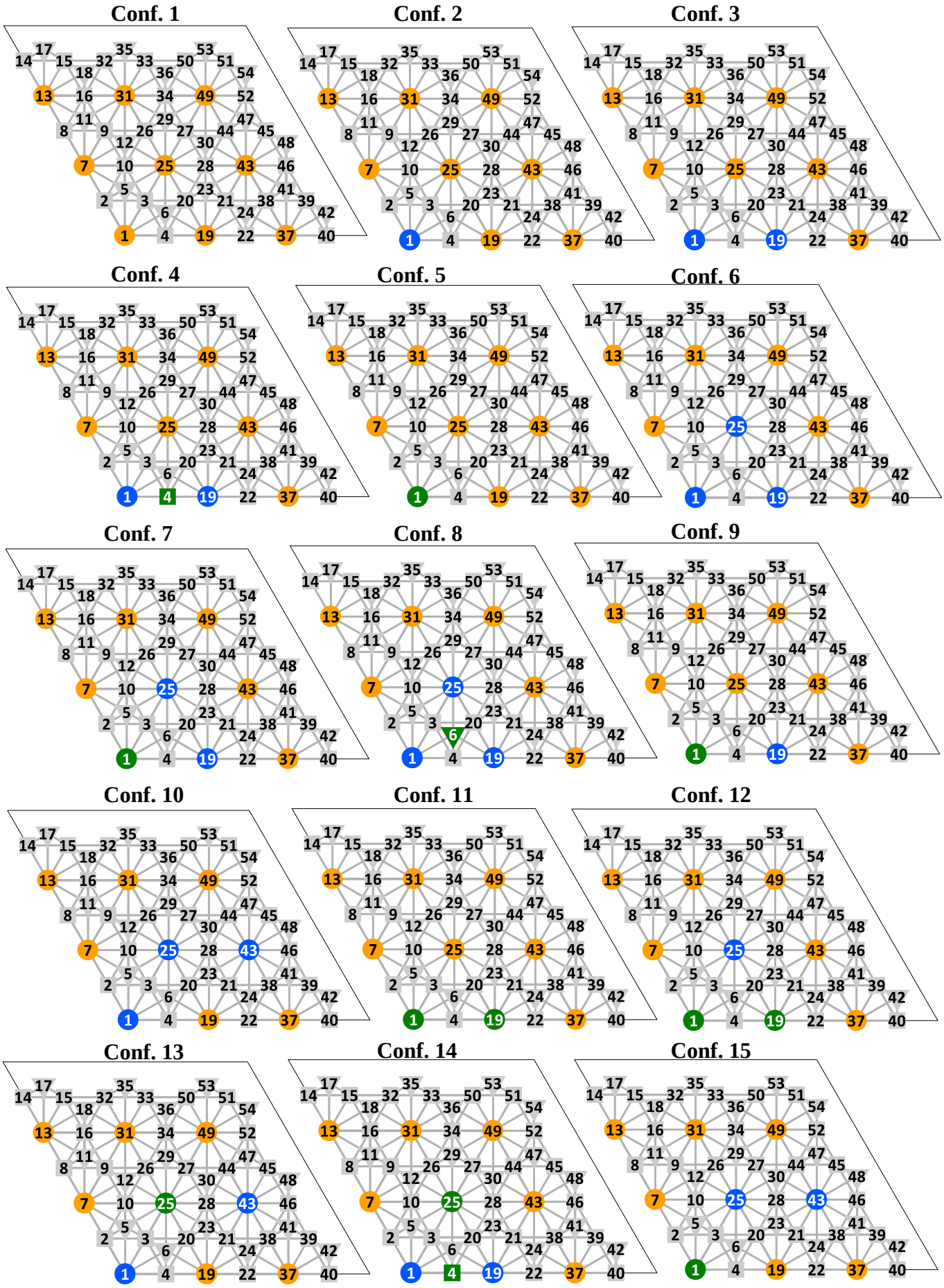

Continues

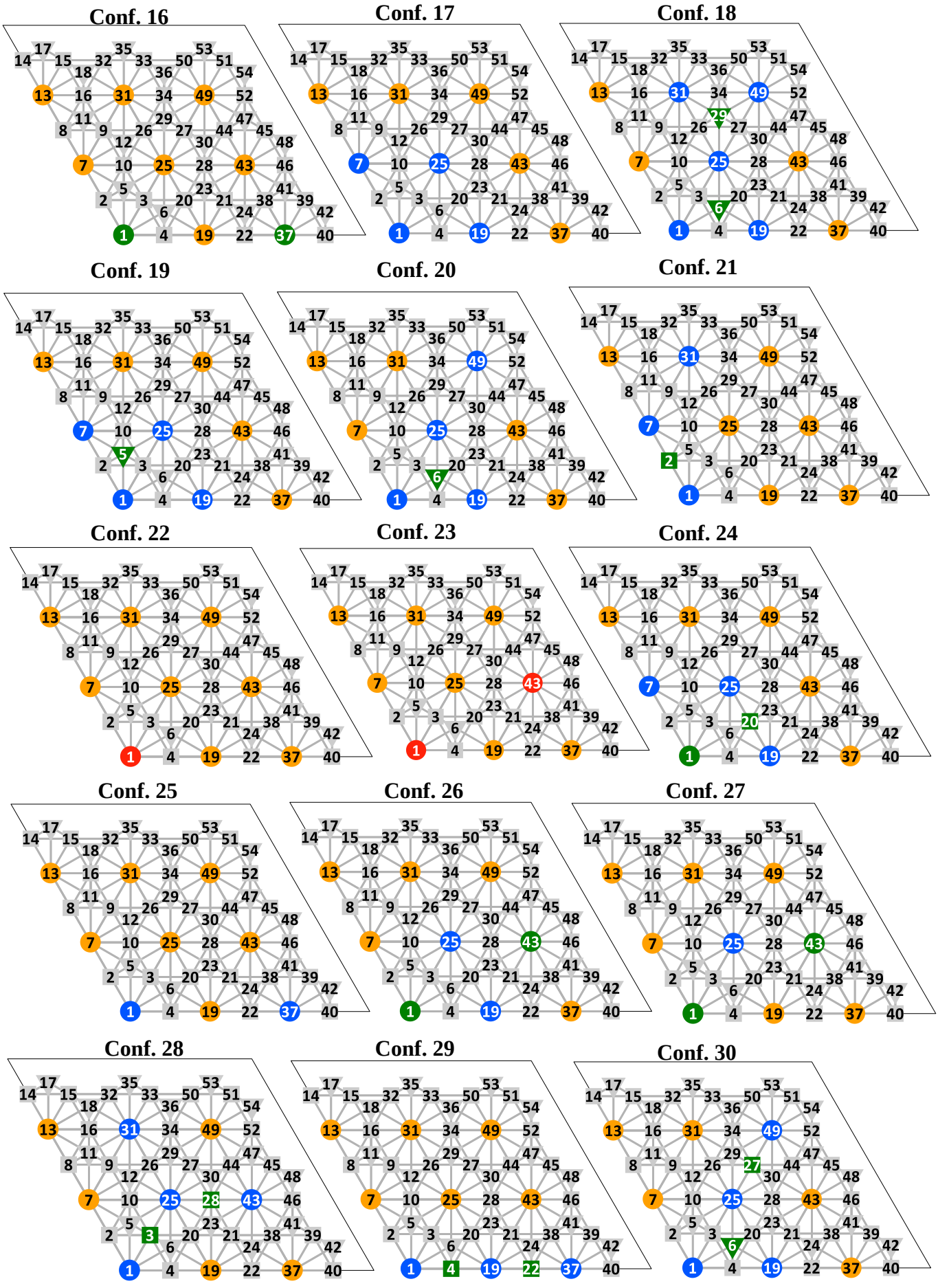
Conf. 16
Conf. 17
Conf. 18
Conf. 19
Conf. 20
Conf. 21
Conf. 22
Conf. 23
Conf. 24
Conf. 25
Conf. 26
Conf. 27
Conf. 28
Conf. 29
Conf. 30

Continues

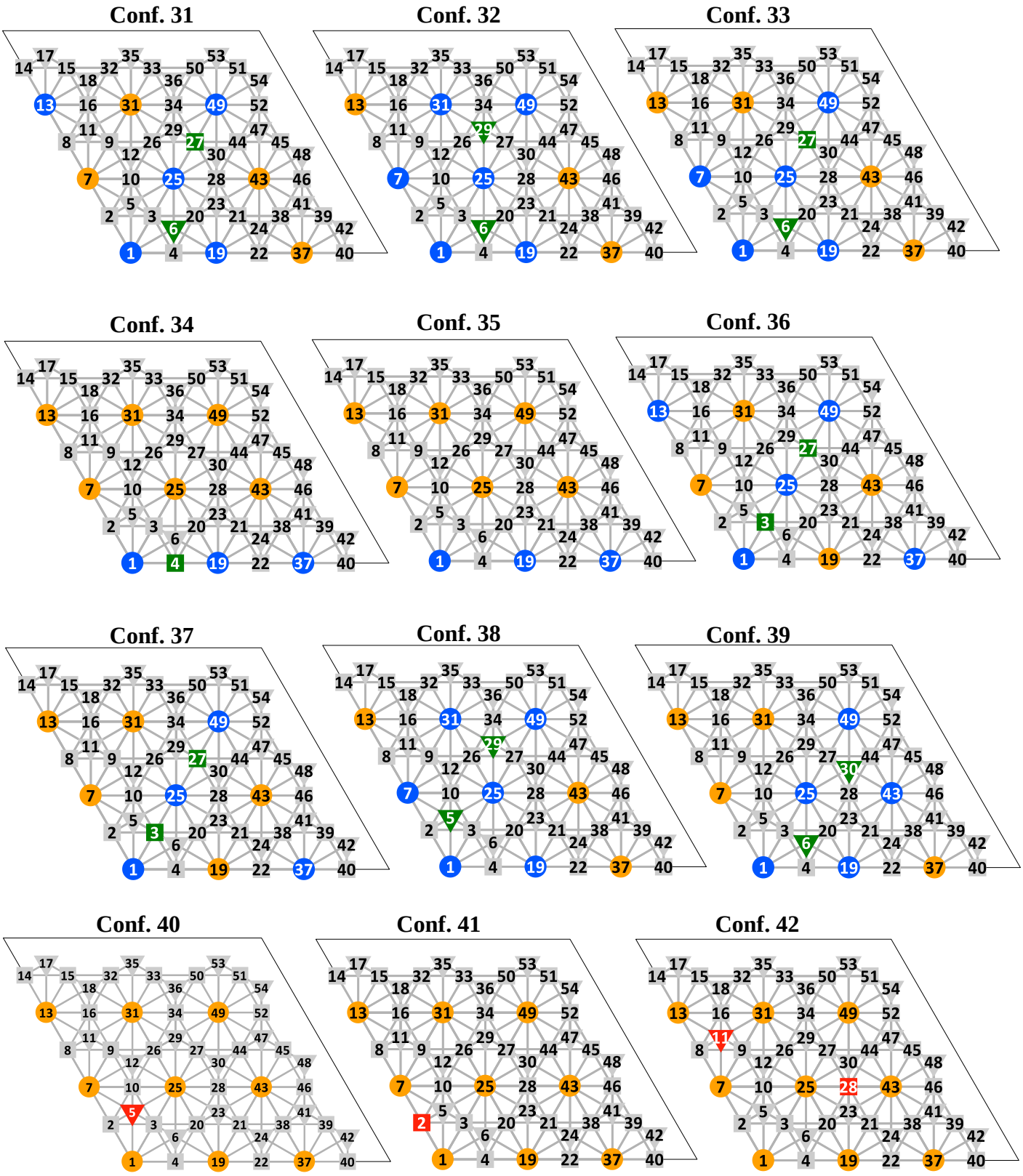

Figure S8. DFT geometries used in the cluster expansion of the Pd/Ag(111) system.

- **Ir/Ag(111)**

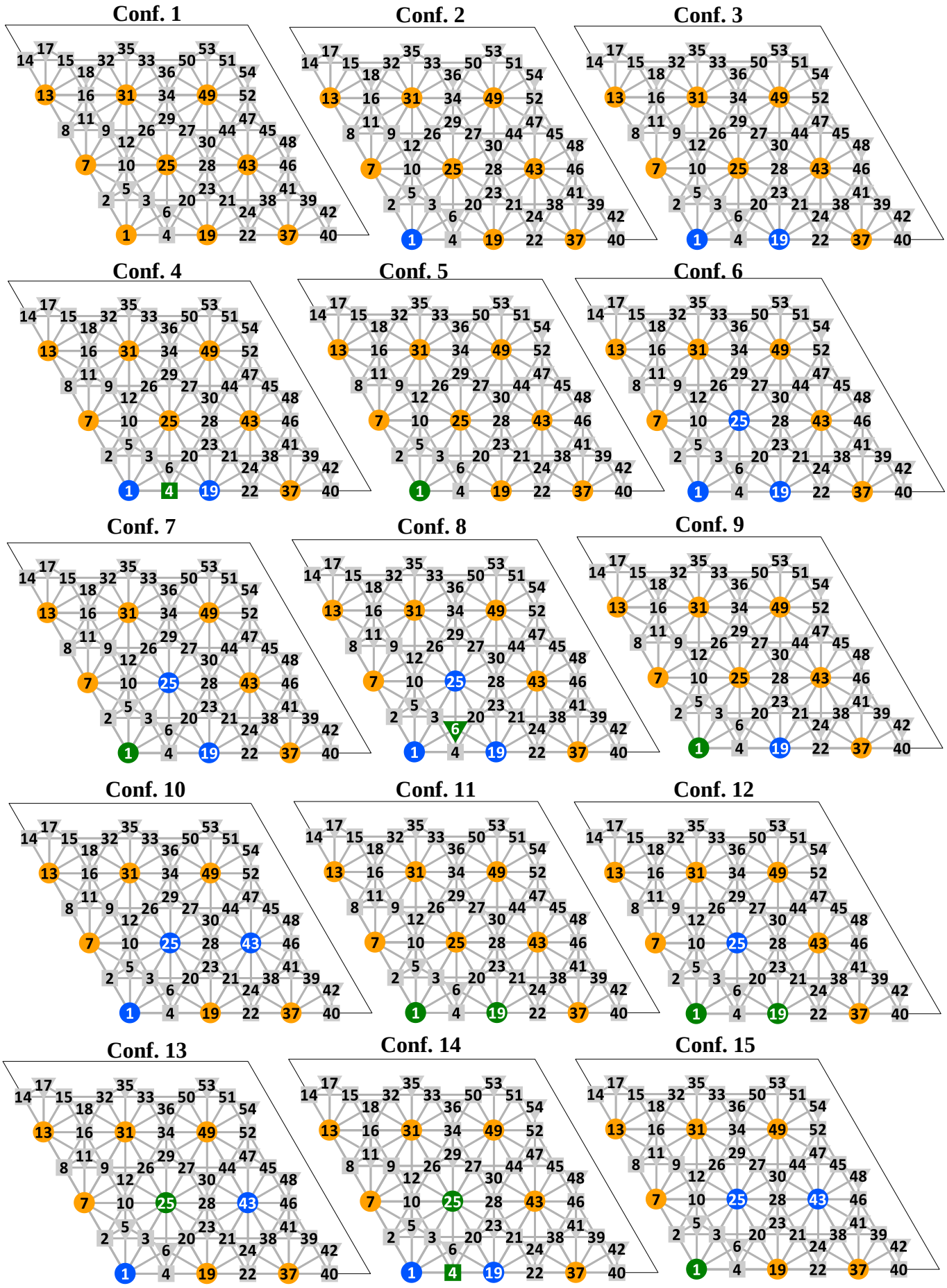

Continues

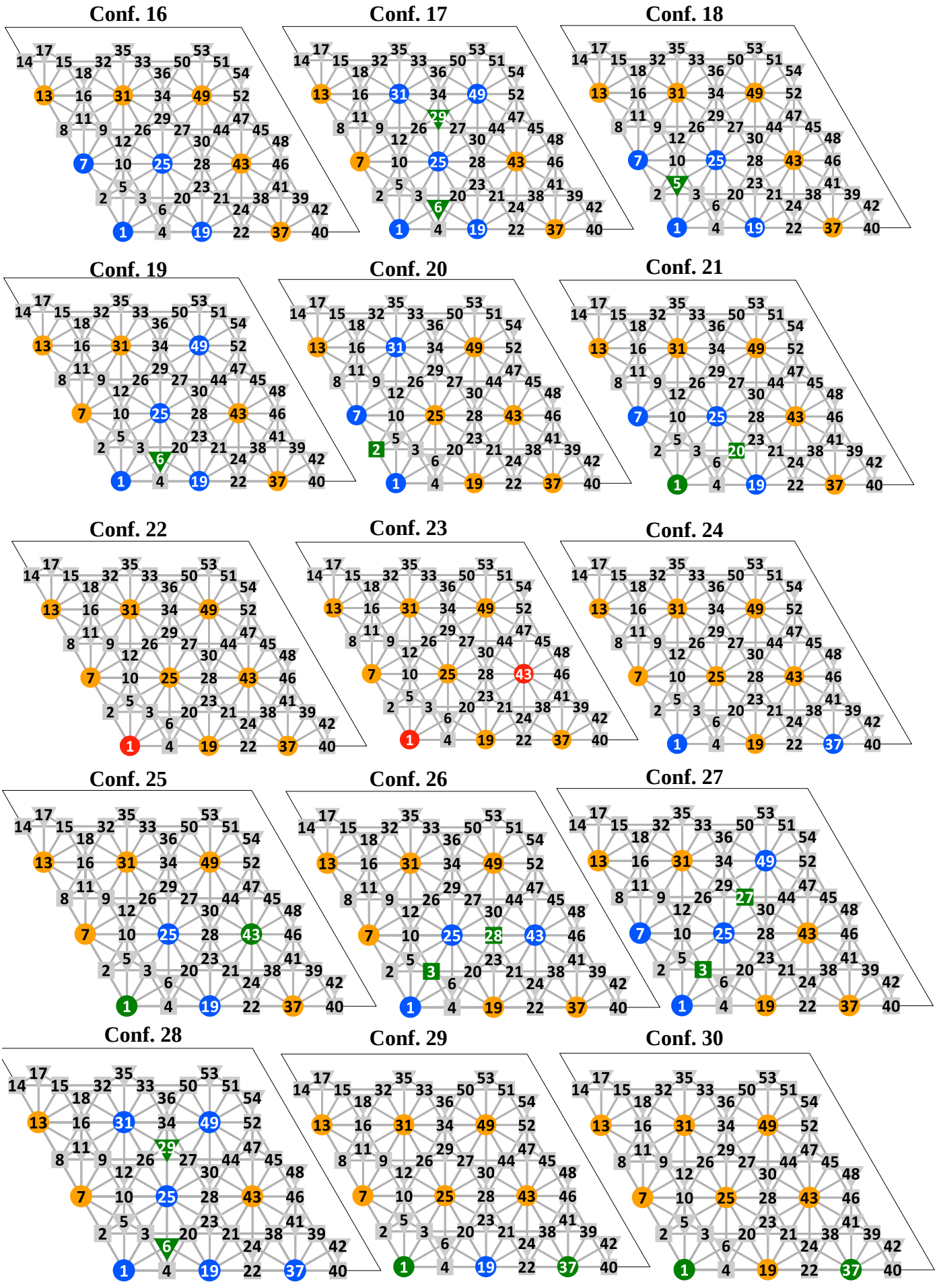
Conf. 16
Conf. 17
Conf. 18
Conf. 19
Conf. 20
Conf. 21
Conf. 22
Conf. 23
Conf. 24
Conf. 25
Conf. 26
Conf. 27
Conf. 28
Conf. 29
Conf. 30

Continues

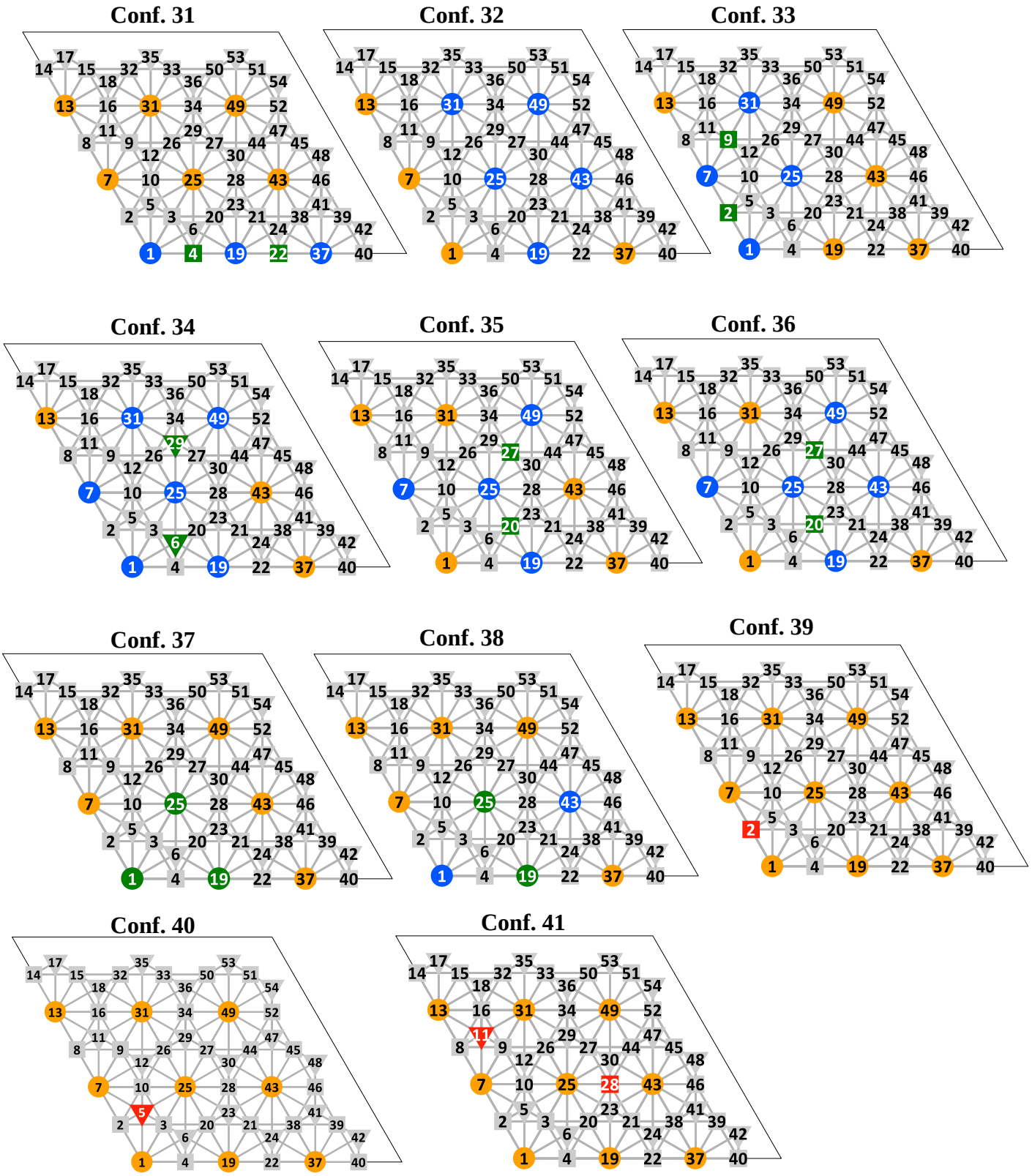

Figure S9. DFT geometries used in the cluster expansion of the Ir/Ag(111) system.

IV. Cook's distances

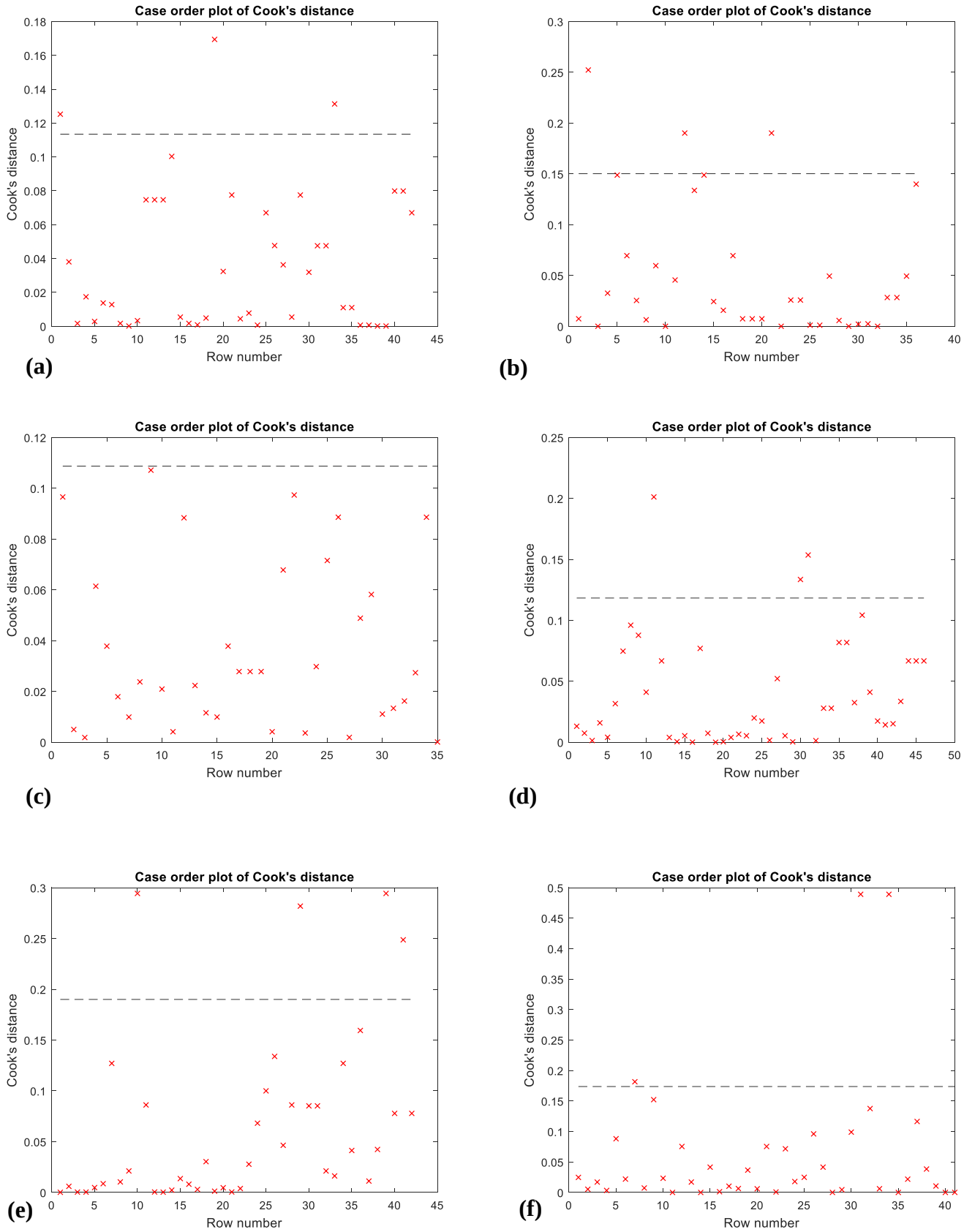

Figure S10. Cook's distances for (a) Ni/Cu(111); (b) Rh/Cu(111); (c) Pt/Cu(111); (d) Pd/Au(111); (e) Pd/Ag(111); and (f) Ir/Ag(111).

V. Average properties in MC simulation

We frequently sample the system during MC simulation, and for each snapshot taken, we calculate the fractions of surface species (i.e. single dopant atoms, dopant dimers, dopant trimers and islands) and the CO dopant fractional coverage. In the main text, we report mean values, calculated over a time-window after stationary conditions have been reached (Figure S11).

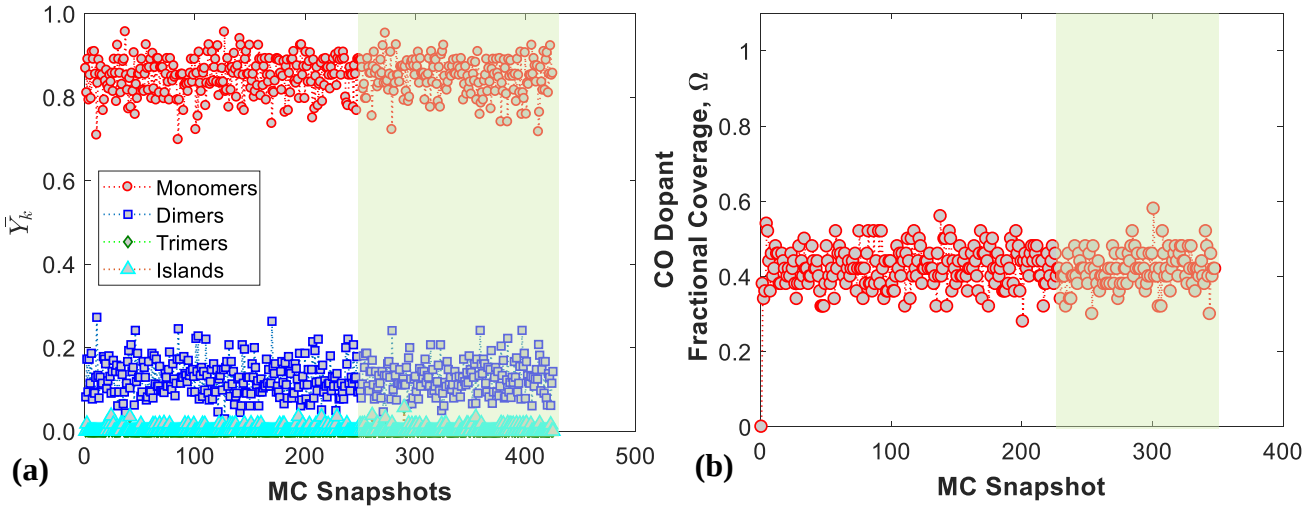

Figure S11. Representative plot of (a) the average fraction of species and (b) the CO dopant fractional coverage versus MC lattice snapshot. The mean reported values are calculated within the regions shaded in green, where stationary conditions are reached.

VI. Calculating the pre-exponential ratio of CO diffusion – Thermodynamic consistency

The total difference in free energy of a multistep thermodynamic process where the initial and final states are identical is

$$\Delta F_{tot} = \Delta F_{12} + \Delta F_{23} + ... + \Delta F_{n1} = 0, \tag{S1}$$

where F is a free energy and ΔF_{12}, ΔF_{23} and ΔF_{n1} are the differences of free energies between states 1 and 2, states 2 and 3 and states n and 1, respectively. An example of such a multistep process is shown in Figure S12: a gas-phase CO molecule binds to the bridge site of a dopant dimer (reaction 1→2); this is followed by a CO* diffusion to an atop site (reaction 2→3) and subsequently by a desorption (reaction 3→1) that brings the system to its initial state 1. The equilibrium constant for the 1→2 step will be

$$K_{12} = \frac{A_{1\to 2}}{A_{2\to 1}} \cdot \frac{\exp\left(-\frac{E_{1\to 2}}{k_B T}\right)}{\exp\left(-\frac{E_{2\to 1}}{k_B T}\right)} = \frac{A_{1\to 2}}{A_{2\to 1}} \cdot \exp\left(-\frac{\Delta E_{rxn,1\to 2}}{k_B T}\right), \tag{S2}$$

where $E_{1\to2}$ and $E_{2\to1}$ are the activation barriers of the 1→2 and 2→1 reactions, respectively, T is the temperature, $A_{1\to2}$ and $A_{2\to1}$ are the pre-exponent factors of the 1→2 and 2→1 reactions, respectively, k_B is Boltzmann's constant, and $\Delta E_{rxn,1\to2}$ is the energy difference between the initial and final states.

The right-hand-side of equation (S2) is

$$\frac{A_{1\to2}}{A_{2\to1}}\cdot\exp\left(-\frac{\Delta E_{rxn,1\to2}}{k_BT}\right)=\frac{Q_{prod}}{Q_{reac}}\cdot\exp\left(-\frac{\Delta E_{rxn,1\to2}}{k_BT}\right)=\exp\left(-\frac{\Delta F_{12}}{k_BT}\right), \tag{S3}$$

where Q_{prod} and Q_{reac} are the partition functions of the initial and final state. From equation (S3)

$$\ln\left(\frac{A_{1\to2}}{A_{2\to1}}\right)-\frac{\Delta E_{rxn,1\to2}}{k_BT}=-\frac{\Delta F_{12}}{k_BT}\quad\Rightarrow$$
$$\Rightarrow\Delta F_{12}=\Delta E_{rxn,1\to2}-k_BT\cdot\ln\left(\frac{A_{1\to2}}{A_{2\to1}}\right). \tag{S4}$$

Similarly, we write

$$\Delta F_{23}=\Delta E_{rxn,2\to3}-k_BT\cdot\ln\left(\frac{A_{2\to3}}{A_{3\to2}}\right), \tag{S5}$$

$$\Delta F_{31}=\Delta E_{rxn,3\to1}-k_BT\cdot\ln\left(\frac{A_{3\to1}}{A_{1\to3}}\right). \tag{S6}$$

By replacing equations (S6), (S5) and (S4) into equation (S1) we find

$$\Delta F_{tot}=\Delta E_{rxn,tot}-k_B\cdot T\left(\ln\left(\frac{A_{3\to1}}{A_{1\to3}}\right)+\ln\left(\frac{A_{2\to3}}{A_{3\to2}}\right)+\ln\left(\frac{A_{1\to2}}{A_{2\to1}}\right)\right)=0\cdot \tag{S7}$$

Since the final and initial states are identical (i.e. a CO molecule in gas phase, Figure S12), $\Delta E_{rxn,tot}$ =0, and therefore

$$\underbrace{\frac{A_{1\to2}}{A_{2\to1}}}_{\substack{Pre-exponential\\ Ratio\,1}}\times\underbrace{\frac{A_{2\to3}}{A_{3\to2}}}_{\substack{Pre-exponential\\ Ratio\,2}}\times\underbrace{\frac{A_{3\to1}}{A_{1\to3}}}_{\substack{Pre-exponential\\ Ratio\,3}}=1. \tag{S8}$$

The pre-exponential ratios 1 and 3 in equation (S8) involve the pre-exponential factors of the CO adsorption and desorption from and to an atop site and a bridge site; these ratios are obtained from first principles (see main text). Once the aforementioned pre-exponential ratios are computed, we calculate the diffusion pre-exponential ratio (pre-exponential ratio 2) by means of equation (S8). In this way, we assure the thermodynamic consistency of our MC calculations. In particular, using eq. (S8) we calculate the pre-exponential ratios for all the CO diffusion processes that may happen during our MC simulations. This includes: CO diffusion from a dopant top site to a bridge site surrounded by dopant atoms, CO diffusion from dopant top site to a threefold site surrounded by dopant atoms, CO diffusion from a bridge sites surrounded by dopant atoms to a threefold site also surrounded by dopant atoms and all CO diffusion processes that can take place on host metal sites (see Figure 2 in the main text).

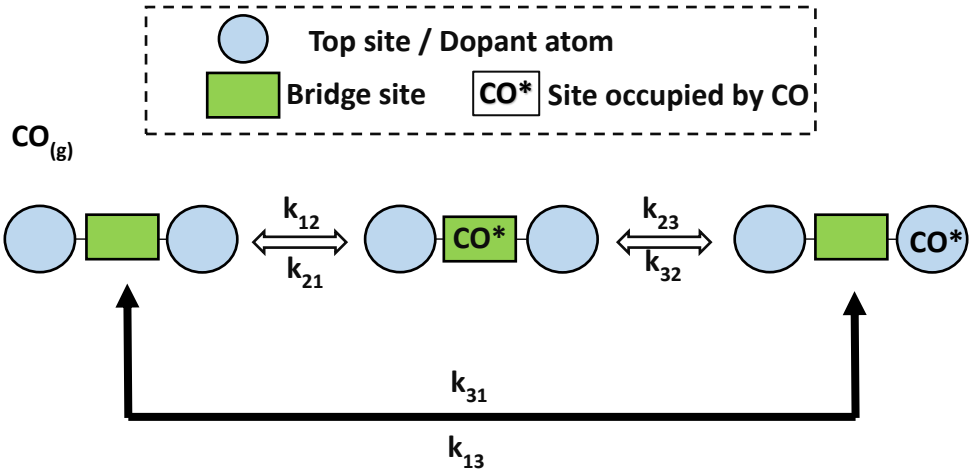

Figure S12. A typical example of multistep process with the same initial and final states.

VII. Vibrational frequencies and maximum CO partial pressures

The vibrational frequencies for CO chemisorption on the most stable site on pure host metal (i.e. Au(111), Ag(111) and Cu(111) and single atom alloy (SAA) surfaces are reported in Ref. 3. In Table S2, we report the corresponding vibrational frequencies on bridge and threefold sites surrounded by dopant atoms for all the highly dilute alloy surfaces under investigation:

Table S2. Vibrational frequencies (ν) for CO chemisorption on hollow sites surrounded by dopant atoms.

Surface	Site	ν_1 (cm^{-1})	ν_2 (cm^{-1})	ν_3 (cm^{-1})	ν_4 (cm^{-1})	ν_5 (cm^{-1})	ν_6 (cm^{-1})
Ni/Cu(111)	bridge	1800	345	315	295	154	34
	fcc	1732	332	294	294	142	137
Rh/Cu(111)	bridge	1801	357	341	341	165	41
	fcc	1728	340	312	311	144	143
Pt/Cu(111)	bridge	1835	356	353	340	175	50
	fcc	1761	334	309	309	137	135
Pd/Au(111)	bridge	1859	350	300	294	152	49
	fcc	1755	329	328	275	144	144
Pd/Ag(111)	bridge	1840	347	300	294	154	51
	fcc	1736	333	333	279	142	142
Ir/Ag(111)	bridge	1704	412	395	390	191	65
	fcc	1633	367	319	319	162	162

The quantity $P_{CO,max}$ is defined in the main text (see eq. 10) and corresponds to the CO partial pressure that results in CO dopant fractional coverage approximately equal to unity. In Table S3 we summarise the $P_{CO,max}$ values for each alloy surface studied herein.

Table S3. Summary of $P_{CO,max}$ values.

Surface	$P_{CO,max}$ (atm)
Ni/Cu(111)	10^{-7}
Pd/Ag(111)	10^{-3}
Pd/Au(111)	10^{-1}
Pt/Cu(111)	10^{-5}
Rh/Cu(111)	10^{-13}
Ir/Ag(111)	10^{-20}

VIII. Calculation of partition functions for CO adsorption/desorption

For a linear rotating gas-phase molecule the rotation is a 2D rotation and $Q_{rot,CO(g)}$ is[4]

$$Q_{rot,\mathrm{CO}_{(g)}} = \frac{8 \cdot \pi^2 \cdot I \cdot k_B \cdot T}{\sigma \cdot h^2}, \tag{S9}$$

where σ is the symmetry number and is equal to unity for CO, and I is a moment of inertia. The partition function for translation is computed by assuming a 2D translation as[4]

$$Q_{transl,\mathrm{CO}_{(g)}} = A_{st} \cdot \frac{2 \cdot \pi \cdot m_{\mathrm{CO}} \cdot k_B \cdot T}{h^2}. \tag{S10}$$

To find the vibrational partition function, we compute the vibrational frequencies of CO on the various adsorption sites (see the previous section) and

$$Q_{vib,CO*} = \prod_{j=1}^{m} \frac{e^{-\frac{\hbar\omega_j}{2k_bT}}}{1-e^{-\frac{\hbar\omega_j}{k_bT}}}, \tag{S11}$$

where m is the number of vibrational modes and ω_j is the oscillation frequency of the j^{th} normal mode of vibration. We note that for a CO molecule in the gas phase there is only one mode of vibration, which is the stretching of the CO bond, and therefore $Q_{vib,CO(g)}$ is computed using eq. (S11) with m = 1.

IX. Representative images of the DFT slab and Monte Carlo snapshots

Figure S13 shows the top and side views of the (111) slab used for our DFT calculations. Figure S14 shows representative MC snapshots from simulations on Ir/Ag, Pd/Ag and Pt/Cu surfaces. Each of these alloys follows a different pattern of behaviour (see the main text), thereby representing an alloy category.

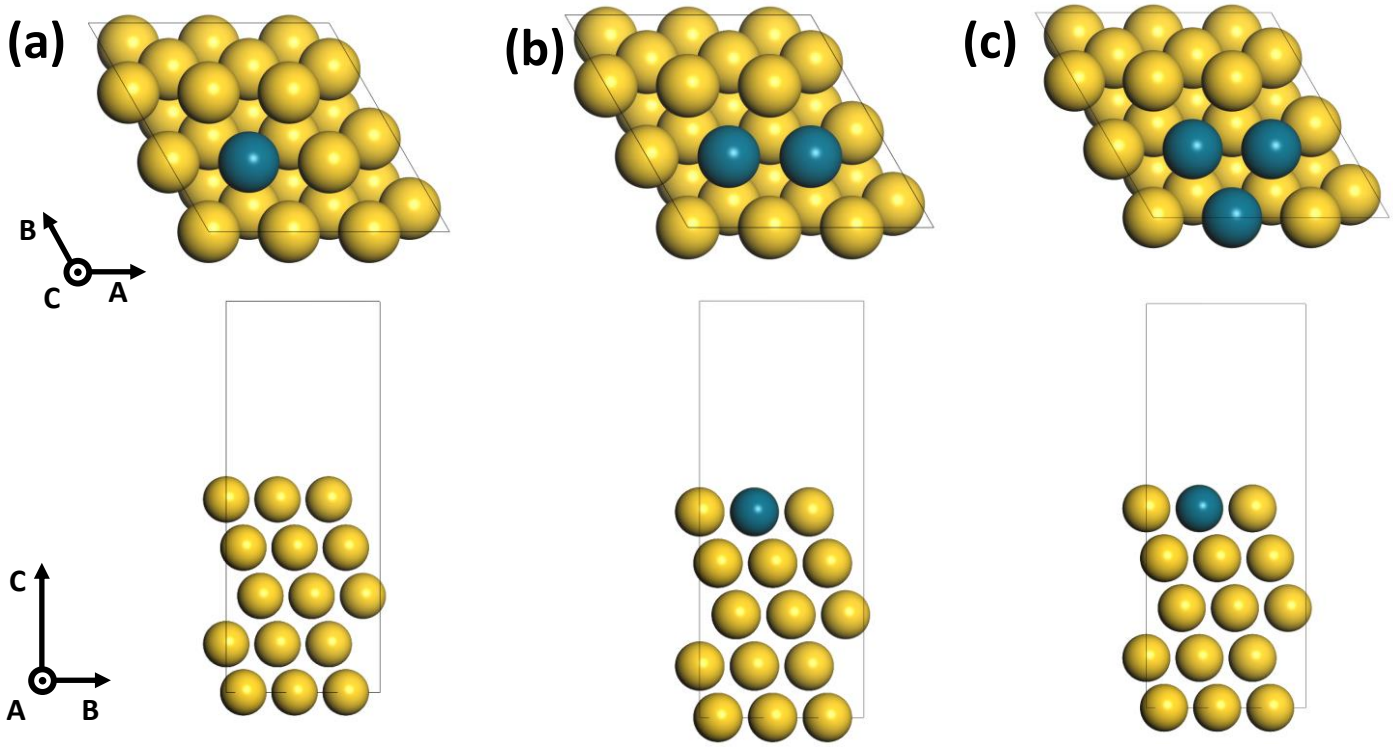

Figure S13. Figures in the first row show the top view of the (111) DFT slab with (a) a single dopant atom (b) a dopant dimer and (c) a dopant triangular trimer located on the surface layer. Figures in the second row show the side view of the same slabs. Host metal atoms are shown in yellow and dopant atoms are shown in teal in all cases. The symbol ⊙ indicates an arrow with direction from the page towards the reader.

(a)

Low CO Coverage - $\Omega_{CO} = 0.0$

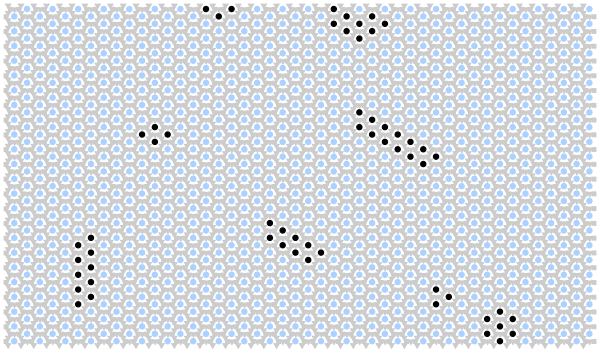

Intermediate CO Coverage - $\Omega_{CO} = 0.66$

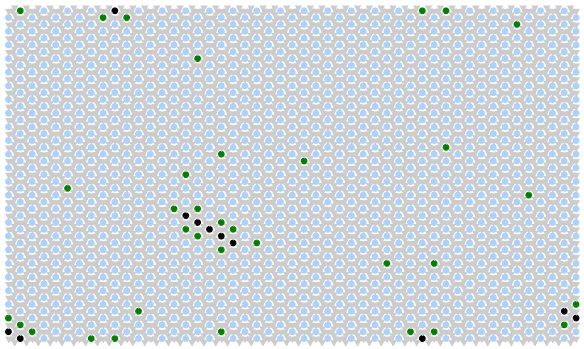

High CO Coverage - $\Omega_{CO} = 0.96$

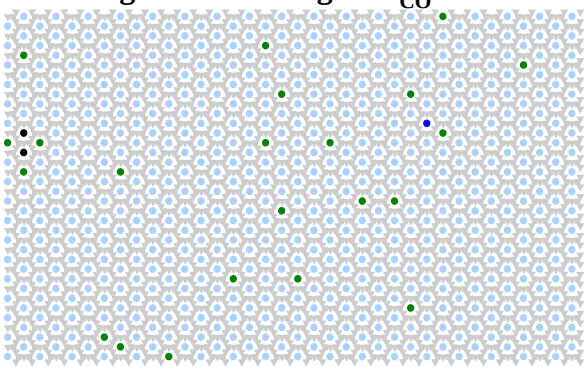

(b)

Low CO Coverage - $\Omega_{CO} = 0.0$

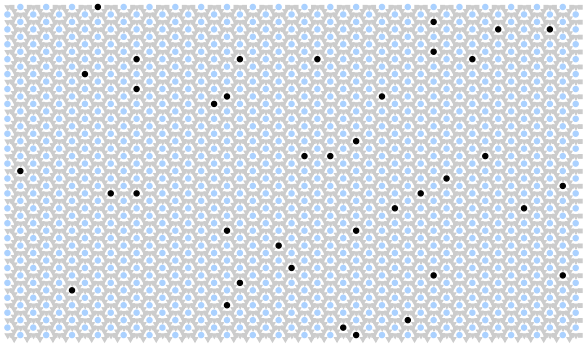

Intermediate CO Coverage - $\Omega_{CO} = 0.26$

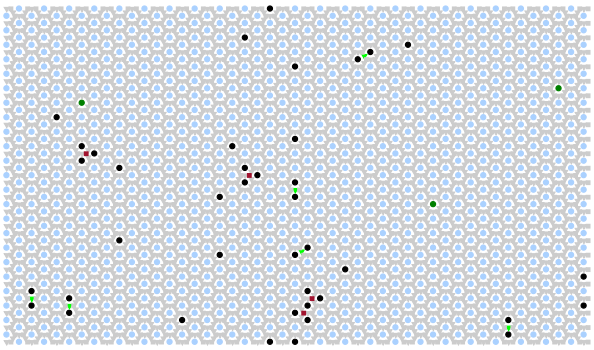

High CO Coverage - $\Omega_{CO} = 0.98$

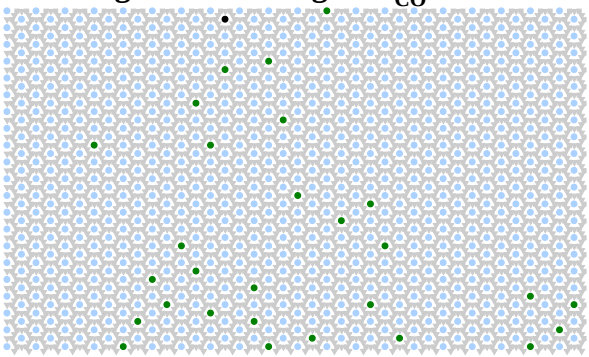

Continues

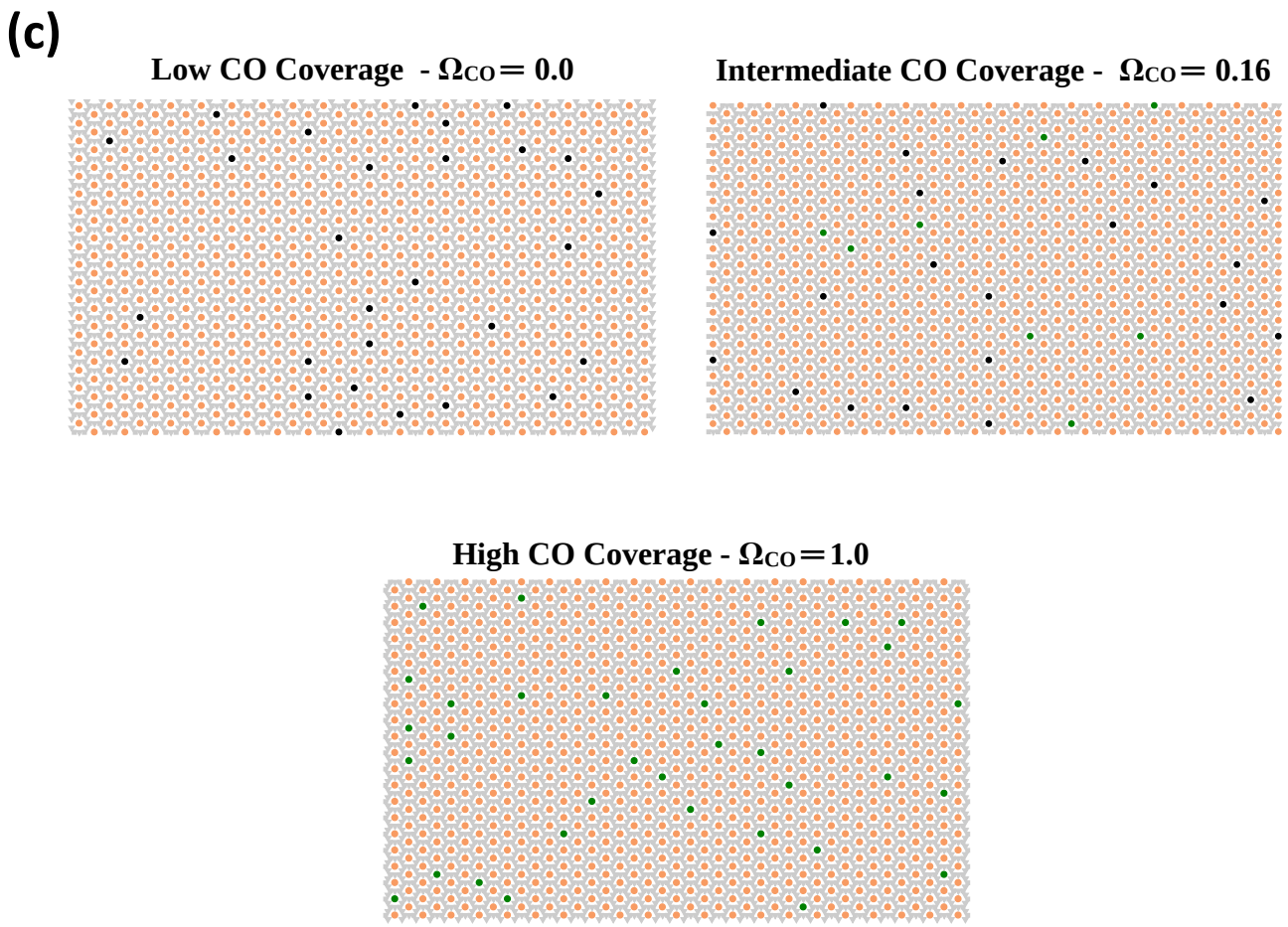

Figure S14. Representative MC snapshots for (a) Ir/Ag(111) (b) Pd/Ag(111) and (c) Pt/Cu(111). In each panel there are three MC snapshots corresponding to low, intermediate and high CO coverage. The corresponding CO dopant fractional coverage (Ω_{CO}) for the MC snapshots displayed, is shown above each inset. Ag, Cu and dopant atoms (i.e. Pd, Ir and Pt) are shown in light blue, orange and black, respectively. CO adsorbed on a dopant top site, a host site, a threefold site surrounded by dopant atoms and a twofold site surrounded by dopant atoms are shown in green, blue, magenta and light green, respectively. CO free twofold and threefold sites are shown in grey. We note that all panels show only a representative part of the MC lattice.

X. An electronic perspective of surface aggregation

In this section, we discuss the surface aggregation of dopant atoms on highly dilute alloys from an electronic standpoint. We focus on the surface aggregation of Pd atoms on Pd/Ag(111) and Pd/Au(111) surfaces. On the aforementioned surfaces, there is a considerable surface aggregation of Pd under reactive conditions as shown in the main text.

Using LOBSTER version 3.2.0,[5–7] we calculated the *d*-projected density of states (DOS) of the surface Pd atoms on the SAA, dimer and trimer geometries and the result is shown in Figure S15 (a), (b) and (c), respectively. For both Pd/Ag(111) and Pd/Au(111) SAA surfaces, we observe that the electronic states are concentrated in a small range of energies close to the Fermi level (Figure S15 (a)). This observation is in line with previous *d*-projected DOS studies on SAA surfaces.[8] Conversely, the *d*-projected DOS of the Pd atoms on the dimer and trimer geometries show broader characteristics than the SAA geometry (Figure S15 (b) and (c)). In particular, at increasing Pd cluster size, there is a progressively increasing density of occupied states close to the Fermi level. This behaviour may be one of the factors that result in stronger CO binding on the

hollow sites of Pd dimers and trimers as compared to the top site of an isolated Pd atom,[3,9] and therefore one of the factors that renders these alloys susceptible to aggregation (see the main text).

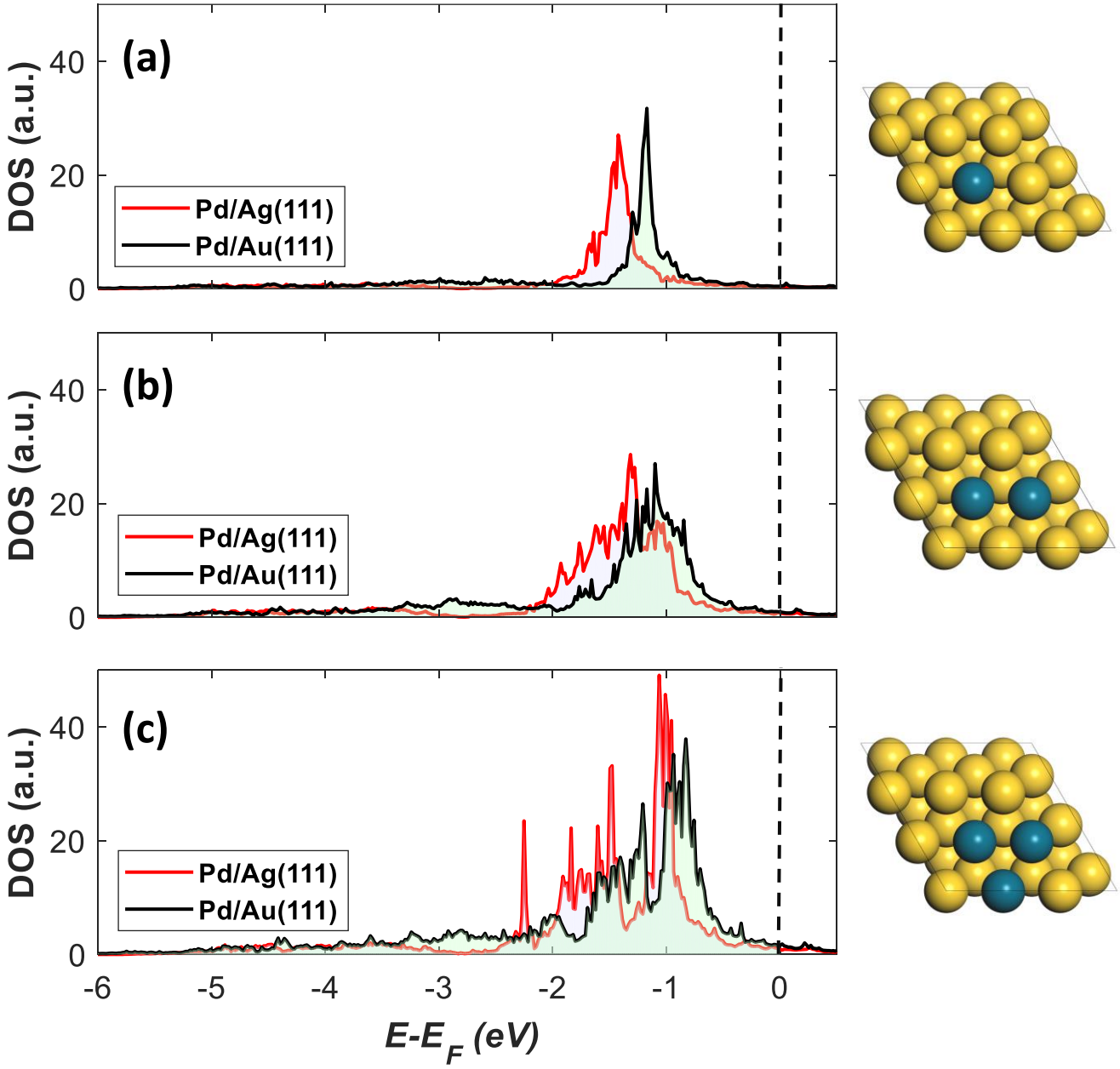

Figure S15. Shows the *d*-DOS plots for: (a) the SAA geometry; (b) the dimer geometry; and (c) the trimer geometry for Pd/Ag(111) and Pd/Au(111) surfaces. All DOS are projected only to Pd atoms on the topmost layer of the slab. The dashed black lines highlight the Fermi level, and the insets next to each panel show the top view of the structure to which the DOS plot on the left corresponds. Pd atoms in the insets are shown in teal and host metal atoms, which can be either Ag or Au, in yellow.

Based on our *d* DOS, we have also computed the *d*-band centre for all the examined structures. In Figure S16, we plot the adsorption energy of CO (E_{ads}(CO)) versus the computed *d*-band centre (ε_d) of the investigated Pd/Ag and Pd/Au geometries. We note that for the same alloy, an upshift of the *d*-band centre to higher energies results in stronger CO binding. This behaviour is attributed to the fact that an upshift in the *d*-band centre implies an energy upshift in the antibonding states, which, as a result, become less filled.[10] This trend clarifies the stronger CO binding on the threefold site of a trimer configuration as compared to the bridge

site of a dimer, as well as the stronger CO binding on the latter site as compared to the top site of an isolated Pd atom. It follows that the surface aggregation of Pd atoms will be favoured in the presence of CO, at coverages such that only the bridge and threefold sites of dimer and trimer geometries are occupied. This is also revealed through our MC simulations (see main text) and previous DFT calculations.[3]

As a final remark, we note that even though the ε_d of the Pd/Au(111) SAA geometry is higher in energy than the corresponding ε_d of the Pd/Ag(111) SAA geometry (Figure S16), the latter structure binds CO more strongly than the former. This deviation of SAA surfaces from the *d*-band model has been previously discussed,[8] and our results suggest that is true for highly dilute alloy surfaces as well (see dimer, trimer structures in Figure S16).

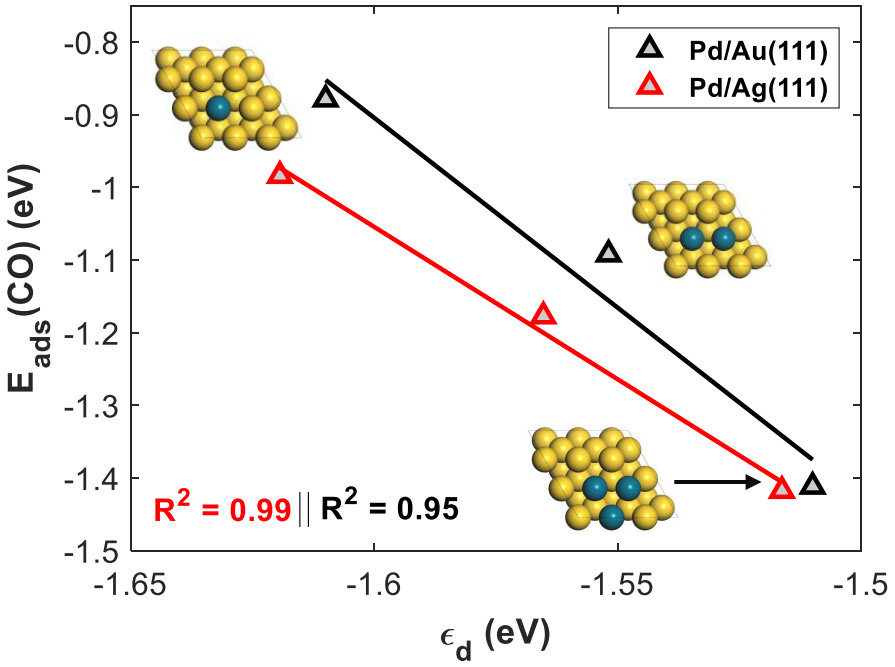

Figure S16. The adsorption energy of CO on Pd/Ag and Pd/Au SAA, dimer and trimer structures versus their *d*-band centre. The insets show the top view of the DFT slab of these structures. Pd atoms in the insets are shown in teal and host metal atoms, which can be either Ag or Au, in yellow.

XI. Calculating the formation energy of a DFT geometry

In the current section, we elaborate on the meaning of the equation which we have employed for the calculation of the formation energy of the DFT geometries in our dataset; this is equation 2 in the main text and we repeat it here:

$$E_f = E_{tot}\left(n+m\cdot CO\right)+\left(n-1\right)\cdot E_{tot}\left(host\right)-n\cdot E_{tot}\left(SAA\right)-m\cdot E_{tot}^{CO_{(g)}}. \quad \text{(S11)}$$

This equation defines the formation energy of any DFT geometry relative to the DFT energy of the SAA structure and the DFT energy of CO in the gas phase. We note that the number of CO gas phase molecules *m* is the number of CO molecules in the structure whose formation energy needs to be computed. From eq. (S11) we note that the "initial state" energy contains contributions from the CO molecules in the gas phase and the SAA geometry. In turn, the "final state" energy contains the DFT energy of the geometry under consideration and the DFT energy of the host material multiplied by *n*-1; *n* is the number of dopant atoms on the DFT

geometry of interest. Thus, eq. (S11) ensures that the number of atoms of each element in the initial and final states does not change.

This concept can be better illustrated through an example, in which we have to calculate the formation energy of the geometry shown in Figure S17 (a). All DFT slabs discussed here contain 45 metal atoms in total. The slab in Figure S17 (a) contains 2 adsorbed CO molecules, 3 dopant atoms and 42 host atoms. For this geometry, $n = 3$ and $m = 2$, and therefore the "initial state" will be composed of 3 SAA geometries and 2 CO molecules in the gas phase (see eq. (S11)), whereas the "final state" will be composed of the structure whose formation energy has to be computed, and 2 (i.e. n-1) pure host metal geometries (Figure S17 (b)). Having computed the DFT energy of all the aforementioned structures, one can readily calculate the formation energy of the geometry in Figure S17 (a) using eq. (S11). Importantly, we realise that indeed the number of atoms of each element in the initial and final states is unchanged (Figure S17 (b)), thereby verifying the validity of E_f obtained from eq. (S11).

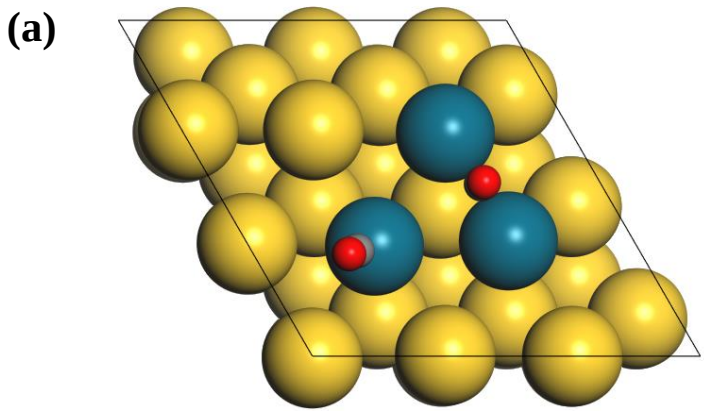

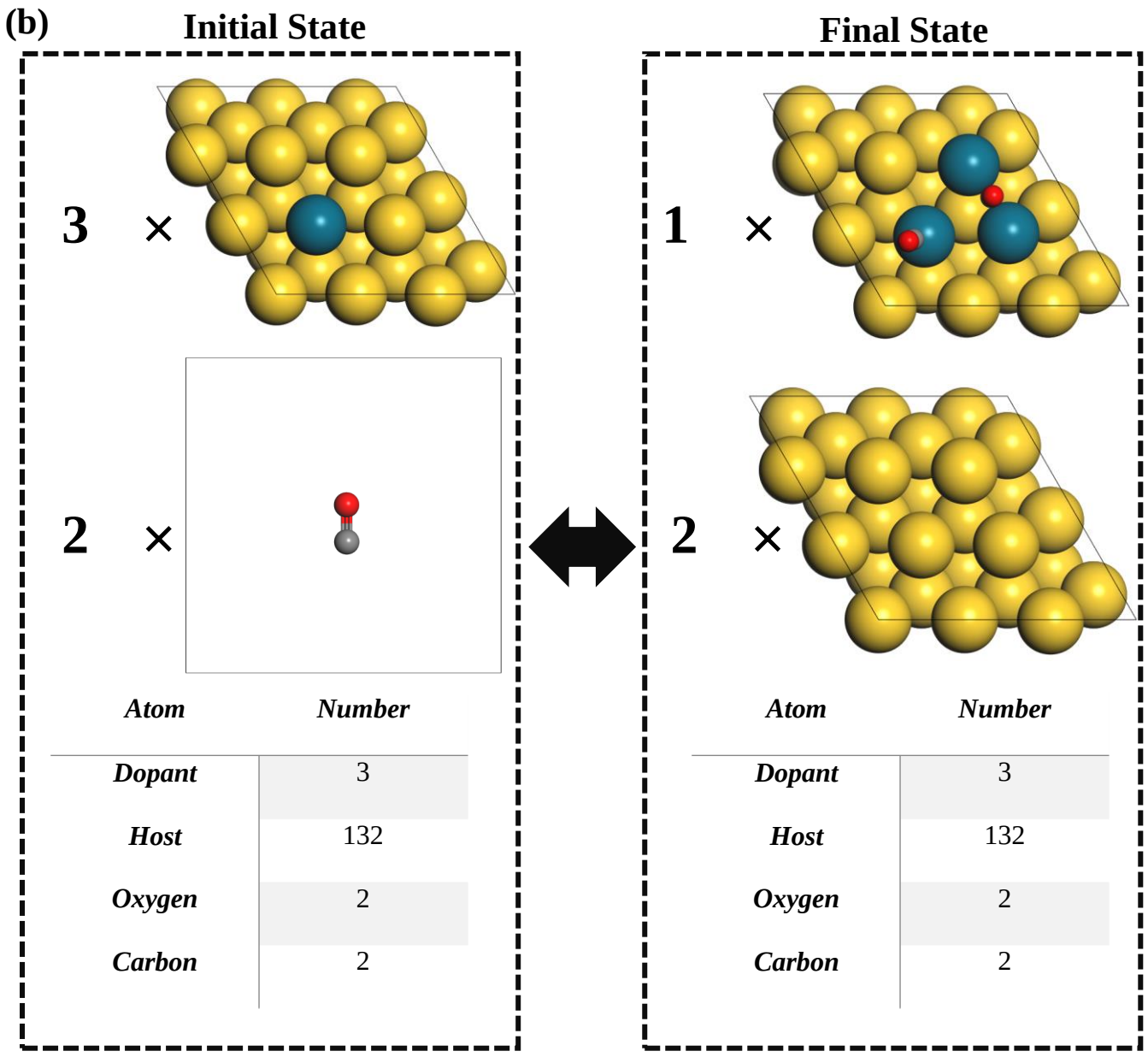

Atom	*Number*
Dopant	3
Host	132
Oxygen	2
Carbon	2

Atom	*Number*
Dopant	3
Host	132
Oxygen	2
Carbon	2

Figure S17. Panel (a) shows the top view of a DFT geometry whose formation energy needs to be calculated. Panel (b) shows the structures of the initial and final states. Once the energies of the latter structures are known, the formation energy of the structure in panel (a) can be found by using eq. (S11)**.** The tables in panel (b) provide the number of different atoms in the final and initial states and show that the number of atoms is balanced, as it should be. Dopant, host, carbon and oxygen atoms are shown in teal, yellow, grey and red colour, respectively.

XII. Monte Carlo simulation bias testing

We have performed additional testing to ensure that our MC simulations are not biased to certain configurations because of how the initial configuration was prepared. This testing included three MC simulations for the Pd/Ag(111) surface at P_N=10^{-4}, i.e. the normalised pressure that brings about the maximum amount of aggregation at 350 K (see main text). The lattice was initialised with three different configurations as follows (Figure S18): *initial lattice structure 1* - Pd atoms are organised in a large island and CO is adsorbed on the most stable adsorption sites of this island; *initial lattice structure 2* - Pd atoms are organised in a CO-free island; *initial structure 3* - Pd are randomly seeded on the MC lattice. We point out that the latter configuration was the one used as initial for the calculations presented in the main text.

For each MC simulation, we have computed the CO coverage and the average species fractions under stationary conditions and the results are summarised in Table S4. Evidently, the final result is independent of the initial lattice state, as long as the system reaches stationary conditions, under which all fractions and CO coverages are calculated. This observation indicates that our MC simulations are neither biased toward the SAA phase nor toward the island phase, and that, in any case, the most thermodynamically favourable surface configurations are sampled.

Table S4. Summary of the fractions of surface species and CO coverage for the MC simulations where different initial lattice structures were employed.

Initial Lattice Structure	**1**	**2**	**3**
$\overline{Y_{SAs}}$	0.59 ± 0.09	0.60 ± 0.07	0.60 ± 0.08
$\overline{Y_{Dimers}}$	0.19 ± 0.06	0.17 ± 0.06	0.17 ± 0.05
$\overline{Y_{Trimers}}$	0.16 ± 0.07	0.15 ± 0.07	0.15 ± 0.05
$\overline{Y_{Islands}}$	0.06 ± 0.02	0.08 ± 0.02	0.08 ± 0.03
Ω_{CO}	0.37 ± 0.04	0.35 ± 0.04	0.36 ± 0.04

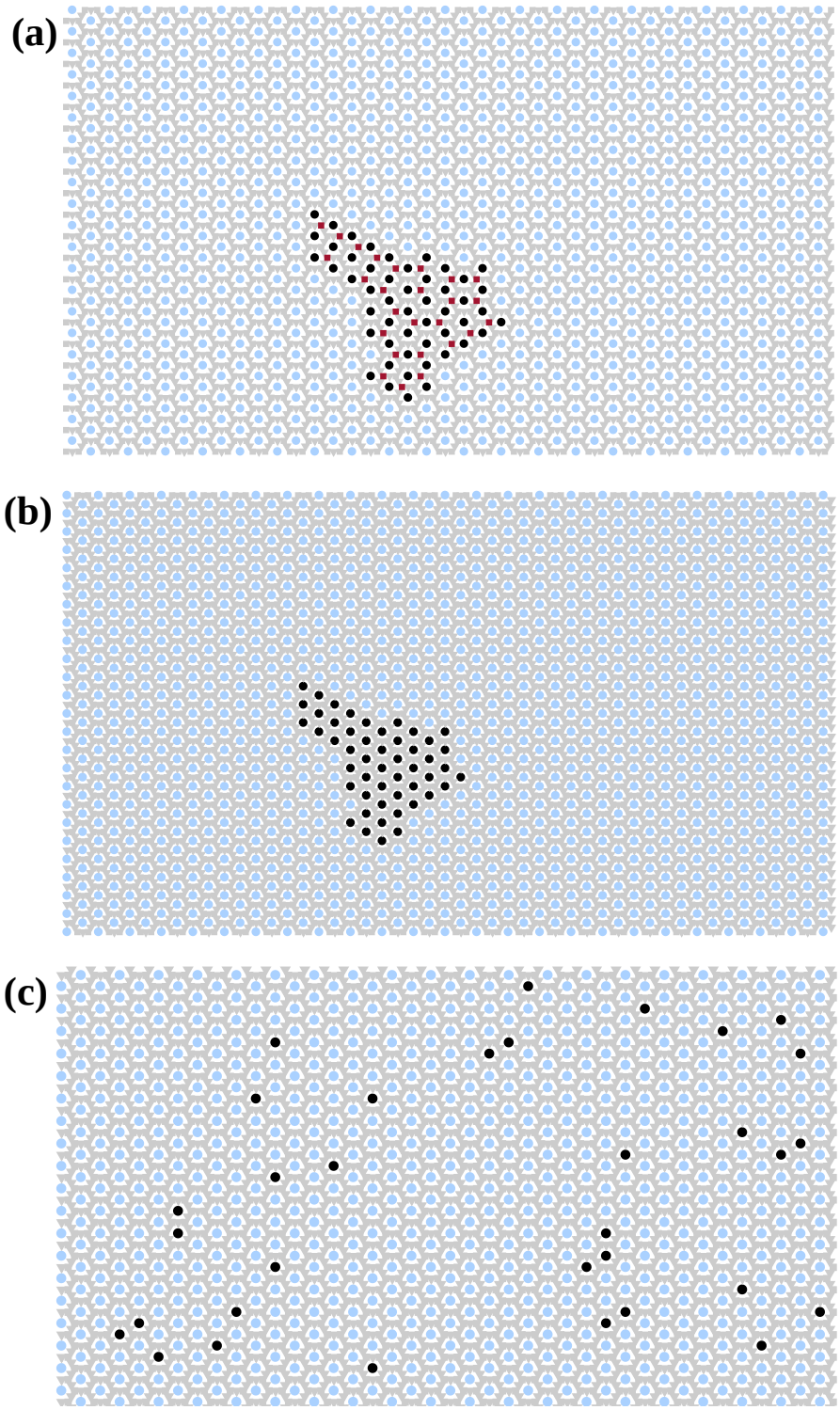

Figure S18. (a) *Initial lattice structure 1*, where Pd atoms form a large island and CO is adsorbed on threefold sites within the island; (b) *Initial lattice structure 2*, where Pd atoms form a large island in the absence of CO; (c) *Initial lattice structure 3*, where Pd atoms are randomly seeded on lattice sites. To retrieve lattice structure (a), we performed a MC simulation where atomic swaps were precluded from the reaction mechanism (see Figure 2 in the main text), and the lattice was initialised as in (b). Then we allowed the system to reach stationary conditions in the presence of CO gas, thereby retrieving lattice structure (a). Structure (c) was the initial lattice configuration for the actual simulation whose result is presented in the main text for $P_N=10^{-4}$ (see the main text). In all panels: Pd and Ag atoms are shown in black and light blue, respectively, CO adsorbates on a threefold site surrounded by dopant atoms are shown in magenta and CO-free twofold and threefold sites are shown in grey. We note that all panels show only a representative part of the MC lattice.

References

(1) Papanikolaou, K. G.; Darby, M. T.; Stamatakis, M. Adlayer Structure and Lattice Size Effects on Catalytic Rates Predicted from KMC Simulations : NO Oxidation on Pt (111). *J. Chem. Phys.* **2018**, *149*, 184701.

(2) Zhdanov, V. P.; Kasemo, B. Surface Restructuring and Aperiodic Kinetic Oscillations in Heterogeneous Catalytic Reactions. *J. Stat. Phys.* **2000**, *101*, 631–647.

(3) Darby, M. T.; Sykes, E. C. H.; Michaelides, A.; Stamatakis, M. Carbon Monoxide Poisoning Resistance and Structural Stability of Single Atom Alloys. *Top. Catal.* **2018**, *61*, 428–438.

(4) Jansen, A. P. J. *An Introduction to Kinetic Monte Carlo Simulations of Surface Reactions*; Lecture Notes in Physics; Springer Berlin Heidelberg: Berlin, Heidelberg, 2012; Vol. 856.

(5) Deringer, V. L.; Tchougréeff, A. L.; Dronskowski, R. Crystal Orbital Hamilton Population (COHP) Analysis as Projected from Plane-Wave Basis Sets. *J. Phys. Chem. A* **2011**, *115*, 5461–5466.

(6) Maintz, S.; Deringer, V. L.; Tchougréeff, A. L.; Dronskowski, R. Analytic Projection from Plane-Wave and PAW Wavefunctions and Application to Chemical-Bonding Analysis in Solids. *J. Comput. Chem.* **2013**, *34*, 2557–2567.

(7) Dronskowski, R.; Blöchl, P. E. Crystal Orbital Hamilton Populations (COHP). Energy-Resolved Visualization of Chemical Bonding in Solids Based on Density-Functional Calculations. *J. Phys. Chem.* **1993**, *97*, 8617–8624.

(8) Thirumalai, H.; Kitchin, J. R. Investigating the Reactivity of Single Atom Alloys Using Density Functional Theory. *Top. Catal.* **2018**, *61*, 462–474.

(9) Papanikolaou, K. G.; Darby, M. T.; Stamatakis, M. CO-Induced Aggregation and Segregation of Highly Dilute Alloys : A Density Functional Theory Study. *J. Phys. Chem. C* **2019**, *123*, 9128–9138.

(10) Hammer, B.; Nørskov, J. K. Electronic Factors Determining the Reactivity of Metal Surfaces. *Surf. Sci.* **1995**, *343*, 211–220.